Exploring strongly correlated Rydberg excitations in cold gases using full counting statistics

María Martínez Valado

Advisors:
Dr. Donatella Ciampini
Prof. Matthias Weidemüller

Università degli Studi di Pisa
Dipartimento di Fisica *E. Fermi*
Dottorato in Fisica Applicata
May 2015

Dissertation
submitted to the
Combined Faculties for the Natural Sciences and for Mathematics
of the Ruperto-Carola University of Heidelberg, Germany
for the degree of
Doctor of Natural Sciences

Put forward by
Lic. María Martínez Valado
Born in: Verea (Ourense, Spain)
Oral examination date: May 18th, 2015

Exploring strongly correlated Rydberg excitations in cold gases using full counting statistics

Referees

Prof. Dr. Giovanni Modugno
Prof. Dr. Thomas Gasenzer

A mi familia

A Giovanni

Abstract

This Thesis aims to investigate the role of correlations arising in cold Rydberg samples as a consequence of the strong interactions between its constituents. For this purpose, two different approaches, which allow the study of different types of correlations, are presented here. On the one hand, as a consequence of the interactions between the excitations, resonantly excited Rydberg ensembles exhibit a strong degree of anti-correlation, which becomes visible either through the blockade of the excitation, or through a slowing down of the dynamics. On the other hand, the Rydberg-Rydberg interactions in the off-resonant regime enhance the generation of new excitations, leading the system to exhibit strong correlations. Moreover, by analyzing the full counting statistics (FCS) of the excitation events we get more insight into this process. Thus, in the off-resonant case, the most notable features of these strong correlations are the bimodal shapes of histograms of the counting distributions. Furthermore, under strong dissipative conditions, the FCS analysis reveals signs of a transition between two dynamical phases. Although the afore-mentioned effects were observed in a system governed by an Ising-type Hamiltonian, correlations emerge in other systems as well. For instance, in systems described by Heisenberg XX-type Hamiltonians, the strong interactions lead the dipolar energy exchange between the excitations.

Riassunto

In questa Tesi viene investigato il ruolo delle correlazioni che emergono in un gas di atomi di Rydberg fortemente interagenti. Nel caso in cui le eccitazioni di Rydberg vengano create su risonanza, come conseguenza delle forti interazioni, si verifica sia un effetto di bloccaggio della eccitazion, che un rallentamento della dinamica. D'altro canto, per eccitazione fuori risonanza, le forti interazioni favoriscono la generazione di nuove eccitazioni Rydberg creando un sistema con un forte di grado di correlazione, come conseguenza della natura sequenziale del processo di eccitazione. Attraverso l'analisi della statistica completa dell'eccitazione è possibile ottenere una maggiore quantità di informazioni sul sistema. La conseguenza più evidente di queste forti

correlazioni è il carattere bimodale della distribuzione. Inoltre, in condizioni di regime fortemente dissipativo, l'analisi della statistica completa delle eccitazioni mostra segni di una transizione fra due fasi dinamiche. Sebbene questi effetti siano stati osservati su un sistema descrito da una Hamiltoniana tipo Ising, questi sono osservabili anche in altri sistemi fortemente correlati, come quelli descritti da una Hamiltoniana tipo Heisenberg-XX, dove le forte interazioni fra gli atomi producono gli scambi energetici dipolari tra le eccitazioni.

Zussamenfassung

In dieser Doktorarbeit wird die Rolle der Korrelationen untersucht, die aufgrund der starken Wechselwirkungen zwischen Rydbergatomen in kalten Gasen auftreten. Zu diesem Zweck werden hier zwei verschiedene Methoden vorgestellt, die eine Untersuchung dieser Korrelationen ermöglichen. Zum einen weisen resonant angeregte Ensembles von Rydbergatomen starke Anti-Korrelationen aufgrund der Wechselwirkungen zwischen den angeregten Atomen auf; diese werden entweder als Anregungsblockade sichtbar oder durch eine Verlangsamung der Dynamik. Zum anderen verstärken die Rydberg-Rydberg Wechselwirkungen im nichtresonanten Anregungsregime die Bildung neuer Anregungen, was zu starken Korrelationen im System führt. Wir erhalten einen tieferen Einblick in diesen Prozess durch eine Analyse der Full Counting Statistics (FSC) der Anregungsereignisse. Im nichtresonanten Fall sind die auffälligsten Merkmale der starken Korrelationen gegeben durch eine bimodale Form der Histogramme der Anregungsereignisse. Unter stark dissipativen Bedingungen offenbart die Analyse der FSC zudem Anzeichen eines Phasenübergangs zwischen zwei dynamischen Phasen. Die obengenannten Effekte wurden zwar in Systemen nachgewiesen, die durch einen Hamilton-Operator vom Ising-Typ beschrieben werden, doch entstehen Korrelationen auch in anderen Systemen. So führen starke Wechselwirkungen in Systemen vom Typ Heisenberg-XX zu einem dipolaren Energieaustausch zwischen den angeregten Atomen.

List of publications

This thesis is based on the following manuscripts and publications:

- **Rydberg tomography of an ultracold atomic cloud**
  M. M. Valado, N. Malossi, S. Scotto, D. Ciampini, E. Arimondo, and O. Morsch
  Physical Review A **88**, 045401 (2013)

- **Full counting statistics and phase diagram of a dissipative Rydberg gas**
  N. Malossi, M. M. Valado, S. Scotto, P. Huillery, P. Pillet, D. Ciampini, E. Arimondo, and O. Morsch
  Physical Review Letters **113**, 023006 (2014)

- **Preparing cold atomic samples for Rydberg studies**
  M. M. Valado, M. D. Hoogerland, C. Simonelli, E. Arimondo, D. Ciampini and O. Morsch
  Journal of Physics B: Conference Series, in press (2015)

- **Observation of kinetic constraints in a cold Rydberg gas**
  M. M. Valado, C. Simonelli, M. D. Hoogerland, E. Arimondo, D. Ciampini and O. Morsch
  in preparation

- **Rydberg avalanches in an off-resonantly driven ultracold gas**
  M. M. Valado, C. Simonelli, E. Arimondo, I. Lesanovsky, D. Ciampini and O. Morsch
  in preparation

The author furthermore contributed to the following publications:

- **van der Waals explosion of cold Rydberg aggregates**
  R. Faoro, C. Simonelli, M. Archimi, G. Masella, M.M. Valado, R. Manella, D. Ciampini, E. Arimondo, and O. Morsch
  in preparation

- **Strongly correlated excitation of a quasi-1D Rydberg gas**
  N. Malossi, M.M. Valado, S. Scotto, D. Ciampini, E. Arimondo, and O. Morsch
  Journal of Physics B: Conference Series **497**, 045401 (2014)

- **Coherent emission of atomic soliton pairs by Feshbach-resonance tuning**
  H. Michinel, A. Paredes, M.M. Valado, D. Feijoo
  Physical Review A: Conference Series **86**, 013620 (2012)

Contents

List of Figures

Introduction

Research on the correlations arising in natural systems and how they influence the evolution of the constituent particles constitute a very active field of science, due to the fact that understanding the meaning of a simple correlation can be the key to explaining the behavior of complex systems. The influence of strong correlations is visible in a wide range of systems. For instance, in solids the interactions between the electrons and the coupling between the charge, spin, orbital, and lattice degrees of freedom play an important role in determining the electronic and magnetic ordering of electronic ensembles [2]. Furthermore, the physics of strong correlations is behind some properties of technologically relevant materials such as high-temperature superconductors [3], magnetic systems [4, 5]; and is also relevant in quantum information [6, 7]. Particularly important for our research are the correlations emerging in atomic systems due to the interactions between its constituent particles. As a consequence of these interactions, small changes in an external parameter may have dramatic effects on the ground state of the system, changing, for instance, the electronic or the magnetic phase of the material. These phase transitions, which can be induced at zero temperature, are a quantum-mechanical effect, and exhibit a quantum critical point separating the two ground states [8].

In recent years, Rydberg atoms, i.e. atoms excited to high energy states, in ultracold gases have been extensively studied due to their peculiar properties (e.g. lifetimes of the order of hundreds of microseconds high sensitivity to electric fields and strong interactions), which make them the ideal candidates for a large variety of applications, ranging from the implementation of fast quantum gates for quantum computation to the realization of quantum simulators of strongly interacting many-body systems, [9, 10, 11, 12, 13, 14]. In fact, the strong interactions these systems exhibit, which can be dipole-dipole or van der Waals interactions, make them ideal candidates for studying many-body effects involving long-range correlations [15, 16, 17, 18, 19, 20, 21, 22, 1]. The aim of the present Thesis is to study the correlations emerging in cold atoms gases excited to such strongly interacting Rydberg states and the characterization of the rich phenomena that arise in

these systems as a consequence of the strong intractions. In our experiments, we use two different approaches to characterize the interaction-related phenomena in Rydberg systems. On the one hand, the resonant laser driving in the non-dissipative regime, under which the majority of the experiments involving Rydberg atoms have been performed [10, 1, 23]. The interest in this regime relies on the fact that one of the most striking features of Rydberg systems emerges under these conditions: the so-called blockade effect [24, 25, 26]. This phenomenon, whereby only a single excitation is allowed within the blockade sphere, has recently attracted the attention of the scientific community due to its potential application in quantum information processing [23, 27, 28]. In the experiments done under resonant conditions, the strong interactions between Rydberg atoms manifest themselves either as spatial correlations [22, 21], or through a reduction of fluctuations [29]. Despite the importance it has received in the past years, the blockade effect is not the only characteristic phenomenon arising in resonantly excited Rydberg samples. Recent theoretical investigations have shown that the incoherent dynamics of such a system is described by a master equation with manifest kinetic constraints [30]. These constraints lead to a spatially correlated collective relaxation of the system, which in experimental terms becomes visible through the dynamical heterogeneity (some regions of the sample experience faster dynamics than others) that slows down the global dynamics.

The second way to approach the study of correlations arising from Rydberg systems arises in the context of an off-resonant excitation of Rydberg states, for which the behavior of the system depends strongly on the detuning and the sign (attractive or repulsive) of the interaction. As a further important ingredient, dissipation has been shown to lead to novel phases and exotic phenomena. In our experiments, such correlations are characterized through the analysis of the full counting statistics of the excitation events, similarly to the methods recently used in condensed matter physics to evidence correlations in electronic transport processes [31, 32]. Both excitation regimes (on and off-resonant) are reached using the same experimental setup, allowing us to study correlations or anti-correlations in a controlled many-body system depending on the selected parameters.

This concept is summarized in Fig. 1. In Fig. 1(a) I show a cloud full of blockade spheres. Intuitively, one can expect that for long durations of the excitation time, a higher number of excitations should be generated. In Fig. 1(b) I show the expected Rydberg fraction (continuous red line) versus the measured one (red circles) as a function of the excitation time. The strong suppression of the excitation is a consequence of the blockade effect. The difference between the curves evidences the strong degree of anti-correlations present this system. This issue will be discussed in detail in Ch. 3. In

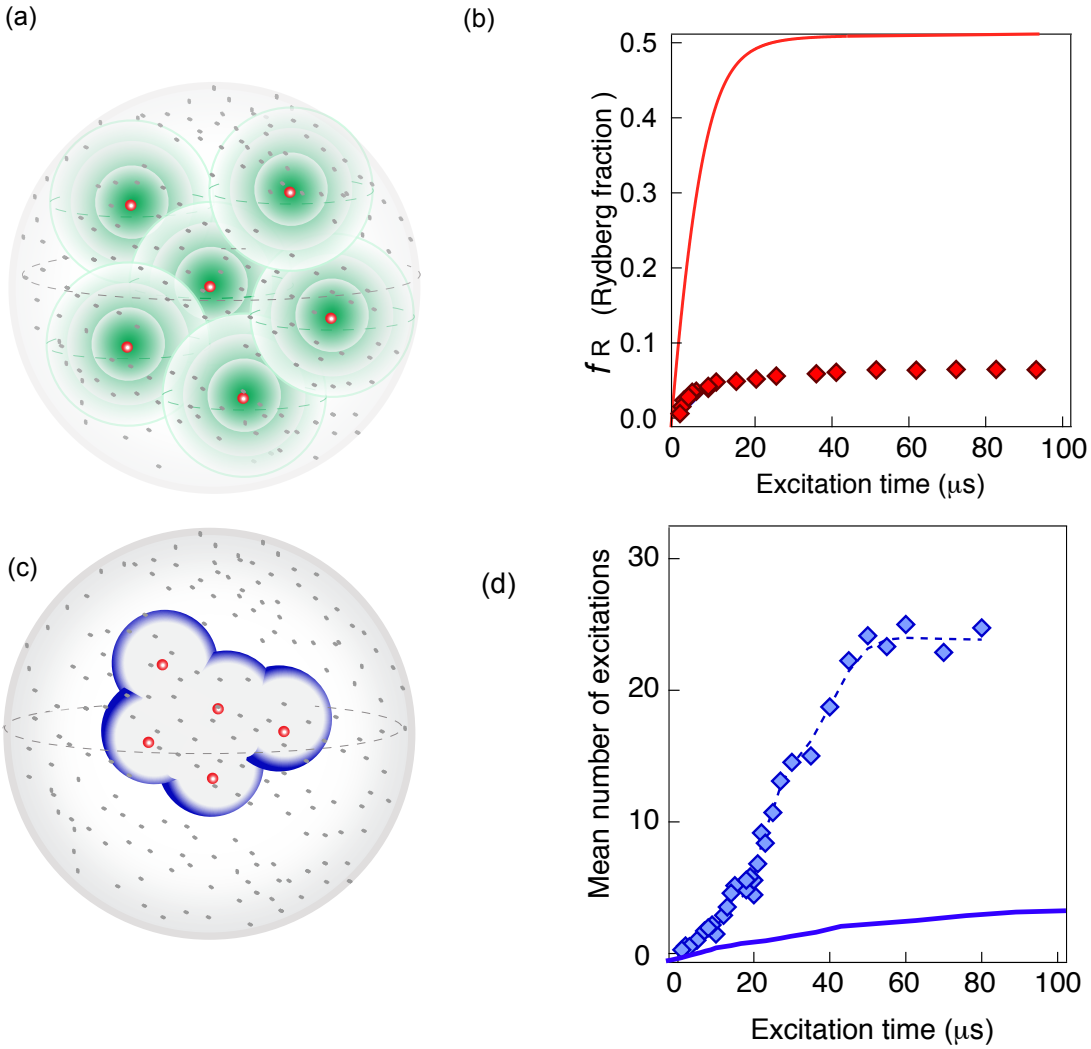

Figure 1: (a) Resonantly excited Rydberg sample. As a consequence of the dipole blockade effect, the spheres in which only a Rydberg excitation is allowed are generated. In the fully blockade regime the cloud is full by the maximum number of spheres that fit into it. (b) Qualitative theoretical time dependence in absence of interactions (continuous red line) and the actually measured Rydberg fraction (red diamonds). The latter one exhibits a strong suppression as a consequence of the blockade effect. This evidences the strong degree of anti-correlation present in this system. This will be explained in detail in Ch. 3. (c) Off-resonant Rydberg excitations in a cold cloud. (d) Due to the strong dependence of the generation of the excitations event on the detuning and the character of the interaction between Rydberg atoms, not many excitations are expected to occur (continuous blue line). However under the right conditions, i.e. the interactions between the atoms and the detuning present the same value and sign; the interactions compensate the energy shift (more details Ch. 4); leading to new Rydberg excitations to be generated as the system evolves (blue diamonds). The fact that the measured excitations reach higher values than the expected ones evidences the strong degree of correlations in this system.

Fig. 1(c) the same sample is reported but, this time, atoms are excited off-resonantly. The plot in Fig. 1(d), is a study of the dynamics of this system. The continuous blue line indicates the expected dynamics of the system in the absence of interaction-induced correlations and symbols represent the actually measured dynamics (blue diamonds). In this case, the differences between the two curves indicates a strong degree of correlations present in this system. This argument will be explained in detail in Ch. 4.

This thesis is organized as follows:

Ch.1 reviews the concepts of Rydberg atoms and their associated strong interactions, as well as the basic aspects of the Dicke Model and the Cooperative Dicke Model, developed by the group of P. Pillet (Laboratoire Aimé Cotton, Orsay, France), which is used in the frame of this Thesis as theoretical support for some of the experimental results. Ch.2 describes in detail the experimental setup present in the BEC lab in Pisa, used to perform all the experiments I will present on the following pages. Here I describe as well some innovations regarding to the setup that have been done during my PhD, like the techniques to prepare atomic samples varying the density of the cloud (Ch.2.1), published in [33], and the seed technique used to generate off-resonant excitations (Ch.2.2.3). In Ch.2.3 I introduce the full counting statistics analysis, which has proved to be a powerful tool for unveiling many-body effects in Rydberg gases. From Ch.3 to 6, I present the central results obtained during my PhD. More specifically, in Ch.3 I present the results of an experimental study on the dynamics of Rydberg samples excited on resonance in the incoherent and non-dissipative regime. Under these conditions, the strong interactions of Rydberg systems lead to the emergence of anti-correlations, through the well-known blockade effect. These results have already been published in [34]. Additionally, I study also the incoherent dynamics of a resonantly excited Rydberg gas, where signatures of kinetic constraints, like dynamical heterogeneity, are expected (predicted theoretically in [30]). Ch.4 and Ch.5 report on the experimental results obtained when Rydberg atoms are excited off resonance, leading, in this case, to strong correlations. Hence, in Ch. 4, I describe how off-resonant Rydberg excitations - or aggregates - are generated under non-dissipative conditions. The cooperative Dicke model will be used here in order to offer a more consistent interpretation of the experimental observations. Contrary to the resonant case, here the interactions between Rydberg excitations enhance the generation of new ones, favouring the growing of the aggregates. This process exhibits three different stages: *ignition*, when the first excitation is generated; *facilitation*, when the aggregates grow; and *avalanche*, in which multiple excitations are generated and exotic phenomena arises, specially under highly dissipative conditions. Each one of these stages is characterized by a certain degree of

correlation. In Ch.4.2.2 I present some experimental results in which the facilitation stage is studied by using a simple technique (whose implementation in the setup is described in Ch.2.2.3) that allows us to "isolate" the facilitation stage from the other ones. In Ch.5 I explore the avalanche stage and the rich phenomena emerging in the presence of strong dissipation. I discuss the experimental signatures we found, supported also by theoretical works, of the existence of two dynamical phases with a transition region in between and its interpretation. These results and their interpretation provided as well the basis for a paper published last year [35]. In the last chapter, Ch.6, I report on a theoretical investigation that I performed in the "Physikalisches Institut" of the University of Heidelberg (Germany), in the framework of the Thesis cotutelle. During the time I spent there, I was involved in the study of short-range interactions in Rydberg systems. My task consisted of generating the computer code and simulating dipole mediated exchange of population between S and P Rydberg states. Particularly, I focused on the different interaction regimes that arise in these samples depending on which timescale dominates: that of the dipole-dipole interactions or the Rabi frequency. This work served also to characterize a new component of the setup, a microwave pulse generator that allows to generate Rydberg P-excitations, which is the first step for future investigations in energy transport experiments.

Chapter 1

Rydberg atoms

Atoms excited to high energy states, so-called Rydberg atoms [9], have been studied since the beginning of the twentieth century, mainly due to the role they play in quantitative atomic spectroscopy [36] . In the $1970's$ it became apparent that Rydberg atoms could play an important role in naturally occurring physical systems, specially in astrophysics [37, 38] and plasma physics [39]. Besides, the developement of the tunable dye laser [40, 41] made it possible, in combination with a simple apparatus, to excite large numbers of atoms to a well-defined Rydberg state. However, it was necessary to wait until the $1990's$, when the field of cold atomic gases faced a revolution with achievements such as the Bose-Einstein condensation [42, 43, 44]; when Rydberg atoms came back to the scientific community spotlight, due to their *extreme* properties and their possible applications. Since then, the field of ultracold Rydberg physics evolved towards different research areas, ranging from quantum computation and quantum simulation [45, 23, 46, 47, 48, 49] quantum non-linear optics [50, 51], energy transport [52], ultracold chemistry [53] or the study of phase transitions [16, 54, 55, 56, 57] and exotic quantum phases [58, 59]. The common denominator of those works relies on the fact that such diverse phenomena can be approached experimentally making use of the properties of Rydberg atoms: their size (which can be as large as several microns), the strong interactions between them, the large lifetimes or the sensitivity to electric fields. In this chapter we review some of the basic properties of Rydberg atoms. Then, we will focus on the nature of the Rydberg-Rydberg interactions and how the interplay with the laser field induces correlations in the system. Moreover, we will introduce some theoretical tools like the Cooperative Dicke Model, which will be used in the interpretation of the results during the following chapters.

1.1 Rydberg atoms

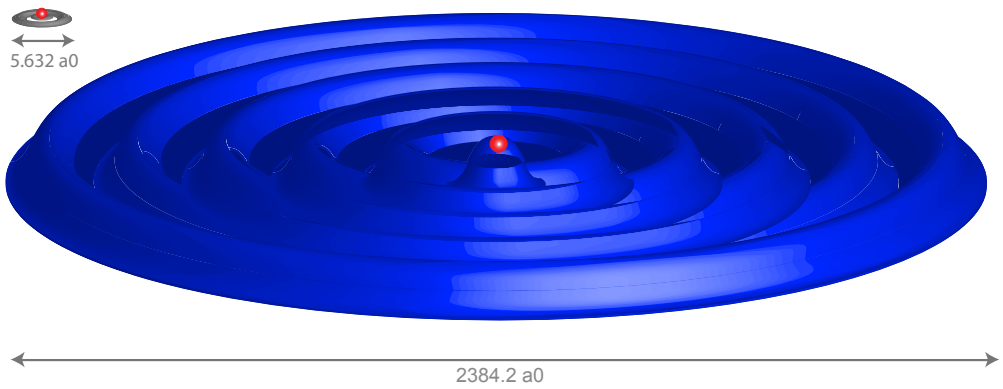

Figure 1.1: Comparison of the sizes (not to scale) in atomic units [1] of a Rydberg atom and a ground state atom in order to highlight the giant size of the former one. The size of Rydberg atoms is proportional to n^2.

Rydberg atoms are characterized by an electron in a high energy state, i.e., with a large principal quantum number, n. This concept is schematically illustrated in Fig.1.1, where a ground state atom is compared with a Rydberg atom. The first time that Rydberg atoms appear historically is in 1885, in the Balmer series for wavelength of visible series of atomic Hydrogen for transitions from $n_I = 2$ to higher lying levels [9]:

$$\lambda = \frac{4c}{Ry}\frac{n^2}{n_i^2 - 4} \tag{1.1}$$

In 1888, J. R. Rydberg generalized that expression for each pair of states n_1 and n_2, extending to the non-visible region the description of the spectra [**?**]

$$\frac{1}{\lambda} = R_\infty \left(\frac{1}{n_1^2} - \frac{1}{n_2^2}\right) \tag{1.2}$$

where $R_\infty = 109736.62\,\mathrm{cm}^{-1}$ is the Rydberg constant.

A few years later, the Bohr atomic model [60] introduces quantized values of the energy of the electron according to the principal quantum number, n, by linking the binding energy of the electron with the hydrogen spectra:

$$E_n = hc\frac{R_\infty}{n^2} \tag{1.3}$$

In analogy to this, the characteristic scaling of other properties of the hydrogen atom with the principal quantum number can be directly derived from the Bohr model. Due to the similarities of Rydberg states to those of hydrogen, these scaling laws appear also in the properties of Rydberg atoms.

In the experiments presented in this Thesis, we deal with highly excited states of rubidium, which has one valence electron. The orbit of the valence electron is large ($\sim n^2$), thus it is possible to separate it from the rest of the electrons and the nucleus, that together form the core. In this sense, a Rydberg atom is quite similar to a hydrogen atom, with the only difference coming from the size of the core. The core electrons are tightly bound and almost unperturbed by the valence electron. The main effect of the core is to screen the nuclear charge in a way that the effective potential seen by the Rydberg electron is approximately the same as that of the Hydrogen atom. The Quantum defect Theory (QDT) allows to quantify the deviations of the real core potential from that of a single positive charge, which result in a phase shift of the wave functions.This means, that the energy eigenvalues should be corrected by a certain factor as compared to those of the hydrogen atom.This is done by replacing the principal quantum number n with an effective principal quantum number. The so-called quantum defect factor, $\delta_{n,l,j}$, depends both on the principal quantum number, n, as well as on the angular momentum l. In practice, it translates the principal quantum number into an effective quantum number: $(n^*) = n - \delta_{n,l,j}$. With this modification the energy levels of the rubidium Rydberg-states can be written like the hydrogen levels as:

$$E_{n,l,j} = -hc\frac{R_\infty}{(n^*)^2} \tag{1.4}$$

The quantum defect is determined by spectroscopic measurements [61] and can be approximated using the empirical Rydberg-Ritz formula [9]:

$$\delta_{n,l,j} = \delta_0 + \frac{\delta_2}{(n-\delta_0)^2} + \frac{\delta_4}{(n-\delta_0)^4} + \dots \tag{1.5}$$

The values of δ_0,δ_2, ... have to be determined experimentally for each atomic species. In Table 1.1 we show the values of these parameters for the

case of rubidium [9]. The quantum defects depends slightly on the value of the principal quantum number, and, specially for high n states, the first two terms of Eq. 1.5 are often sufficient.

Series	δ_0	δ_2
$ns_{1/2}$	3.13109(2)	0.204(8)
$np_{1/2}$	2.65456(15)	0.388(60)
$np_{3/2}$	2.64145(20)	0.33(18)
$nd_{3/2,5/2}$	1.347157(80)	−0.59553
$nf_{5/2,7/2}$	0.016312	−0.064007

Table 1.1: Rubidium quantum defects, from [9].

1.2 Properties

The high principal quantum number, n, gives Rydberg atoms remarkable properties, that scale with the value of the principal quantum number. Table1.2 shows some of these properties as well as the scaling law with (n^*):

Property	(n^*)**-scaling**
Binding Energy E_n	$(n^*)^{-2}$
Orbital radius	$(n^*)^2$
Level spacing	$(n^*)^{-3}$
Lifetime τ	$(n^*)^3$
Polarizability α	$(n^*)^7$
Ionisation field $\mathcal{E}_{ion}$	$(n^*)^{-4}$
Dipole-dipole interaction coefficient C_3	$(n^*)^4$
van der Waals interaction coefficient C_6	$(n^*)^{11}$

Table 1.2: Some properties of Rydberg atoms and scaling laws with the effective principal quantum number $(n^*) = n - \delta_{n,l,j}$ (see [9]).

Of particular importance for the work presented in this thesis are the long lifetime of Rydberg atoms and their high sensitivity to electric fields.

1.2.1 Lifetime of Rydberg atoms

The lifetime of alkali Rydberg atoms, determined by the radiative decay to lower lying levels but also by transitions to higher (and lower) lying states induced by blackbody radiation, can be on the order of hundreds of microseconds for $n \geq 50$ (much larger than, for instance, the lifetime of the $5P_{3/2}$,

$\tau_{lifetime} \approx 26.2\,\text{ns}$). The spontaneous decay rate between of the state $|nl\rangle$ to the lower lying state $|n'l'\rangle$ can be expressed in terms of the A Einstein coefficient :

$$A_{n'l',nl} = \frac{2e^2\omega^3_{nl,n'l'}}{3\epsilon_0\hbar c^3 h}|\langle n'l'|r|nl\rangle|^2 \tag{1.6}$$

The stimulated emission as well as absorption of blackbody radiation are given by the Einstein B coefficient :

$$B = AN(\omega) \tag{1.7}$$

where, $N(\omega)$ is the number of photons per mode of the black body radiation at temperature T and frequency ω, given by the Bose distribution:

$$N(\omega) = \frac{1}{e^{\hbar\omega/k_BT} - 1} \tag{1.8}$$

Hence, the total lifetime of the state $|nl\rangle$ can be calculated by summing these contributions over all the possible all states $|n'l'\rangle$ [1]:

$$\tau^{-1}_{nl} = \sum_{n'l'} A + \sum_{n'l'} AN(\omega_{nl,n'l'}) \tag{1.9}$$

The first sum is limited to states with energies below the Rydberg state, whereas the second sum runs over all allowed dipole transitions (transitions to ionized states are neglected).

The experiments described in this manuscript were performed using Rydberg states with n ranging from $n = 70$ to $n = 90$, and their lifetimes ($\sim (n^*)^3$) are between $150 - 200\,\mu$s [62]. In order to measure the lifetimes of Rydberg states accurately, state-sensitive detection schemes as in [63, 64], are required.

1.2.2 Rydberg atoms in electric fields

Rydberg atoms are extremely sensitive to electric fields, due to their size and the loose binding to the electron core. This feature allows a simple and fast manipulation of the excited-state energies by applying small electric fields. When moderate electric fields (which for the Rydberg states used in this thesis means electric fields on the order of $\sim 20\,\mathrm{Vcm}^{-1}$) are applied instead, the loose binding of the electron allows to separate it from the core and to ionize the Rydberg atom, which is employed as mechanism of detection of Rydberg atoms.

The effect of electric fields on Rydberg atoms can be seen by estimating the perturbation of an atomic system due to an external static electric field along the $z-$axis: $V = ezF$. According to the second order perturbation theory, the energy eigenvalues can be calculated approximately as:

$$E_n = E_n^0 + \langle n^{(0)}|V|n^{(0)}\rangle + \sum_{k\neq n} \frac{|\langle n^(0)|V|k\rangle|^2}{E_n^0 - E_k^0} \tag{1.10}$$

For low values of the angular momentum the energy levels are not degenerated, and the quadratic Stark shift dominates :

$$\Delta E = \sum_{k\neq n} \frac{|\langle n^(0)|V|k\rangle|^2}{E_n^0 - E_k^0} = \frac{1}{2}\alpha F^2 \tag{1.11}$$

where α is the polarizability. As the dipole moment scales with $(n^*)^2$ and the difference between states with $(n^*)^{-3}$(see Table 1.2), it is immediate that $\alpha \sim (n^*)^7$, given as well in Table 1.2.

To give some numbers, in the case of rubidium, the polarizability of the the $5S$ state (ground state) is $\alpha = -79.4\,\mathrm{MHz}(\mathrm{V}\cdot\mathrm{cm}^{-1})^{-2}$ [65], whereas the polarizability for the $43S$ state is $\alpha = -17.7\,\mathrm{MHz}(\mathrm{V}\cdot\mathrm{cm}^{-1})^{-2}$, which is enough to shift this state, at a field of $1\,\mathrm{Vcm}^{-1}$, 350 linewidths to the red [1], where the linewidth of Rb transition $5S - 6P$ is $\sim 60\,\mathrm{MHz}$. If states with higher angular momentum are considered, then the states with opposite parity are degenerate, forming new eigenstates with respect to the electric dipole interaction.These states exhibit a linear Stark shift dependence in small electric fields.

1.3 Interaction between Rydberg atoms

The extreme sensitivity of Rydberg atoms to external perturbations causes these atoms to “feel” the presence of other Rydberg atoms even at large

distances (on the order or several micrometers). The features associated to those interactions (strength, sign, radial and angular dependences) determine the behavior of a Rydberg system, making Rydberg gases a very rich playground for experiments and theoretical studies. Moreover, they allow to experimentally control these parameters in an easy way.

1.3.1 Dipole-dipole and van der Waals interactions

In experiments with Rydberg atoms, electric fields can be used to ionize the sample as a part of the detection process (see Ch. 2), or to induce a permanent dipole moment, because when the electron cloud is shifted with respect to the nucleus, atoms gain a dipole moment. As a result, dipole-dipole interactions between two atoms or molecules with permanent dipole moments emerge.

An electrostatic dipole, with dipole moment μ, situated at the center of the cloud generates an electric field at the position $\vec{R} = R\vec{n}$ can be calculated as:

$$\vec{E}(\vec{r}) = \frac{1}{4\pi\epsilon_0}\frac{3(\vec{n}\cdot\vec{\mu})\vec{n} - \vec{\mu}}{R^3} \tag{1.12}$$

From Eq. 1.3.1, the dipole-dipole interaction between two atoms separated by a distance R along the direction $\vec{n}$ (see Fig. 1.2) is:

$$V_{dd} = \frac{1}{4\pi\epsilon_0}\frac{\vec{\mu}_1\cdot\vec{\mu}_2 - 3(\vec{\mu}_1\cdot\vec{n})(\vec{\mu}_2\cdot\vec{n})}{R^3} \tag{1.13}$$

If a relatively small electric field, $\vec{F}$ is applied, we can consider that a given state $|r\rangle$ is only coupled with the state $|r'\rangle$, closest in energy and connected by an allowed transition. The Hamiltonian matrix in this case reads:

$$\begin{pmatrix} E_r & \frac{\vec{\mu}_1\vec{\mu}_2}{R^3} \\ \frac{\vec{\mu}_1\vec{\mu}_2}{R^3} & E_r + \Delta_F \end{pmatrix}$$

where E_r correspond to the energies of the state $|r\rangle$ and Δ_F is the Förster defect, which quantifies the energy difference between the two pair of states. By diagonalizing this matrix we obtain the eigenvalues:

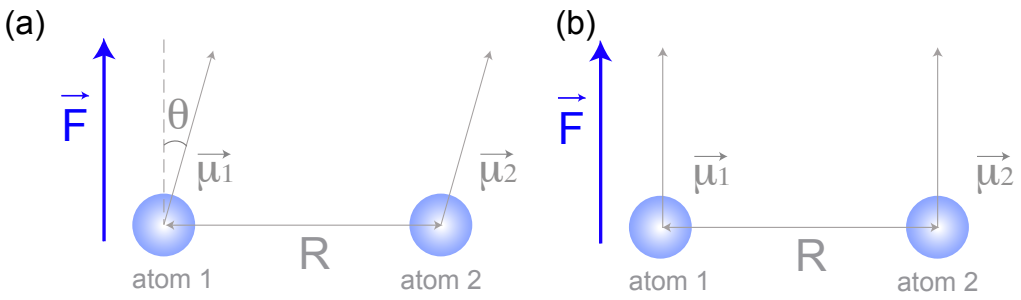

Figure 1.2: (a) Two excited atoms separated by a distance R in the presence of an electric field $\vec{F}$ with an angle between the vector of the electric field and the dipole moment of an atom θ, and (b) with the dipole moments μ_1 and μ_2 along the direction of the electric field $\vec{F}$

$$E_{\pm} = \frac{\Delta_F}{2} \pm \sqrt{\left(\frac{\Delta_F}{2}\right)^2 + \left(\frac{\mu_1\mu_2}{R^3}\right)^2} \tag{1.14}$$

Depending on the energy of the pair states, the Förster defect can be positive or negative, which determines the sign of the interaction and also its character. These features can be tuned by using a small electric field, $\frac{1}{2}\alpha\vec{F} = \vec{\mu}$, where α is the polarizability. Depending on the value of Δ_F we have different types of interactions:

- **Resonant dipole dipole interactions** $\left(\frac{\mu_1\mu_2}{R^3} >> \Delta_F\right)$. For small distances or when $\Delta_F = 0$ (Förster resonance), the dipole-dipole term dominates, leading Rydberg atoms to exhibit dipolar interactions. The energy shift of the pair states is:

$$\Delta E = \pm\frac{\hbar C_3}{R^3} \tag{1.15}$$

  Here, the C_3 coefficient determines the interaction amplitude. C_3 increases with the principal quantum number scaling with $(n^*)^4$, ($\mu_{1,2} \sim (n^*)^2$) [24].

- **van der Waals interaction** $\left(\frac{\mu_1\mu_2}{R^3} << \Delta_F\right)$. For large distances between the atoms, the dipole-dipole coupling is only perturbative. Thus, the energy shift is given by:

$$\Delta E = \pm \frac{\hbar C_6}{R^6} \tag{1.16}$$

with, $C_6 = \frac{(\mu_1 \mu_2)^2}{\Delta_F}$. Considering the scalings with the principal quantum number of $\mu_{1,2} \sim (n^*)^2$ and $\Delta_F \sim (n^*)^{-3}$, we find $C_6 \sim (n^*)^{11}$ [24]

1.3.2 Dipole blockade and collective excitation

A distinctive feature which comes directly from the strong interactions between Rydberg atoms is the dipole blockade [11, 12, 25, 26, 24] whereby the excitation of a particular atom can be suppressed by a neighboring one that is already in a Rydberg state. It can be understood from a pair state picture, see Fig. 1.3, where a laser field resonant with the excitation frequency of a single Rydberg atom cannot excite a second Rydberg atom in the vicinity of the first due to the energy shift of the doubly excited state, caused by the interactions between atoms in the Rydberg state.

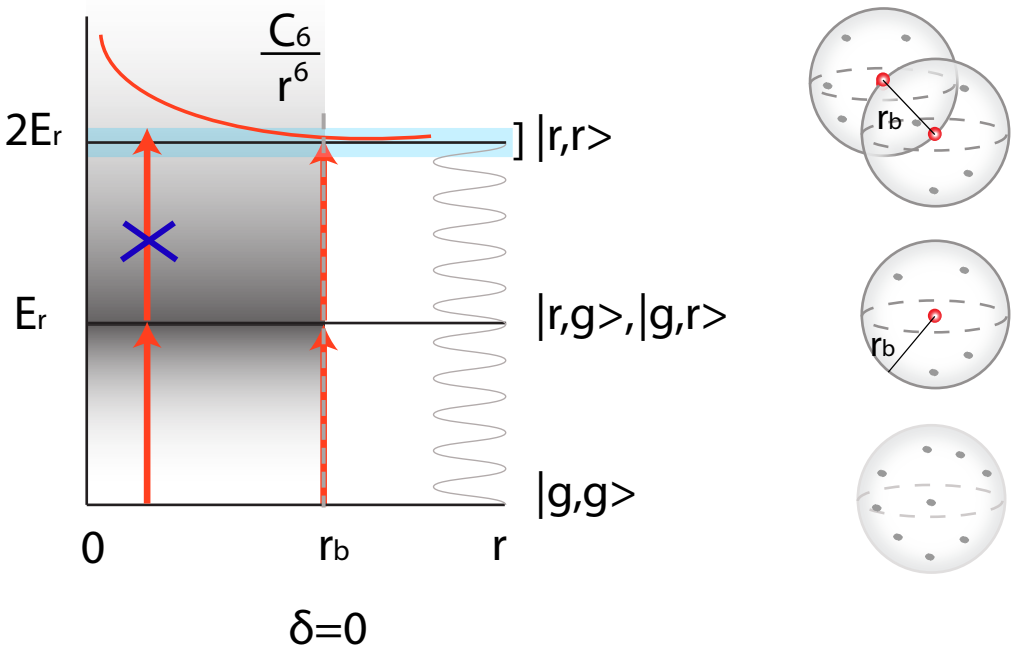

Figure 1.3: Schematic representation of the dipole blockade effect. Once a Rydberg excitation is generated, the interactions between Rydberg atoms induce a shift of the energy levels of the surrounding ground state atoms, blocking the excitation process within a volume defined by the radius, r_b.

The radius of influence of an atom in this sense is called the blockade radius,

$$r_b \equiv \sqrt[6]{\frac{C_6}{\hbar\Omega}} \tag{1.17}$$

where Ω is the Rabi frequency, i.e. the excitation linewidth (for a sufficiently narrow linewidth of the laser). Consequently, the value of the blockade radius depends on the interaction strength and the linewidth of the Rydberg excitation. If the interaction energy becomes larger than the Rabi frequency and the laser linewidth, the excitation laser frequency is out of resonance with the shifted state and hence, only one atom at a time can be excited to the Rydberg state within a blockade radius. At the beginning of the excitations the blockade spheres are generated independently, Fig.1.4 (a). As the system evolves in time, more and more blockade spheres are created, and, as a direct consequence of the dipole blockade, the excitation dynamics of the atoms are strongly correlated. This leads to a cutoff in the excitation when all the available blockade volumes in the sample have been exhausted, see Fig.1.4 (b).

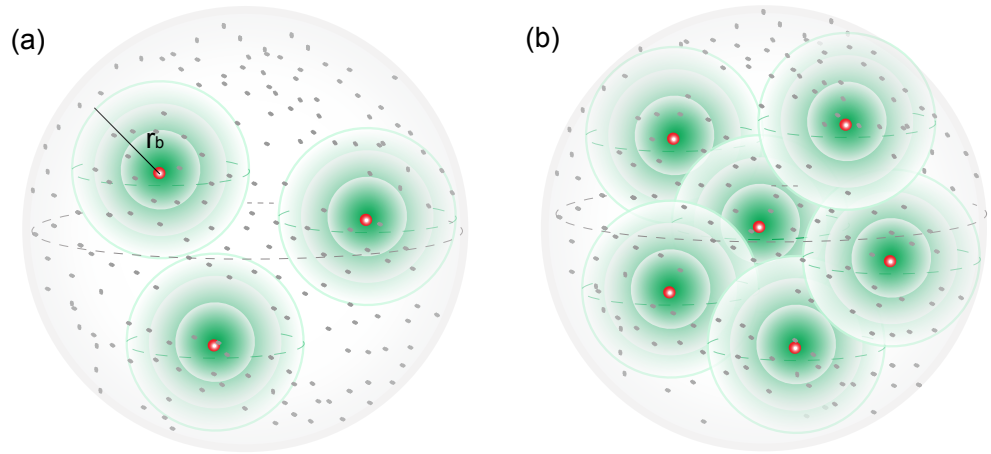

Figure 1.4: Illustration of the Rydberg blockade spheres in the cloud. When the laser field irradiates the cloud some atoms are excited to Rydberg states. Around each excitation, a blockade sphere (an area within which only a single Rydberg excitation is possible) is generated. At the beginning of the excitations few blockade spheres are generated (a). As the system evolves with time, more and more blockade spheres are generated until the system arrives to the fully blockade regime (saturated regime) in which the maximum number of spheres that can fit into the cloud volume has been reached (b)

Depending on the strength of the interactions between Rydberg excitations, three different types of resonant excitation regimes can be distinguished:

- **Single atom excitation**, which occcurs if a single atom is driven to the Rydberg state by a Rabi frequency Ω_0;
- N **non-interacting atoms excitation**, which undergo the same Rabi oscillation. In this case the amplitude of the population in the Rydberg state is equal to N.
- **Collective excitation**, where N interacting atoms of the sample are illuminated together with the same laser field. The atoms being indistinguishable relatively to the laser excitation and Rydberg excitations are shared collectively by all the atoms.

The ground state of the system is:

$$|\psi^{(N,0)}\rangle = |g_1, g_2, ..., g_N\rangle \tag{1.18}$$

When the j^{th} atom is excited to the Rydberg state we get : $|g_1, g_2, ...r_j, ...g_N\rangle$. Due to symmetry with respect to permutation, the collective state with one excitation is written as:

$$|\psi^{(N,1)}\rangle = \frac{1}{\sqrt{N}} \sum_{j=1}^{N} |g_1, g_2, ..., r_j, ...g_N\rangle \cdot e^{-i\vec{R}_j\vec{k}} \tag{1.19}$$

where N is the number of atoms of the sample. The phase factor $e^{-i\vec{R}_j\vec{k}}$ accounts for the relative phase of the laser field with wave vector $\vec{k}$ at the position$\vec{R}_j$ of the Rydberg atom. As this phase factor is not relevant when considering the blockade phenomenon itself, in the following we disregard it.

Thus, in the case of a fully blockaded ensemble, the $|\psi^{(N,1)}\rangle$ is the only possible state, all the states with two Rydberg excitations are shifted out of resonance of the laser field due to Rydberg-Rydberg interactions.

The full basis of the system will be formed by $|\psi^{(N,1)}\rangle$ and $|\psi^{(N,0)}\rangle$. The Rabi frequency associated to the excitation of the state $|\psi^{(N,1)}\rangle$ from the ground state $|\psi^{(N,0)}\rangle$ differs from the single atom case by a factor $\sqrt{N}$:

$$\Omega_{coll} = \sqrt{N}\Omega_0 \tag{1.20}$$

Figure 1.5: Sketch representing the collective excitation.

The appearance of the factor $\sqrt{N}$ factor is a typical characteristic for collective excitation. The N ground state atoms inside the blockade sphere share equally one excitation. In this sense a fully blockaded ensemble can be treated as a two-level system, characterized by an enhanced coupling with the laser field. In Rydberg literature, it is often called a superatom [13, 14, 66].

1.4 The Cooperative Dicke model

In the frame of this Thesis we use an extension of the Dicke model [67] applied to Rydberg excitations, in a work done in collaboration with the group of P. Pillet (Laboratoire Aimé Cotton, Orsay, France), which is explained in Ch.4. The Dicke states represent a useful theoretical tool to study the coupling of an ensemble of identical atoms with the electromagnetic field. It has been mainly used in the frame of the Superradiance phenomenon, reviewed in [68, 69].

Here, the original Dicke model, based on the laser excitation conserving the cooperative character of the collective atomic wave functions, was modified by including the van-der-Waals interactions between the collective Dicke states, taking into account the r^{-3} contribution at short distances for S states. A detailed description of the so-called Cooperative Dicke model can be found in [70].

1.4.1 The Dicke states

We consider an ensemble of N two-level atoms. These levels are labeled $|g\rangle$, for the ground state, and $|r\rangle$, for the Rydberg state. The position of the atom i is $\vec{R}_i$. Additionally, a laser field defined by its wave vector $\vec{k}$ is considered. From the transition and projector operators of each atom, $\hat{\sigma}^i_{\alpha,\beta} = |\alpha_i\rangle\langle\beta|(\alpha, \beta = g, r)$, the collective operators can be defined as:

$$\begin{aligned}\hat{R}^{+}_{\vec{k}} &= \sum_{i=1}^{N} \hat{\sigma}^{i}_{rg} e^{i\vec{k}.\vec{R}_i} \\ \hat{R}^{-}_{\vec{k}} &= \sum_{i=1}^{N} \hat{\sigma}^{i}_{gr} e^{i\vec{k}.\vec{R}_i} \\ \hat{R}^{(3)}_{\vec{k}} &= \tfrac{1}{2} \sum_{i=1}^{N} \hat{\sigma}^{i}_{rr} - \hat{\sigma^{i}_{gg}}\end{aligned} \tag{1.21}$$

whose commutation relations are:

$$\begin{aligned}\left[\hat{R}^{+}_{\vec{k}}, \hat{R}^{-}_{\vec{k}}\right] &= 2\hat{R}^{(3)}_{\vec{k}} \\ \left[\hat{R}^{+}_{\vec{k}}, \hat{R}^{(3)}_{\vec{k}}\right] &= 2\hat{R}^{+}_{\vec{k}}\end{aligned} \tag{1.22}$$

From these equations, the collective operator $\hat{R}^{2}_{\vec{k}}$ is defined as:

$$\hat{R}^{2}_{\vec{k}} = \hat{R}^{(3)2}_{\vec{k}} + \frac{1}{2}\left(\hat{R}^{+}_{\vec{k}}\hat{R}^{-}_{\vec{k}} + \hat{R}^{-}_{\vec{k}}, \hat{R}^{+}_{\vec{k}}\right) \tag{1.23}$$

Hence, the Dicke states are the common eigenstates of $\hat{R}^{2}_{\vec{k}}$ and $\hat{R}^{(3)}_{\vec{k}}$. It is important to note here the analogy with angular momentum operators. Eq. 1.4.1 corresponds to the angular momentum algebra with the $\hat{R}^{2}_{\vec{k}}$ and $\hat{R}^{(3)}_{\vec{k}}$ operators defined in terms of the raising and lowering operators accordingly to the definitions for the two-level an non-interacting atoms:

$$\begin{aligned}S^{(j)}_{-} &= |\downarrow\rangle_j\langle\uparrow|_j \\ S^{(j)}_{+} &= |\uparrow\rangle_j\langle\downarrow|_j\end{aligned} \tag{1.24}$$

where $|\downarrow\rangle_j$ and $\uparrow\rangle_j$ are the ground and excited states for the $j-th$ atom.

Dicke states are labeled by their eigenvalues, c, m ($c \in [0; N/2]$ and $m \in [-c; c]$). The cooperative number, c denotes the symmetry of the state relatively with the laser excitation (i.e. reflects how the superposition of the atomic states is symmetric or not relatively to the exchange of atoms), and m refers to the inversion of population of the Dicke state [70]. These values satisfy:

$$\begin{aligned}\hat{R}^{(3)}_{\vec{k}}|c,m\rangle &= m|c,m\rangle \\ \hat{R}^{2}_{\vec{k}}|c,m\rangle &= c(c+1)|c,m\rangle\end{aligned} \tag{1.25}$$

In [70], the Dicke states are labeled as as $|j,c\rangle$ (j is the number of atoms in the Rydberg state $j = N/2 - m$, and c remains as the cooperative number). Then their range of values will be: $j \in [0;N]$ and $c \in \left[|\frac{N}{2} - j|; \frac{N}{2}\right]$. Due to the symmetry of the laser excitation, only the states with the same cooperative number c are coupled together by the laser field. For each pair of values (j,c), the number:

$$Nc = \binom{N}{\frac{N}{2} - c} - \binom{N}{\frac{N}{2} - c + 1}$$

accounts for the Dicke states degeneracy. The states with $c = \frac{N}{2}$ are called *fully symmetric states* and there is only one for each j value.

As an example, we show here the Dicke basis in the case of $N = 2$ atoms (it is possible only one) compared with the spin-1/2 basis of the ensemble.

For this case, a spin-1/2 basis that describes all possible states of the system can be: $\{|\downarrow\downarrow\rangle, |\uparrow\downarrow\rangle, |\downarrow\uparrow\rangle, |\uparrow\uparrow\rangle\}$. In order to treat the collective interaction between the system and the electromagnetic field, we change the basis to another one characterized by the quantum numbers c, the cooperative number that refers to the symmetry of the state, and j, which indicates the number of atoms in the Rydberg state. Thus for $N = 2$ atoms, $c \in [0,1]$, we have:

N	Spin-1/2 basis	$\|c;j\rangle$	Dicke basis
0	$\|\downarrow\downarrow\rangle$	$\|c=1;j=0\rangle$	$\|\downarrow\downarrow\rangle$
1	$\|\uparrow\downarrow\rangle$	$\|c=1;j=1\rangle$	$\frac{1}{\sqrt{2}}(\|\uparrow\downarrow\rangle + \|\downarrow\uparrow\rangle)$
1	$\|\downarrow\uparrow\rangle$	$\|c=0;j=1\rangle$	$\frac{1}{\sqrt{2}}(\|\downarrow\uparrow\rangle - \|\uparrow\downarrow\rangle)$
2	$\|\uparrow\uparrow\rangle$	$\|c=1;j=2\rangle$	$\|\uparrow\uparrow\rangle$

Table 1.3: Spin-1/2 and Dicke basis for $N = 2$ atoms.

all non-degenerate.

1.4.2 Description of the cooperative model

The advantage of using the Dicke basis regards to the electric dipole selection rules, which allow electromagnetic transitions only between the states with

the same cooperative number c. The statements done for the two-atom case can be easily extended to the N-atom system, where the formal analogy between the Dicke basis and the angular momentum algebra remains valid. For simplicity, we define $\mathcal{N}_e = -N/2 + j$ as the number of excited atoms. Once $\mathcal{N}_e$ is fixed, $\mathcal{N}_e + 1$ values of c are possible, see Fig. 1.6

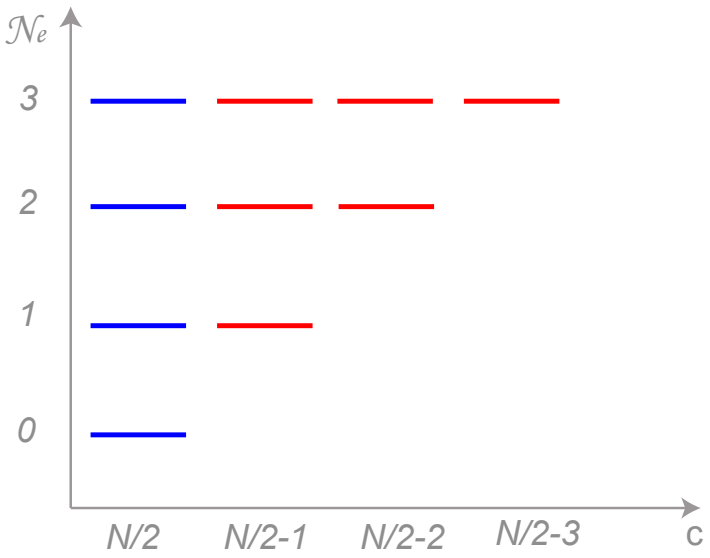

Figure 1.6: Schematic representation of the Dicke states: not degenerated symmetric states (blue) and degenerated non-symmetric states (red)

The quantum wave function of a system of N two-levels atoms evolves in a 2^N dimensional Hilbert space. Using 2^N linearly independent Dicke states it is possible to construct a quantum basis. Those states will be effectively coupled if the laser is resonant with the $|g\rangle \rightarrow |r\rangle$ and if the dipole moment of that transition is not zero. Within a Dicke basis, the states with $c = N/2$ are called fully symmetrical Dicke states. The fully symmetrical Dicke state with one Rydberg excitation corresponds to the Rydberg state populated in the case of a fully blockaded ensemble or, to the excited state of a superatom.

The Dicke collective states are defined in function of their symmetry relative to the electromagnetic field. Thus, it is possible to define the Dicke collective states such that the laser excitation only coupled the states with the same symmetry, greatly simplifying the problem.

In the case of a sample of non-interacting atoms, all of them behave identically and independently. If at time zero all the atoms are in the ground state, the system is in the state $|N/2, 0\rangle$ and following the selection rules, only states of the type $|N/2, \mathcal{N}_e\rangle$ can be reached. The coupling constant between the state with $\mathcal{N}_e$ and the state with $\mathcal{N}_e + 1$ is the collective Rabi frequency: $\Omega_{coll} = \sqrt{(N - \mathcal{N}_e)(\mathcal{N}_e + 1)} \cdot \Omega_0$. Thus, in this situation, all the

atoms of the system collectively oscillate at the single atom Rabi frequency, Ω.

To include the strong interactions between Rydberg atoms in the model has two effects on the Dicke collective states. The first one is that the states with the same number of excitations are no more degenerate in energy. The discrete levels become energy bands. Secondly, transitions between states with the same number of excitations but different cooperative numbers are induced. Fig. 1.7, taken from [70] represents qualitatively these two effects in the frame of an interacting Dicke basis.

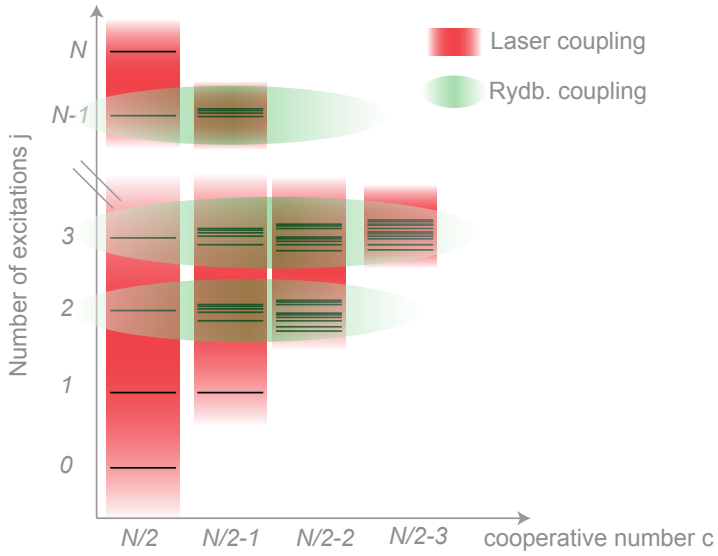

Figure 1.7: Dicke states in the interacting case . An electromagnetic field acts independently in each subset of states with the same symmetry (vertical axis), whereas the Rydberg-Rydberg interaction couples the states with the same number of excitation, j (horizontal axis). States with same j and c are no more degenerate in energy due to the van der Waals interactions (original from [70]).

Here it has been assumed that the only non-symmetric states populated are those ones with $c = N/2 - \mathcal{N}_e$, which comes from the fact that the number of these states is higher than the number of states with higher value of c. The population of those states can be transferred with a rate Γ only to states with a higher number of excitations, which excludes oscillations in the dynamics of the system. Additionally, when the system reaches a certain number of excitations the dipole blockade role becomes important, in a way that the radiation is not resonant anymore with the transitions between non-symmetric states. This causes the system to remain trapped in a region of the space of the states. To summarize, when looking at the properties

of symmetry of the laser excitation of an assembly of indistinguishable two-level atoms, there exists a basis which contains naturally those properties, the so-called Dicke basis. The cooperative model explains the behavior of interacting particles and shows how the symmetry properties of the collective states, caught through the coupling degree between the Dicke states, influences the dynamics of the system. Besides, the collective Dicke states contain the full statistical information about the collective Rydberg excitation and therefore allow the calculation of all the moments of the excitation statistics. The improved Dicke model, will be used in the frame of this Thesis as a support for the correct understanding of the experimental investigations on the excitation of Rydberg atoms off-resonance described in Ch.4.

Chapter 2

Experimental setup, excitation to Rydberg states and methods

In the present Chapter we describe the experimental apparatus in Pisa, employed to perform the majority of the experiments presented in this Thesis. In Ch.2.1 we describe in detail how we prepare the cold atomic ensembles used in Rydberg experiments. The procedure to excite atoms to Rydberg states as well as the process to detect them are explained in detail in 2.2. Additionally, we present the full counting statistics analysis as a useful tool in order to characterize strongly correlated systems like ours in Ch.2.3. A more detailed description of the experimental apparatus can be found in [71].

2.1 Preparing cold atomic samples for Rydberg studies

Our experiments are performed using 87-rubidium atoms in magneto-optical traps (MOTs) excited to different Rydberg states with principal quantum number n. The typical sizes of the MOTs used in the experiments presented in this Thesis vary from few tens of microns up to $\sim 200\,\mu$m, with typical peak densities at the center of the cloud around $n \approx 1 \cdot 10^{11}\,\mathrm{cm}^{-3}$. The realization of these clouds, which are considerably smaller than those typically used in cold atom experiments, requires particular attention on the aligment of the cooling beams and the use of high magnetic field gradients ($\sim 20\,$G/cm along the coil axis).

To realize the MOTs we use two different laser sources, the *cooling* and the *repumping* lasers, both of them in master-slave configuration. In Fig. 2.1 we show the scheme of the atomic levels used in the trapping process. The confinement of the atoms in the trap is done by the cooling laser, which is resonant to the transition $|5S_{1/2}; F = 2\rangle \rightarrow |5P_{3/2}; F' = 3\rangle$. Although much

less likely, an atom can make an off resonant transition into the $|5P_{3/2}; F' = 2\rangle$ state. When this happens, the atom is able to decay into the $|5S_{1/2}; F = 2\rangle$ or the $|5S_{1/2}; F = 1\rangle$ state. In order to avoid atoms in the $|5S_{1/2}; F = 1\rangle$ state to be excluded of the trapping process, the repumping light, resonant with the $|5S_{1/2}; F = 1\rangle \rightarrow |5P_{3/2}; F' = 2\rangle$ is applied. This cycle allows to confine and cool the rubidium atoms in the magneto-optical trap at the Doppler limit temperature, $T_D \simeq 150\,\mu$K.

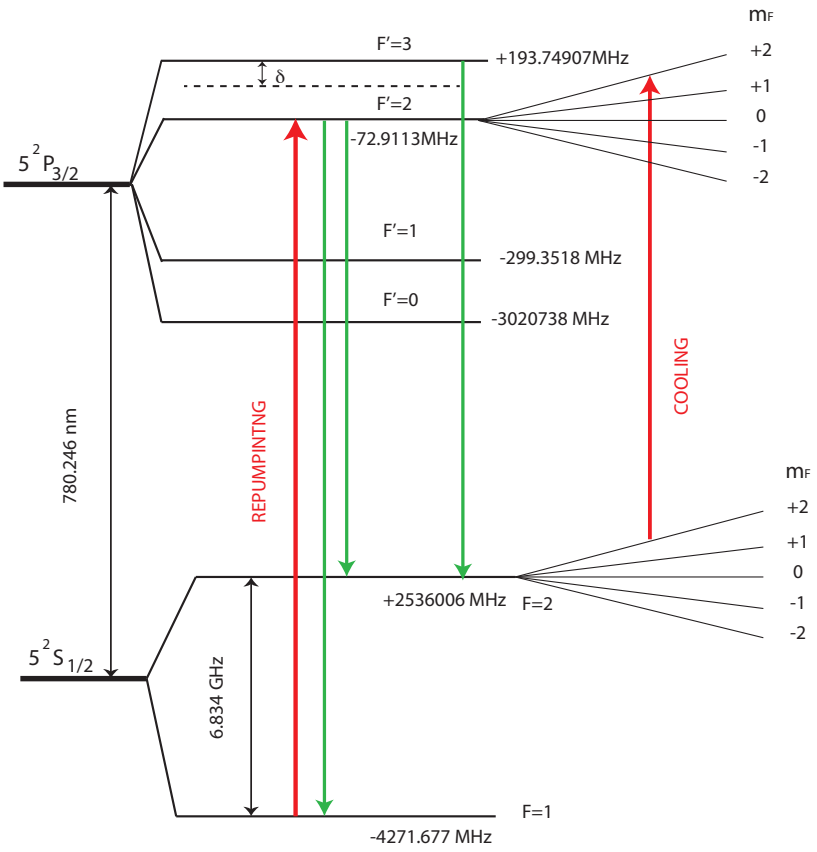

Figure 2.1: Level scheme of the magneto-optical trap (MOT), in which the cooling and repumping transitions are evidenced in red and the spontaneous decay in green.

The experimental apparatus consists of two quartz cells of sizes: $V_{big} = 80\,\text{mm} \cdot 47\,\text{mm} \cdot 47\,\text{mm}$ and $V_{small} = 70\,\text{mm} \cdot 24\,\text{mm} \cdot 18\,\text{mm}$, separated by a distance of 20 cm and connected by a graphite tube of 5 mm of internal diameter. Two ionic pumps from VARIAN connected to the two parts of the vacuum chamber generate the pressure gradient between the two cells, with 10^{-8} mbar inside the big cell and 10^{-10} mbar inside the small one. Two pairs of rubidium dispensers, consisting of electric resistances in which rubidium atoms are chemically bound to their surfaces, are placed close to the bigger

cell. An electric current heats the strips and thus induces a chemical reaction allowing atoms to be emitted into the system.

Inside each cell, a MOT presenting different geometries and functions, is created. The $2D+$ MOT is generated in the bigger cell by two pairs of circularly polarized counterpropagating beams of wavelength $\lambda = 780\,\text{nm}$ and waists of 12 mm. The beams are detuned by $\Delta = -2.4\Gamma$ from the $|5S_{1/2}; F = 2\rangle \rightarrow |5P_{3/2}; F' = 3\rangle$ transition, where $\Gamma = 6.055\,\text{MHz}$ is the natural linewidth of the $|5P_{3/2}; F' = 3\rangle$ level; and a repumper beam is added to them. The $2D+$ MOT gradient is $\sim 22\,\text{G/cm}$. The atoms are cooled in two dimensions, in a cigar shape cloud. In the same direction as the long axis of this cloud, a pushing beam is sent in order to transfer the atoms into the small cell, where the atomic flux loads the $3D$ MOT. In this case, three pairs of counterpropagating beams of waist of of 8 mm and power of of $\sim 5\,\text{mW}$ are used together with repumper light. These beams are detuned by $\Delta = -2.9\Gamma$ from the $|5S_{1/2}; F = 2\rangle \rightarrow |5P_{3/2}; F' = 3\rangle$ transition and the gradient of the $3D$ MOT is is $\sim 12.2\,\text{G/cm}$. The continuous load from the $3D$ MOT is lead by the flux from the $2D+$ MOT but also counteracted by atom loss processes, mainly due to the collisions with background atoms. During the experiments, the MOT is monitored by a CCD camera from DTA. This device collects a portion of the light scattered by the atoms and from this signal we calculate the number of atoms in the MOT as well as its size, with a statistical error of $\sim 10\%$ (the systematic error is estimated to be around a factor of 2 due to uncertainties in the calculation of the atom number from the scattered light collected by the camera).

2.1.1 Density variation techniques

Generating atomic clouds in different density regimes can be a way to study strongly interacting Rydberg systems in different scenarios, e.g., many-body collective effects [72, 73], or glassy features that Rydberg systems exhibit in the incoherent regime [30]. Here we describe two experimental techniques which allow us to work in different density regimes ranging from the single-atom regime to the high density regime.

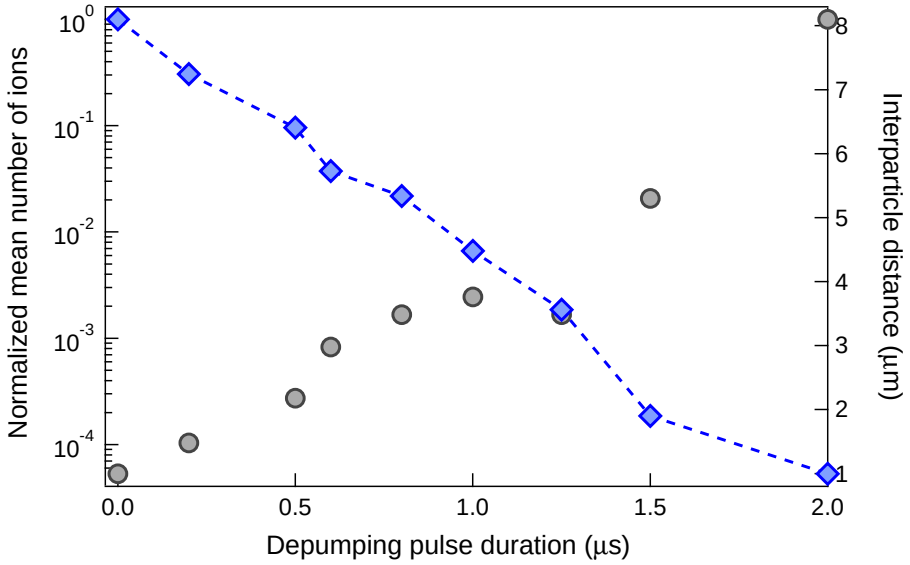

Figure 2.2: Variation of the number of ions as a function of the depumping pulse duration. On the left axis, we plotted the normalized number of ions obtained as a function of the duration of the depumping pulse (blue diamonds). The dashed line is a guide to the eye. On the right axis, we indicated the mean interparticle distance (grey circles).

The first one consists of depumping some of the atoms of the sample into a hyperfine level of the ground state not coupled to the Rydberg transition. This is achieved by irradiating the cloud with a pulse of laser light of intensity $I = 3.6 \cdot I_{sat}$ (where I_{sat} is the saturation intensity of the $|5S_{1/2}\rangle \rightarrow |5P_{3/2}\rangle$ transition), resonant with the transition $|5S_{1/2}; F = 2\rangle \rightarrow |5P_{3/2}; F' = 2\rangle$, after the MOT and the repumping beam are switched off. The $|5P_{3/2}; F' = 2\rangle$ state has a lifetime $\tau = 30\,\text{ns}$ and decays both to the $|5S_{1/2}; F = 2\rangle$ and to the $|5S_{1/2}; F = 1\rangle$ states, with a branching ratio of 1/5 [74]. Although atoms in the state $|5S_{1/2}; F = 1\rangle$ are still present in the atomic cloud, they are no longer coupled to the Rydberg transition due to the large energy difference between the sub-levels of the ground state ($\sim 6,8\,\text{GHz}$). This leads to a decrease in the effective density n_{eff}, i.e, the density of atoms in the $|5S_{1/2}; F = 2\rangle$ state. In order to measure n_{eff} using this technique, after the depumping pulse goes off, we directly photoionize the atoms of the cloud using an up to $2\,\mu\text{s}$ pulse of the 421 nm laser and measure the number of ions created. The photoionization technique will be explained in more detail in Ch. 2.2. We observed that the efficiency of this technique is maximum in absence of magnetic field. Consequenctly, the MOT magnetic field is switched off before illuminating the cloud with the depumping pulse.

Using this technique we manage to decrease the effective density of the

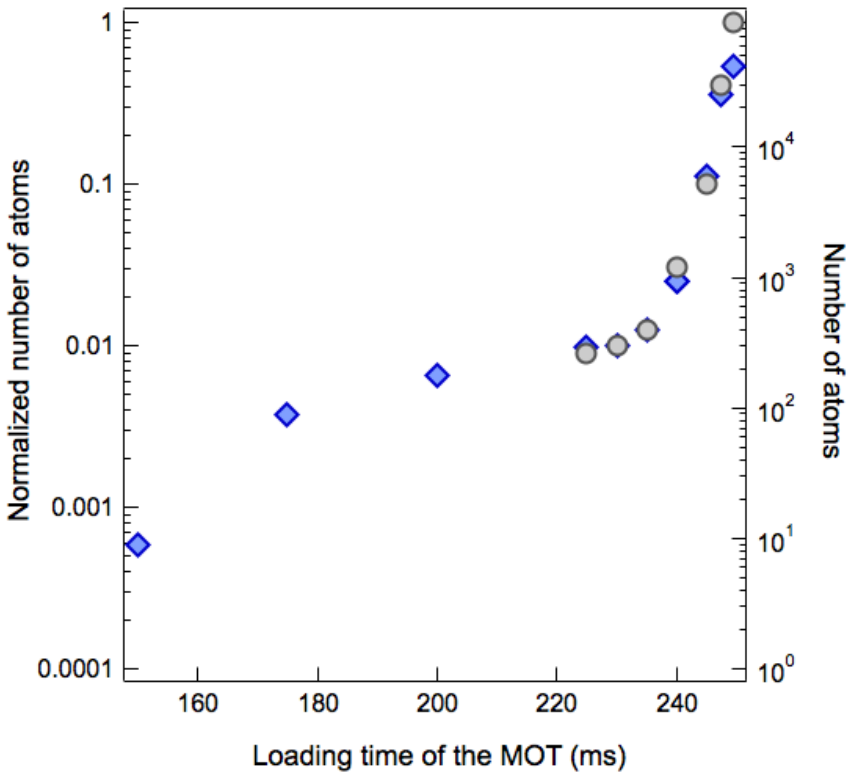

Figure 2.3: Variation of the number of atoms in the MOT as a function of the loading time. On the left axis, the normalized number of atoms in the MOT is plotted as a function of τ_{loading} in ms. On the right axis is shown the absolute value for each point. Grey circles indicate the number of atoms directly measured by the CCD camera (statistical error of $\sim 10\%$, systematic error estimated to be around a factor of 2). Blue diamonds correspond to the number of atoms calculated based on the number of ions measured when the sample is directly ionized. For both cases, the error bars are smaller than the symbols.

sample, while its size remains constant. In Fig.2.2 we plot the normalized number of ions as a function of the duration of the depumping pulse on the left axis (blue diamonds), and, on the right, we indicated for each case the averaged interparticle distance: a (grey circles) We observed that applying a pulse of duration up to $\tau_{\text{depump}} = 2\,\mu$s led to a decrease of the effective density of the sample by $3-4$ orders of magnitude, having clouds of $N \approx 10$ atoms. For τ_{depump} values longer than $2\,\mu$s, the efficiency of this technique decreased, which made difficult to reach the regime of a single atom (on average) in the cloud. These conditions, however, could be reached using the second technique, in which we reduce the loading time (τ_{loading}) of the MOT.

In Fig.2.3, grey circles indicate measurements of the number of atoms of the MOT obtained directly from the CCD camera. Below $N \approx 300$ atoms, the background noise made it impossible to obtain an accurate estimation of the atom number in this way. Hence, from this point (i.e., when $\tau_{\text{loading}} < 220\,\text{ms}$), N was deduced by photoionizing the sample and measuring the number of ions generated. Knowing N from the CCD measurement and the number of ions created in the photoionization experiment for a certain τ_{loading}, we extrapolate the value of N in the regime where the CCD measurement is not possible (blue diamonds in Fig.2.3). Regarding to the cloud size, we measure it using the CCD camera for τ_{loading} values up to $220\,\mu$s. As the measurements did not show significant variations, we assumed that the same behavior would be verified for lower values of τ_{loading}. As can be seen in Fig.2.3 using this technique we are able to reach a regime with $N \leq 10$ atoms. Thus, both techniques offer the possibility to generate clouds from several thousands to a few atoms. The variation of the loading time of the MOT allows us to reach the few atom regime, whereas the depumping technique presents the advantage that the effective density of the sample can be varied at any time of the experiment without changing the size of the cloud.

2.2 Generation and detection of Rydberg atoms

2.2.1 Excitation to Rydberg states

The excitation to the Rydberg states is achieved by using a two-photon excitation process. The scheme is shown in Fig.2.4. For the first step of the transition, $5S_{1/2} \rightarrow 6P_{3/2}$, we use a 840 nm MOPA laser $TA100$ from TOPTICA which is sent to a doubling cavity SGH 1004 also from TOPTICA, giving an output power at 421 nm of around 60 mW. In order to avoid population of the intermediate state, this laser is detuned by δ, ranging from $+300\,\text{MHz}$ to $+2\,\text{GHz}$.

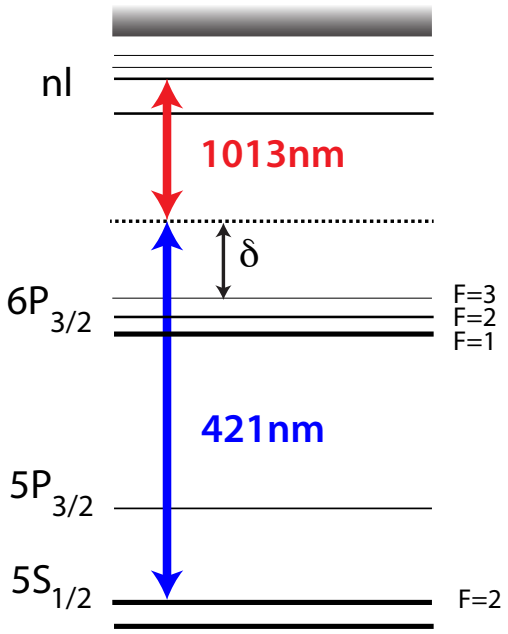

Figure 2.4: Excitation to Rydberg states using two-photon ionization scheme. The first step of the transition, $5S_{1/2}$ to $6P_{3/2}$, is done using a 421 nm laser source. This laser is detuned by 2 GHz in order to avoid population in the $6P$-level. The second step is done using a 1013 nm laser which allows us to reach the desired Rydberg state.

The second step of the transition, $6P_{3/2} \rightarrow nl$ is done using a $DL100$ diode laser from TOPTICA injected in a $TIGER$ laser from SACHER. Using this configuration, we a get typical output power at 1013 nm of 160 mW. Taking into account that we are able to control the ionizing electric fields up to $\sim 5\,\mathrm{V/cm}$, we can access to Rydberg states with principal quantum numbers ranging from $n = 55$ to $n = 120$.

The effective two-photon Rabi frequency is given by:

$$\Omega = \sqrt{\frac{\Omega_{Blue}\Omega_{IR}}{4\Delta} + \delta^2} \tag{2.1}$$

where δ is the detuning of the second transition laser with respect to the Rydberg state. In the following, the values of the Rabi frequency will be given on resonance ($\delta = 0$).

The stabilization in frequency of the Rydberg excitation lasers is done using a Fabry-Perot interferometer (TOPTICA FPI100). Both the 421 nm and the 1013 nm beams are coupled into the Fabry-Perot cavity together to a reference laser (of $\lambda = 780\,\mathrm{nm}$), locked to a known atomic transition. The FPI

used in our experiment is a piezoelectrically scanned device which combines a high finesse F, ($F \sim 120$for the 421 nm laser [71]) with the flexibility of using it as a stable reference cavity. A Labview program provides the interface to control the stabilization of the Rydberg excitation lasers. This is done by modulating the length of the FP cavity over its full free spectral range with a frequency of 200 Hz. On the transmission signal of the FP, four transmission peaks are identified, two of them correspond to the Rydberg excitation lasers, and the other two peaks belong to the reference laser. The latter ones serve as to determine a well defined relative frequency scale for the position at which other peaks appear. The program measures the relative positions of the transmission peaks and compares them to the reference position. The error signal is then sent to a PID110 TOPTICA module used to stabilize the laser frequency on the chosen value. This way the program is able to generate error signals from the transmission signal of the FP and use them to stabilize the Rydberg excitation lasers. Additionally, it is also possible to scan the 1013 nm laser by changing the reference position used to generate the error signal. The interface of the program shows the reading and setting of the relative motion of the laser frequency directly in MHz allowing to scan within a free spectral range FSR of the order of 1 GHz for a set wavelength. The linewidth of the Rydberg excitation (on the μs time scale), which is determined by the intrinsic quality of the Rydberg excitation lasers and the overall mechanical stability of the setup, has been evaluated in the past to be around700 kHz, so the main task of the FP is to stabilize the spectral lines against thermal drift during the measurement. In order to stabilize the temperature of the FP cavity it has been placed inside an isolated wooden box controlled by a heating system. Using this configuration the lasers remain locked for hours.

Depending on the requirements of the experiment, two different configurations based on the superposition of the excitation beams can be used. In Fig. 2.5 we show an schematic of these two configurations. The waist of the 1013 nmbeam is 110 μm, whereas the waist of the 421 nm beam varies depending on the selected configuration. In the *counterpropagating* or $3D$ configuration, the optical paths of the 421 nm and the 1013 nm are overlapped before entering in the quartz cell. In this case, the laser 421 nm laser presents a waist of 40 μm. We call this configuration the $3D$ configuration because the interaction volume has approximately the same size of the cloud, see Fig 2.5 (b). The focused $1D$ configuration in which a tightly focused 421 nm beam with with a waist of 6 μm is superimposed with the 1013 nm at 45° inside the quartz cell. In this case, the interaction volume can be approximated by a cylinder of base $S = \pi w_{Blue}^2$, and height $h = 2 \cdot \sqrt{2} w_{IR}$, see (a). In order to estimate the number of atoms contained in this volume, the spatial variation

of the density must be taken into account.

Let us assume that the density of the sample follows a gaussian distribution:

$$n(x,y,z) = n_0 \cdot e^{\left(\frac{-x^2}{\sigma_x^2}\cdot\frac{-y^2}{\sigma_y^2}\cdot\frac{-z^2}{\sigma_z^2}\right)} \tag{2.2}$$

Then, the total number of atoms in the MOT can be obtained as:

$$N_{at} = \int\int\int n_0 \cdot e^{\left(\frac{-x^2}{\sigma_x^2}\cdot\frac{-y^2}{\sigma_y^2}\cdot\frac{-z^2}{\sigma_z^2}\right)} \,\mathrm{d}x\,\mathrm{d}y\,\mathrm{d}z \tag{2.3}$$

Assuming also that the intensity of the beams is given by the expression

$$I_j = I_{0,j} \cdot e^{\frac{-2r^2}{\sigma_j^2}} \tag{2.4}$$

with $j = 421\,\mathrm{nm}, 1013\,\mathrm{nm}$.

Hence, given the total number of atoms in the MOT, N_{at}, the number of atoms within the interaction volume can be written as:

$$N_{V_{int}} = N_{at} \cdot \mathrm{erf}\left(\frac{\sqrt{2}\sigma_{Blue}}{\sigma_y}\right) \cdot \mathrm{erf}\left(\frac{\sqrt{2}\sigma_{Blue}}{\sigma_z}\right) \cdot \mathrm{erf}\left(\frac{2\sigma_{IR}}{\sigma_x}\right) \tag{2.5}$$

where erf denotes the error function.

During the entire excitation and detection sequence, the MOT beams are switched off in order to keep all the atoms initially in the ground state. A slightly modified version of this excitation scheme can be used to directly photoionize atoms [75, 34] by leaving the MOT trapping beams switched on, exciting, consequently, atoms to the $5P_{3/2}$-level.These atoms are then photoinized by applying a $1-2\,\mu$s pulse of the 421 nm laser. The ions produced are detected using the same electric field pulses as in the Rydberg detection. A detailed explanation of this excitation technique is given in Ch.3.2.2, in which the ions measurement be used as a reference to evidence the Rydberg excitation blockade.

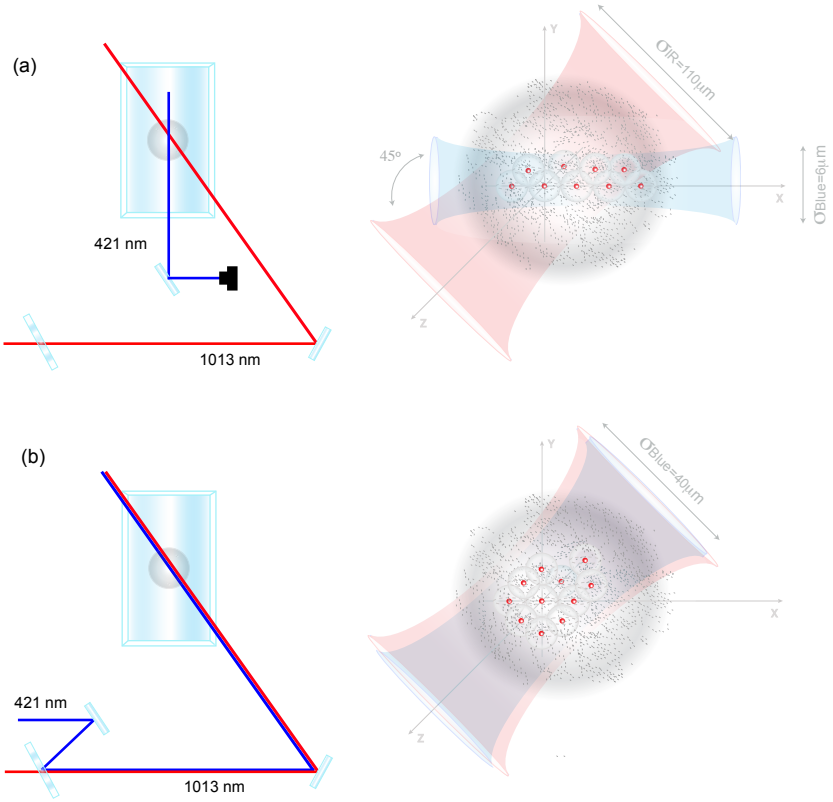

Figure 2.5: Optical paths of the 421 nm and 1013 nm laser. (a) Quasi $1D$ configuration. (b) $3D$ configuration. In both cases a detail of the overlapping of the beams with the MOT that helps to visualize the shape of the interaction volume is included (Drawings are not to scale, but designed to give complementary information not clear enough in the left figures).

2.2.2 Ionization and detection of Rydberg states

The extremely high sensitivity to electric fields of Rydberg atoms ($\sim n^{-4}$) is used in our experiment in the detection process.

In the Fig.2.6 we present a scheme of the quartz cell with the detection system. In the detection process, the sample is first field ionized using two pairs of plates applied on the external face of the quartz cell. The electric field needed in order to ionize a certain Rydberg state can be calculated using the following expression:

$$E_{Ion} = \frac{Ry^2}{4k(n - \delta^{n,j,l})e^3} \tag{2.6}$$

where $k = \frac{1}{4\pi\epsilon_0}$, e is the electron charge and $\delta^{n,j,l}$ is the Quantum defect theory correction to the principal quantum number. For the states used in this thesis the calculated ionization field is $\sim$ 16 V/cm (calculated for the $70S_{1/2}$ Rydberg-state, used in most of the experiments presented in this thesis).

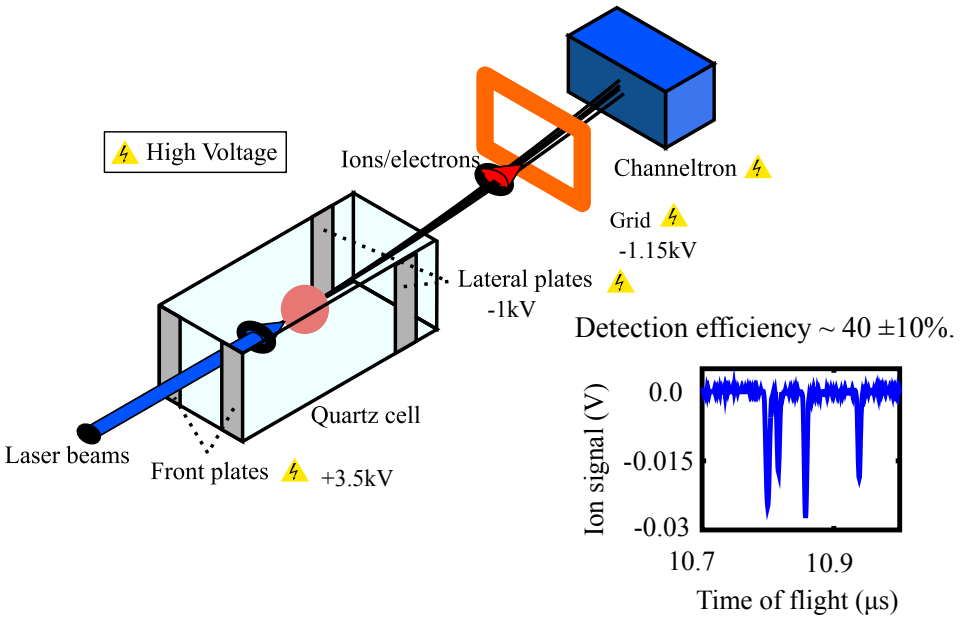

Figure 2.6: Experimental setup. In (a) The laser beams are superimposed so as to excite atoms within the same volume. In (b) the ion signal detected by the channeltron is presented.

The frontal plates are kept at $+3.5\,\mathrm{kV}$ while the voltage applied on side ones is $-1\,\mathrm{kV}$ and they remain switched on during $4.3\,\mu\mathrm{s}$ in order to avoid charging up the cell and the creation of an extra electric field acting on the atoms for a significant time. As a consequence of the screening effect due to the quarz cell, the field *seen* by the atoms is reduced, allowing us to ionize Rydberg states with a principal quantum number higher than $n = 52$.

The emitted ions are then guided towards the detector, a Channel Electron Multiplier (CEM) $KKBL510$, located around 15 cm from the center of the quartz cell. However, its position is not right on the axis determined by the atomic cloud position and the direction of the electric field of the ionization pulse. Thus a grid connected to a high voltage ($\sim 1.15\,\mathrm{kV}$) is used to guide the emmited ions towards the CEM. The channeltron has an internal gain determined by a potential, we set it to the maximum, $-2.5\,\mathrm{kV}$, in order to ensure the maximum detection efficiency. Finally, the output signal is acquired on the oscilloscope, the LeCroy WaveRunner, connected to a computer in which is installed the LabView program used to count the peaks, signal the arrival of the detected ions, with an accuracy better than 5%. Fig. 2.6(b) shows the typical signal of the arrival of the ions given by the oscilloscope. A limitation that our detection device presents comes from the minimum time interval between two peaks in order to be resolved (approximatly $10 - 20\,\mathrm{ns}$) and counted. Above a certain number of ions (typically approx. 40) the arrival times of the ions are too closely spaced, preventing us from counting the peaks. The experiments were performed for a number of detected ions below 40 in order to avoid saturation effects.

An important aspect in our experiments is to know precisely the number of Rydberg atoms we create. Assuming that all those Rydberg atoms are ionized by the electric field pulse and that we can determine the number of detected ions, from the observations we conclude that not all ions that are created and accelerated towards the channeltron are finally detected. Thus, knowing the efficiency of detection of our system becomes very important. Basically, two effects play a role here, the proportion of ions reaching the detector and the finite efficiency of the detector. The estimation overall detection efficiency for this setup, $\eta \approx 35 \pm -10\%$, has been reported in details in [75]. In that case, the determination of the detection efficiency consisted in comparing, during a photoionization process, the number of detected ions with an evaluation of the atomic loss from the cloud performed for different atomic densities and laser power values. For the experiments reported in this Thesis, a detection efficiency of our experiments of $\eta \approx 40\%$ was considered. Besides, except for the cases in which it is explicitly indicated, we show observed values, both for the mean number of ions ($\langle N\rangle_{obs} = \eta\langle N\rangle$) as well as for the standard deviations ($SD_{obs} = \eta SD$).

In the treatment of our experimental results, we consider that the processes involved in the detection efficiency follow a Poissonian statistics, which, as we will see in the following sections, will play a significant a role in the determination of the Rydberg excitations statistics.

2.2.3 Generation of off-resonant excitations: the technique of the seed

In this section we describe how to create a single Rydberg excitation, so-called the *seed*, which serves to start a sequential evolution process that ends with the generation of an avalanche of Rydberg excitations.

A laser pulse of duration τ is divided in two parts with different frequencies. The first part, with frequency ν, is resonant with the transition to the selected Rydberg state in order to create the seed. The second part, at frequency $\nu + \delta\nu$ happens off resonance and corresponds to the stage where the evolution and the avalanche take part.

In the experiments discussed in this Thesis we used two different configurations. The first one allows to realize a jump in frequency up to +30 MHz; this technique is limited both by the diffraction efficiency of the acousto-optic modulator (AOM),which decreases quickly as the AOM is operated at frequenices much below or above the centre frequency of 80 MHz , and by the shifting of the optical paths due to the different value of the radio frequency. A sketch of this configuration is reported in Fig.2.7 (a). As seen on it, an square pulse, beginning at τ_0 and of duration $\delta\tau$, is sent to an AOM which acts as a switch for the 421 nm laser beam. The accuracy of the switching on an off of the pulses is mainly determined by the AOM rise time: ~ 100 ns. The output radiation from this AOM is temporally divided in two parts, the first one resonant with the Rydberg transition (when the seed is created), and the second one off-resonant with the Rydberg transition.

As previously mentioned, the first configuration presented a limit of jumps up to +30 MHz. In order to work with detuning values higher than that, we employed a different experimental configuration. In this case, the 1013 nm laser path was modified in a way that the sample could be illuminated with two different orders of the radiation diffracted by the AOM in $m = 0, -1$. The sketch is represented in Fig.2.7 (b). The $m = 0, -1$ orders present a difference in frequency up to $\sim +80$ MHz. When the AOM was switched on, the $m = -1$ order of the 1013 nm beam, whose frequency was resonant with the Rydberg transition, illuminated the cloud for a duration τ_{seed}. After that, the AOM was switched off, and the MOT irradiated by the $m = 0$ order of the 1013 nm laser at a frequency shifted to the blue. Using this configuration, we are able to perform experiments in the range from +80 MHz

to +55 MHz, which is again limited by the efficiency of the acousto-optic modulator (AOM) and by the shifting of the optical paths. Even though we cannot realize experiments in between of +55 MHz and +30 MHz, the range we can cover using the techniques described above is enough in order to describe the dynamics in the off-resonant regime, as we will see in the following chapters.

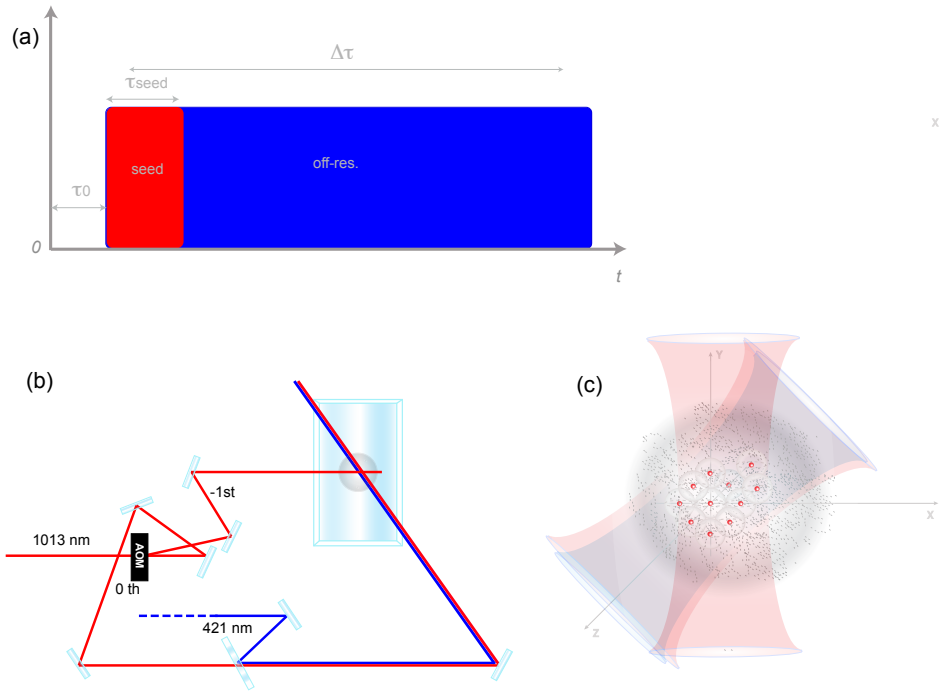

Figure 2.7: Optical paths of the $m = 0, -1$ orders of the 1013 nm beam. The off-resonant pulse comes from the $m = 0$ order of the 1013 nm beam and lasts for a total duration of Δt. When the AOM is switched on, a pulse of light resonant with the Rydberg transition of duration τ_{seed} (very short compared to the off-resonant one); illuminates the cloud generating a seed (see Ch. 4).

2.3 Full counting statistics in ultracold Rydberg atom samples

In order to study the evolution of the Rydberg atom systems, our experiments are repeated several times (typically, between 50-500) under the same conditions, in order to obtain sufficiently good statistics. For each single experiment the number of counts are registered on the CEM, allowing us to acquire the complete counting distribution, which represents the probability of registering a number k of counts in a single excitation. Apart from the mean number of Rydberg excitations, $\langle N \rangle$ and the variance, $\langle (\Delta N)^2 \rangle$, the

analysis of the full counting distribution as well as of the higher order statistical moments provides more insight into the properties of the system of study, as pointed out, e.g., in [76] for the phase transition of a spin $1D$ Ising model. Hence, the analysis of the full counting statistics contains important information regarding to the evolution of many-body systems, similarly to the methods recently used in condensed matter physics to unveil correlations in electronic transport processes [31, 32].

2.3.1 The Mandel Q-parameter

Besides the well-known importance of the the mean number, $\langle N \rangle$, and the variance, $\langle (\Delta N)^2 \rangle$ to characterize our results, there are some other statistical parameters, that can be obtained from the analysis of the full counting statistics of the excitation events, which result specially useful for our research. Of particular importance is the Mandel Q parameter, which describes the deviation from a Poissonian distribution [77]:

$$Q = \frac{\langle (\Delta N)^2 \rangle}{\langle N \rangle} - 1 \tag{2.7}$$

In the regime in which interactions are negligible each excitation to a Rydberg state is independent of all the others, which gives Q factor equal to zero because the variance is equal to the mean. The resulting distribution is close to a Poissonian distribution, with the deviation from a Poissonian caused by finite Rydberg excitation probability [**?**]. However, when the interatomic interactions are strong, the excitation processes are highly correlated [29], and one expects sub-Poissonian counting statistics, characterized by $Q < 0$. The minimum $Q = -1$ represents a theoretical case without any fluctuations. $Q > 0$ corresponds to super-Poissonian excitation statistics, which will be studied in more detail in Ch. 5.

In the limit of negligible interaction between the atoms, the dynamics of each atom is independent of that of the other atoms. Assuming that the excitation laser covers the whole sample and acts on each atom in the same way, the excitation probability is the same for all atoms [**?**]:

$$P_{exc} = \frac{\langle N_{Rydb} \rangle}{\langle N_a \rangle} \tag{2.8}$$

where $\langle N_a \rangle$ is the number of atoms in the sample. If each one of this atoms has 100% probablity to be excited to a Rydberg state, we obtain:

$Q = -P_{exc}$. Now we consider a "fully blockaded" Rydberg sample due to infinitely strong interaction between the excitation, where one atom is excited with probability 1, and excitation of this atom completely suppresses the excitation of any other atom. Hence, as stated above, in the case of non-interacting atoms the deviation of the atom counting statistics from a Poisson distribution is simply determined by the excitation probability P_{exc}, i.e. the finite ratio of the number N_{Rydb} of excited atoms to the number N_a of atoms in the gas cloud. Moreover, as is the case in the opposite limit of strong interaction, the value of Q does not depend on the time evolution of the excitation process, but just on the final number of excited atoms [**?**].

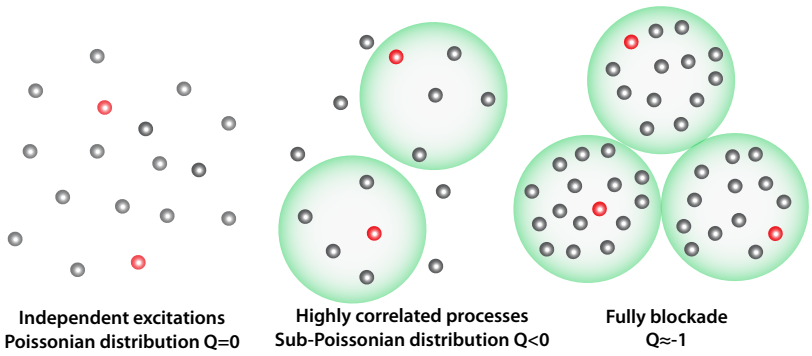

Figure 2.8: Representation of the different kind of interaction regimes in Rydberg atom gas: from the independent excitations to the fully blockaded regime. Also, the Q factor values are shown for each case.

It is important to point out here that these parameters were corrected by a factor which takes into account the efficiency of our measurements. Therefore, in the following chapters, all the results that will be presented will be already corrected by the detection efficiency, η,

$$\langle N_D \rangle = \eta \langle N \rangle \tag{2.9}$$

$$Q_D = \eta Q \tag{2.10}$$

where $\langle N_D \rangle$ and Q_D are the *detected* mean number of counts and Q factor.

2.3.2 Analysis of higher order moments of the counting distributions

As stated before, the full counting distribution provides more information of our system than an analysis of only the mean. The full counting statistics

$P(x)$ can be studied by analyzing the n-th order central moments (performed up to $n = 4$ in the experiments presented in the following pages)

$$\mu_n = \langle (x - \bar{x})^n \rangle \tag{2.11}$$

as well as their associated normalized quantities, shown in Table 2.1, as a function of the mean number $\bar{x}$. The full counting statistics can be studied with more accuracy by analyzing higher-order central moments of the counting distributions.

Associated Normalized Quantities	**Expression**
Mandel Q-factor (Q)	$Q = \mu_2/\bar{x} - 1$
Skewness (γ)	$\gamma = \mu_3/\mu_2^{3/2}$
Binder Cumulant (B)	$B = 1 - \mu_4/(3\mu_2^2)$
Bimodality Coefficient (b)	$b = (\gamma^2 + 1)/(\mu_4/\mu_2^2)$

Table 2.1: Associated normalized quantities to the n-th order central moments (up to $n = 4$) of a counting distribution.

The finite detection efficiency η in the experiment, which transforms the actual counting distribution $P(x)$ into an observed counting distribution $(P(x))_{obs}$:

$$(P(x))_{obs} = \sum_{y=x}^{\infty} \binom{y}{x} \eta^x (1-\eta)^{y-x} P(y), \tag{2.12}$$

which can be taken into account easily through the transformation to μ_n^F n-th factorial moments [78]:

$$(\mu_n^F)_{obs} = \eta^n \mu_n^F \tag{2.13}$$

We make use of the factorial moments here because they simplify the writing of the equations when one wants to include the finite detection efficiency. The relationship between the factorial moments and the real quantities (central moments μ_n) [79] is given by:

$$\mu_n = \sum_{i=0}^{n-1} \sum_{j=1}^{n-i} \left[(-1)^i \binom{n}{i} S(n-i, j) \right] \mu^i \mu_j^F + (-\bar{x})^n, \tag{2.14}$$

where $S(i, j)$ is the Stirling number of the second kind and $\bar{x}$ the mean of the distribution. Finally, the observed mean and the second, third and fourth central moments are then related to the actual central moments by

$$
\begin{aligned}
(\bar{x})_{obs} &= \eta\bar{x} \\
(\mu_2)_{obs} &= \eta^2\mu_2 + (\eta-\eta^2)\bar{x} \\
(\mu_3)_{obs} &= \eta^3\mu_3 + 3(\eta^2-\eta^3)\mu_2 + (2\eta^3-3\eta^2+\eta)\bar{x} \\
(\mu_4)_{obs} &= \eta^4\mu_4 + 6(\eta^3-\eta^4)\mu_3 + \left[6(\eta^3-\eta^4)\bar{x} + +(11\eta^4-18\eta^3+7\eta^2)\right]\mu_2 \\
&\quad +(3\eta^4-6\eta^3+3\eta^2)\bar{x}^2 + (-6\eta^4+12\eta^3-7\eta^2+\eta)\bar{x} \qquad (2.15)
\end{aligned}
$$

from which the observed values of the normalized quantities can be calculated (for the Mandel Q-factor, the particularly simple result $(Q)_{obs} = \eta Q$ holds). Alternatively, the above procedure can be used to calculate the actual central moments and normalized quantities from the observed ones.

Chapter 3

Resonant excitation dynamics of Rydberg ensembles

Atoms in high-lying Rydberg states interact with each other, either via van der Waals or dipole-dipole potentials [9], which are many orders of magnitude stronger than those between ground state atoms. Resonantly optically excited Rydberg samples [26, 80, 15, 13, 14, 81, 82, 29, 21, 22, 83] constitute a rich playground for the study of those interactions and their consequences. The dipole blockade effect [24, 84, 25, 26], which allows only a single excitation to the Rydberg state within the volume of the blockade sphere, or the manifestation of kinetic constraints [30] in analogy to glassy systems, are just two examples among the wide range of possibilities that those ensembles offer.Theoretical calculations of the coherent excitations dynamics are difficult because of the exponential growth of the computational resources required with N. Thus, for small numbers of particles it is possible to solve directly the Schrödinger equation, whereas in case of large N, the master equation has to be approximated to a rate equation [85], or numerical simulations techniques, like the MCWF (Monte Carlo Wave Function) [86, 87], can be used alternatively to approach the solution of the master equation. From the experimental side, the observation of the universal scaling laws with density and laser intensity provide earlier evidence of the coherent dynamics [80], recently observed for an N-atom system on the μs timescale [81, 21]; whereas the predictions for the incoherent regime have not been verified and they are a subject of study nowadays [85, 30].

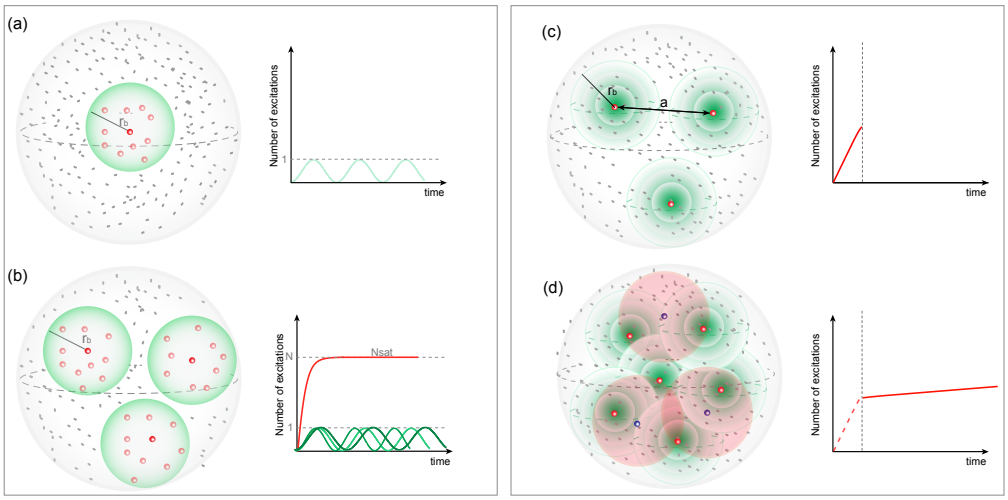

Figure 3.1: Different regimes of Rydberg excitation dynamics: (a)-(b) coherent, (c)-(d) incoherent. (a) Coherent dynamics of a single superatom. A single Rydberg excitation is shared collectivelly by all the atoms contained in the blockade sphere. The population of this system, which is described as a two-level system, oscillates between the ground and the excited state with collective Rabi frequency Ω_{coll}. Coherent dynamics are observed via Rabi oscillations. (b) When more excitations are generated, each blockade sphere is considered like an independent superatom. The number of Rydberg excitations measured at a certain time is the sum of the contributions of all the superatoms present in the cloud. The dynamics (red) exhibits a fast growth for short excitation times and saturates for long times to a value N_{sat}, as a sign that the sample is fully blockaded. (c) In the incoherent case, initially Rydberg excitations are generated independently. The interactions between them do not affect the dynamics, and the number of excitations increases linearly. (d) As the time increases, the space available for generating new excitations, gets tighter (nearest neighbors are closer and interact strongly preventing the generation of new Rydberg atoms). This effect becomes more pronounced in the high density regions of the sample. Ground state atoms located in the available space keep a low (but non-zero) probability of being excited if the time of interaction with the laser field is large enough (red spheres). As a consequence, a slowing down of the dynamics is observed.

In this chapter we report on the realization of a resonantly excited Rydberg gas and the study of the strong atomic interactions within this system. After a short review of the mathematical description of the single atom dynamics, we approach the N-atom system. There, we focus our studies on the characterization of coherent and incoherent excitation, the verification of

the time-scaling laws [80] predicted for each case, as well as the estimation of the coherence time of our system. Those results motivated a deeper investigation of the role that Rydberg interactions play under these conditions both in the saturated regime as well as before reaching the stationary state. Hence in Ch. 3.2.1 we studied the Rydberg dynamics before reaching the saturated regime, where kinetic constraints are expected to become manifest [30] giving rise to characteristic features of the dynamics like an increase of the relaxation time scale of the atomic ensemble (see Fig. 3.1); whereas, in Ch.3.2.2 a method to spatially visualize the effect of dipole blockade inside a cold atomic cloud is presented.

3.1 Theoretical description of the evolution of a resonantly excited Rydberg system

In this section we want to study the effect of the relaxation terms on the dynamics of a two-level atom Rydberg sample. Before approaching the many-body problem, we present here some basics of the mathematical description of the behavior of the a single atom and some qualitative aspects of the dynamics of a Rydberg atoms system that can be seen from a single atom model.

3.1.1 Single atom case

We considered a single two-level atom interacting with a light field of Rabi frequency, Ω_0. The optical Bloch equations (OBE) can be written as [88]

$$\begin{cases} \frac{d\tilde{\rho_{eg}}}{dt} = -(\gamma_\perp - i\delta)\tilde{\rho_{eg}} + \frac{i\omega\Omega_0}{2} \\ \\ \frac{dw}{dt} = -\gamma_\parallel(\omega + 1) - i\Omega_0(\tilde{\rho_{eg}} - \tilde{\rho_{ge}}) \end{cases} \tag{3.1}$$

In the absence of relaxation terms, $\gamma_\perp, \gamma_\parallel = 0$, the population oscillates between the ground $|g\rangle$ and the excited state, $|e\rangle$ at frequency Ω around the stationary value: $\langle N_e = \frac{1}{2}\rangle$. Our case of study, instead, presents $\gamma_\perp, \gamma_\parallel \neq 0$ in a regime where the population of the ground and the excited states changes slowly with respect to the coherences, i.e. $\gamma_\parallel << \gamma_\perp$. The coherences follow an adiabatic evolution of the populations that result almost stationary on time $\gamma_\perp^{-1}$.

Thus, the system of equation 3.1 can be solved by imopsing an *adiabatic approximation*.

From the first equation 3.1 we obtain:

$$\begin{cases} \tilde{\rho_{eg}} = -e^{(\gamma_\perp - i\delta)t} \int \tilde{c} e^{-(\gamma_\perp - i\delta)t} \, \mathrm{d}t = \frac{\tilde{c}}{(i\delta - \gamma_\perp)} \\ \\ \frac{d\omega}{dt} = -\gamma_\parallel(\omega + 1) - \Omega^2 \left[\frac{\gamma_\perp}{\gamma_\perp^2 + \delta^2} \right] \omega \end{cases} \tag{3.2}$$

Then, the second equation can be solved, by setting as initial condition $\omega(0) = -1$:

$$\omega(t) = \frac{\gamma_\parallel(\gamma_\perp^2 + \delta^2) + \gamma_\perp \Omega^2 e^{-t\left(\gamma_\parallel + \frac{\gamma_\perp}{\gamma_\perp^2 \delta^2}\Omega^2\right)}}{\gamma_\parallel(\gamma_\perp^2 + \delta^2) + \gamma_\perp^2 \Omega^2} \tag{3.3}$$

Doing this we obtain the characteristic population inversion rate:

$$\Gamma \sim \gamma_\parallel + \gamma_\perp \frac{\Omega^2}{\gamma_\perp^2 + \delta^2} \tag{3.4}$$

where, the first term is determined from the relaxation of the populations, $\gamma_\parallel$, and the second one, defined as excitation rate, depends on the Rabi frequency, Ω. For long excitation times, the system reaches the stationary value predicted for the average population of excited state:

$$\langle N_e \rangle = \frac{1}{2 + 2\frac{\gamma_\parallel}{\gamma_\perp}\left(\frac{\gamma_\perp^2 + \delta^2}{\Omega^2}\right)} \tag{3.5}$$

This equation predicts that in the limit of low spontaneous emission, $\gamma_\parallel$, the population of the excited states reaches the value $\frac{1}{2}$ independently of the detuning, contrary to what is expected for coherent radiation.

3.1.2 Excitation dynamics of strongly interacting many-body systems

The study of the dynamics of an ensemble of N strongly interacting atoms presents the additional difficulty of the exponential growth of the Hilbert space with N. For systems of a limited number of particles, the Schrödinger equation can be solved analytically for coherent dynamics [89, 90, 16, 91]; whereas, under strongly dissipative conditions, the master equation must be approximated by a rate equation, whose basis grows linearly with N [92, 93].

Alternatively, different numerical simulation techniques (equivalent to the master-equation treatement) were proposed in order to gain more physical insight into those systems, like the wave-function Monte Carlo (MCWF) technique[86, 87]. A method specifically developed for the blockaded Rydberg ensemble is the so-called, superatom model [90, 94, 95], which combines the description of a non-fully blockaded ensemble with the results obtained for the case of a fully blockaded one. Let us consider a cloud formed by N atoms placed in a sphere of radius r_b with only one Rydberg excitation present in it, i.e. the sample is fully blockaded. The behavior of such a system can be described using the single-atom equations, detailed in Ch.3.1.1, by treating the whole system as a two-level atom. This approximation, known in Rydberg literature as *superatom*, is necessary because a more rigorous treatment of the problem would require to take into account the different contribution of the relaxation terms $\gamma_{\parallel}$ and $\gamma_{\perp}$, that here we assumed: $\gamma_{\parallel} = \gamma_{\perp} = 0$. The laser field couples coherently the ground state $|g\rangle$ and the symmetric excited state of the superatom $|r\rangle$ with amplitude:

$$\left[\frac{\Omega_{coll}^2}{\Omega_{coll}^2 + \delta^2}\right] \tag{3.6}$$

The average population of the Rydberg state within the superatom oscillates with collective Rabi frequency, Ω_{coll}, around the stationary state $\langle N_r \rangle_{SS}$. By keeping $\gamma_{\perp} = 0$, the presence of a relaxation term $\gamma_{\parallel} \neq 0$ damps the oscillations until the stationary state is reached, whose average population presents an upper limit equal to 1/2. Under these conditions, the superatom behaves exactly like a single two-level atom. The experiments presented in this thesis were performed in atomic ensembles of N atoms randomly distributed in a cloud of size bigger than the blockade radius, so the sample can be divided into blockade spheres, which can be treated as independent superatoms. The spatial dependence of the density distribution of the ground state atoms, $n(r)$, results in a variation of the number of ground state atoms inside each superatom, which can be calculated by summing the populations of all the superatoms present in the sample at a time τ:

$$\langle N_r \rangle_{\tau} = \int n_R(r) \sin^2\left(\frac{1}{2}\Omega_{coll}(r)\tau\right) \mathrm{d}^3 r \tag{3.7}$$

This integral sums the contribution of each superatom whose population oscillates with $\Omega_{coll}(r) = \sqrt{\tilde{N}}\Omega$. The saturation curve [80] shows an initial linear increase with time and a saturation to a constant value N_{sat}. Both

the slope of the curve and the value of N_{sat} have been used to characterize either the type of dynamics, (coherent, coherent collective or incoherent), as well as the underlying interaction (non-interacting or strongly interacting), by studying the scaling of the excitation time with the density of the ground state atoms and the Rabi frequency [80, 16]. In this thesis we focus on the study of the incoherent dynamics of a Rydberg ensemble. As we will see in the following pages, the aforesaid scaling laws, specially the ones with the Rabi frequency, will be used to justify that we are in conditions of incoherent evolution.This problem, that has been recently approached theoretically in [30], where the authors directly solve the equations of the dynamics of a sample of N interacting atoms that evolve in the incoherent regime.

The description of the two-level system is done by using the spin 1/2 formalism, representing for each atom the ground state as $|\downarrow\rangle$ and the excited state as $|\uparrow\rangle$. The Pauli matrices are indicated as $\sigma^k_{x,y,z}$ and $n_k = (1+\sigma^k_z)/2$ is the projector onto the excited state. Additionally, the excitation time was rescaled as: $\tau = t \cdot (\Omega^2/\gamma_\perp)$. In order to calculate the excitation rate in [30] the authors study the evolution of the density matrix:

$$\begin{cases} \partial_t \rho = \mathcal{L}_0 + \mathcal{L}_1 \\ \mathcal{L}_0 = -i[H_0, \rho] + \delta_\perp + \sum_{k=1}^{N} (n_k \rho n_k - \frac{1}{2}\{n_k, \rho\}) \\ \mathcal{L}_1 = -i\Omega \sum_{k=1}^{N} [\sigma^k_x, \rho] \end{cases} \tag{3.8}$$

where H_0 is the Hamiltonian of the system:

$$H_0 = -\sum_{k=1}^{N} \delta n_k + \sum_{k,m} \frac{V_{k,m}}{2} \tag{3.9}$$

$\mathcal{L}_0$ and $\mathcal{L}_1$ are the Lindblad terms, which account for the incoherent processes such as decay or dephasing. Here, $\mathcal{L}_0$ and $\mathcal{L}_1$ describe the fast and the slow part of the dynamics, respectively. The interest is focused on the regime where $\mathcal{L}_0$ dominates, i. e., $\gamma_\perp >> |\Omega|$, which is the incoherent regime. The authors approximate the master equation as an *effective* master equation where the fast dynamics has been integrated out.

This analysis can be interpreted by observing that, in the limit $\Omega^2 >> \gamma_\perp \gamma_\parallel$, the population dynamics in the Bloch equations is characterized by the excitation rate:

$$\Gamma = \frac{\Omega^2}{\gamma_\perp}\left(\frac{1}{1+\frac{\delta^2}{\gamma_\perp^2}}\right) \tag{3.10}$$

and in case of atomic interactions of the kind of:

$$V_{j,k} = \frac{C_\alpha}{|r_k - r_j|^\alpha} \tag{3.11}$$

with $\alpha = 6$. In the denominator of Eq. 3.10, it is necessary to replace $\hbar\delta$ by $\hbar\delta - \frac{C_\alpha}{|r_k - rj|^6}$ in order to account for those interactions. At this point, the theoretical interpretation becomes hard due to the random positions of the atoms within the sample, the authors solve this problem by placing the atoms in a regular lattice of a certain spacing, which allows them to express all the distances as a function of the spacing of the lattice. In our case, although the atoms are randomly distributed in the cloud we were able to apply the same simplification by expressing all the distances as a function of the mean interparticle distance among the atoms of the sample, a. This allows one to define an *interaction* term, which depends on the interaction strength among the atoms, C_6, as well as on the mean distance between excitations, a.

$$R = \frac{1}{a}\left(\frac{C_6}{\hbar\gamma_\perp}\right)^{(1/6)} \tag{3.12}$$

From here, it is possible also to introduce the rescaled detuning Δ as:

$$\Delta = \frac{\delta}{R^6\gamma_\perp} \tag{3.13}$$

Note that the excitation rate of the single atom depends on the interactions with atoms in the excited state with occupation n_j

Hence, it is possible to rewrite Eq. 3.10 as:

$$\hat{\Gamma} = \frac{1}{1+\epsilon_k^2} \tag{3.14}$$

where:

$$\epsilon_k = R^6 \left[\Delta - \sum_{j \neq k} \frac{n_j}{|r_k - r_j|^6} \right] \tag{3.15}$$

Finally, the excitation rate of the k^{th} atom case is:

$$\Gamma_k = \frac{\Omega^2}{\gamma_\perp} \cdot \frac{1}{1 + [R^6(\Delta - \sum_{j \neq k} \frac{n_j}{|\hat{r_k} - \hat{r_j}|^6})]^2} \tag{3.16}$$

The equation accounts for the interaction between atoms through the single atom detuning δ, plus the energy shift caused by the neighboring Rydberg atoms:

$$R^6 \cdot \sum_{j \neq k} \frac{n_j}{|\hat{r_k} - \hat{r_j}|^6} \tag{3.17}$$

An increase of this product means stronger interactions within the system, which leads to a decrease of the excitation rate because in the vicinity of excited atoms the dynamics are slowed down due to the effect of the Rydberg-Rydberg interactions.

More insight into the relaxation dynamics can be gained by doing the mean field analysis, which allows us to rewrite the equation for the Rydberg density as:

$$\partial_t \rho(\tau) = \frac{1 - 2\rho(\tau)}{1 + [\sum_k |r_k|^{-\alpha} \cdot R^\alpha \rho(\tau)]^2} \tag{3.18}$$

whose stationary solution is compatible with the expected result for a system of N non-interacting atoms:

$$\rho_{\text{stationary}} \equiv lim_{\tau \to \infty} \rho(\tau) = 1/2 \tag{3.19}$$

This intuitively leads to the state in which all the atoms in the sample reach the equilibrium between the populations of the ground and the excited state. Integrating the equation 3.18 and imposing as initial condition $\rho(0) = 0$, the implicit equation for $\rho(\tau)$ has the form:

$$\tau = -(1/8)[4 + \left(\sum_k |\hat{r_k}|^{-\alpha}\right)^2 R^{2\alpha}] \times log(1 - 2\rho(\tau)) - \\ 1/4 \cdot \left(\sum_k |\hat{r_k}|^{-\alpha}\right)^2 R^{2\alpha}(\rho(\tau) + 1)\rho(\tau) \tag{3.20}$$

From Eq. 3.20 it is possible to distinguish three different excitation time regimes, depending on the value of τ:

- $\rho(\tau) << 1/2$ (short excitation times). In this case the solution of Eq. 3.20 has the form: $\rho(\tau) = e^{-\tau} sinh(\tau)$, which means that the number of excitations grows independently of the atomic interactions. This behavior occurs at the beginning of the excitation process, where, assuming that the Rabi frequency is uniformly distributed across the sample, the new excitations are randomly distributed in the cloud and separated enough in order to ensure that they do not influence the dynamics of the rest of the atoms.

- $\rho(\tau) \approx 1/2$ (long excitation times). Here the Eq. 3.20 solution looks like $\rho(\tau) \approx [1 - exp(-8\tau/(4 + F_\alpha^2 R^{2\alpha}))]/2$. In this case the system approaches to the stationary state, independently of the atomic interactions. All the atoms in the sample reach the equilibrium between the population of the ground and the excited state at the expected value $\rho(\tau) \approx 1/2$. The dynamics is blocked because there are no more atoms in the cloud that can be excited to the Rydberg states.

- $\rho(\tau) << 1/2$ (intermediate times), but the product $R^\alpha \rho(\tau) >> 1$. Under these conditions, the Eq. 3.20 solution adopts the form $\rho(\tau) \sim [3/(R^{2\alpha} F_\alpha^2)]^{1/3} \tau^{1/3}$. This constitutes the most complex situation because, when the excitation time is increased, the volume size available to get a new Rydberg excitation without considering the interactions decreases. As a consequence, a slowing down of the dynamics is observed.

The size of the excluded volume, defined as the space available for generating a new excitation (see Fig. 3.1 (d)); decreases with time, representing a key factor of these dynamics. Thus, in the dipole blockade regime the laser linewidth , $\gamma_\perp$ defines the minimum distance between two Rydberg excitations,r_b, in a way that the generation of subsequent excitations within the volume defined by r_b is blocked. However, a ground state atom located at a distance lower than r_b from a Rydberg excitation, exhibits a very slow dynamics and, therefore, has a very low but non-zero probability of being

excited to the Rydberg state. In fact, if the time of interaction with the laser field is long enough, then the excitation to the Rydberg state can happen. In this sense the sample is not divided in rigid blockade spheres but in regions in which the excitation rate is large or small. This property is not contained in the mean field analysis, where all the atoms of the sample are considered equal. The authors obtain the dynamics in this limit by solving the effective master equation: $\mu = \mathcal{P}\rho = lim_{t\to\infty} e^{\mathcal{L}_0 t}\rho$. This shows a heterogeneous evolution of the atomic system characterized by large fluctuations within the relaxation time. Another aspect that is not considered in the mean field approximation is the hierarchic evolution of the excitations. Each atom excited to the Rydberg state conditions the successive excitations of its neighboring atoms so, but there is no "sharing" of excitation as in the case of coherent collective excitation.

3.2 Coherent versus incoherent Rydberg dynamics

The scaling laws for Rydberg dynamics [80] predict a linear dependence of the timescale with the Rabi frequency in the coherent regime and a quadratic dependence for the incoherent case. In our case we verify these laws by measuring the dynamics of a Rydberg ensemble for three different values of the Rabi frequency: $387 \pm 77\,\mathrm{kHz}$ (red diamonds), $207 \pm 41\,\mathrm{kHz}$ (blue diamonds) and $98 \pm 20\,\mathrm{kHz}$ (grey diamonds). The experiment was performed in a MOT of $N = 70000$ atoms and sizes $V = 92.4\,\mu\mathrm{m} \cdot 42.9\,\mu\mathrm{m} \cdot 62.9\,\mu\mathrm{m}$, where Rydberg excitations are generated under resonant conditions ($\delta = 0$) using the $3D$ configuration of the 421 nm laser source, see Ch.2. In Fig. 3.2 (a) we present the measurements of the mean number of excitations as a function of time.

Rescaling the excitation times with the expected law in case of coherent dynamics, ($\tau_{resc} = \tau_{exc} \cdot \Omega$), the curves diverge since $\tau_{resc} \approx 0.23$ ($\tau_{exc} \approx 1\,\mu\mathrm{s}$), see the open symbols in Fig. 3.2 (b); meaning that our system does not evolve coherently. By contrast ,when the times are rescaled according to the incoherent dynamics law, $\left(\tau_{resc} = \tau_{exc} \cdot \frac{\Omega^2}{\gamma_\perp}\right)$, solid symbols in Fig. 3.2 (b); the three curves lie on the top of each other, which demonstrates the incoherent evolution of the of our system.

In order to gain more insight into the coherent dynamics of our system, limited by the laser linewidth, $\gamma_\perp = 0.7\,\mathrm{MHz}$, we focus the measurements in the time range $\tau_{resc} = [0 - 6]$. In this experiment we use a MOT of $N = 162000$ atoms and size $V = 109\,\mu\mathrm{m} \cdot 55\,\mu\mathrm{m} \cdot 77\,\mu\mathrm{m}$. In Fig. 3.3 we show the mean number of excitations as a function of time, already rescaled

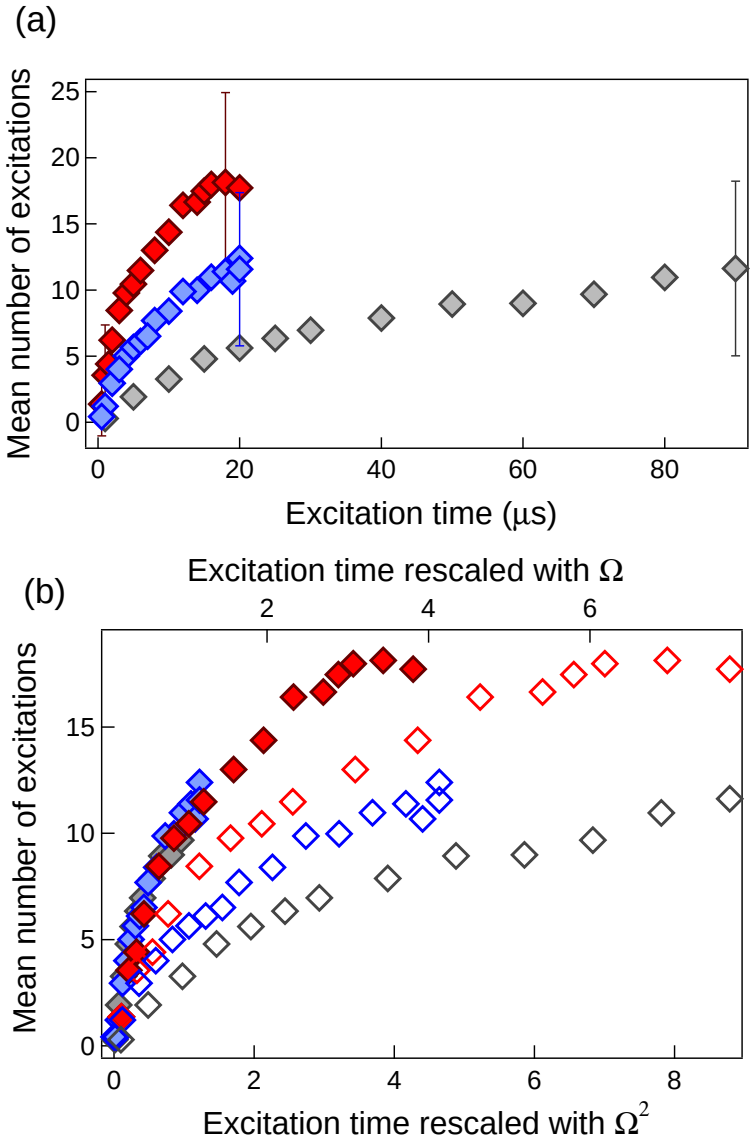

Figure 3.2: (a) Resonant dynamics of a Rydberg system in the $3D$ configuration varying the Rabi frequency value: 387 ± 77 kHz (red diamodns), 207 ± 41 kHz (blue diamonds) and 98 ± 20 kHz (grey diamonds). The error bars correspond to one standard deviation of each set of data. (b) Data from (a) rescaled according to the coherent dynamics law ($\tau_{resc} = \tau_{exc} \cdot \Omega$, open symbols), and according to the incoherent dynamics law ($\left(\tau_{resc} = \tau_{exc} \cdot \frac{\Omega^2}{\gamma_\perp}\right)$, solid symbols).

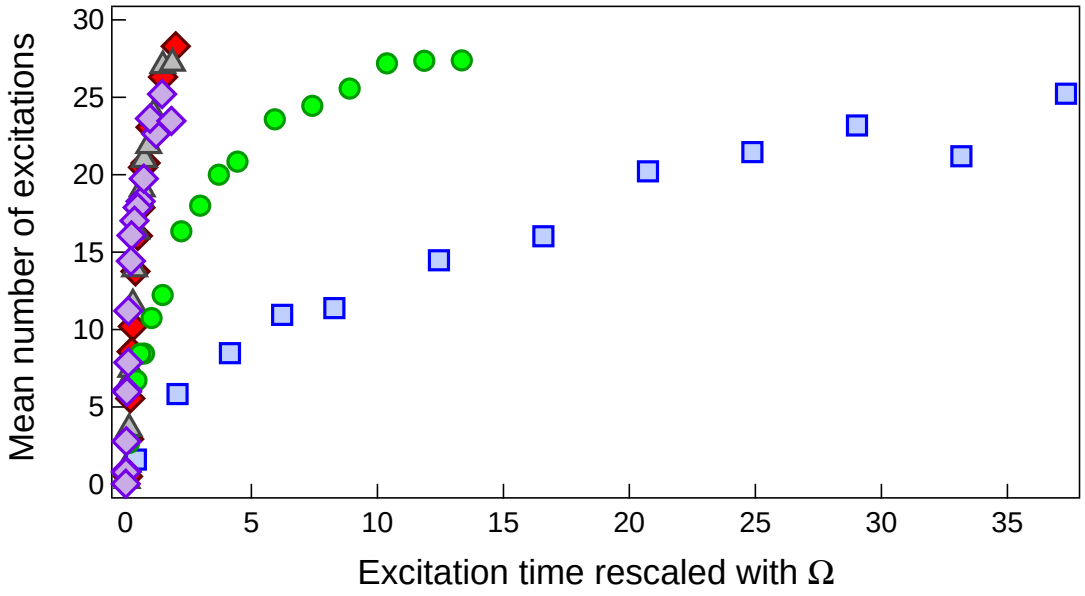

Figure 3.3: Resonant dynamics f in $3D$ configuration varying the values of the Rabi frequency: $982 \pm 196\,\mathrm{kHz}$ (red diamonds), $745 \pm 149\,\mathrm{kHz}$ (grey triangles), $414 \pm 83\,\mathrm{kHz}$ (violet diamonds), $148 \pm 30\,\mathrm{kHz}$ (green circles) and $122 \pm 24\,\mathrm{kHz}$ (blue squares). The sample had $N = 162000$ atoms and size $V = 109\,\mu\mathrm{m} \cdot 55 \cdot\ \mu\mathrm{m} \cdot 77\,\mu\mathrm{m}$ and density $n = 6.5 \cdot 10^{10}\,\mathrm{cm}^{-3}$. The excitation times are scaled as ($\tau_{resc} = \tau_{exc} \cdot \Omega$)

with the coherent dynamics law ($\tau_{resc} = \tau_{exc} \cdot \Omega$). The Rabi frequency values are: $982 \pm 196\,\mathrm{kHz}$ (red diamonds), $745 \pm 149\,\mathrm{kHz}$ (grey triangles), $414 \pm 83\,\mathrm{kHz}$ (violet diamonds), $148 \pm 30\,\mathrm{kHz}$ (green circles) and $122 \pm 24\,\mathrm{kHz}$ (blue squares). It is clear from the Fig. 3.3 that the curves only overlap up to $\tau_{resc} \approx 0.23$ ($\tau_{exc} \approx 1\,\mu\mathrm{s}$), and from that point the curves diverge. We interpret this as a sign of the change of the slope of the dynamics, which in turn is related to the character of the evolution of the system (coherent or incoherent).

Although the crossover between coherent and incoherent dynamics has been studied in theoretically in several works [96, 85], experimentally it has not been investigated yet. Typically, the coherent evolution lasts only for a few microseconds, which implies that performing experiments in which the different types of evolution are clearly differentiated, becomes a challenging task. In our case, to estimate at which moment the slope of the dynamics changes, we study the evolution by fitting to our data an *ad hoc* function, whose slope changes at a crossover point, τ_{coh}. In the experiment we measure the Rydberg dynamics in atomic samples of different densities, prepared using

the depumping beam technique (see 2.1). As the crossover point does not depend on the density of the cloud, by performing measurements in low density samples we ensure that our observations correspond to a change in the slope of the curve related to the coherent-incoherent transition and not to a slowing down of the dynamics caused by kinetic constraints (this will be discussed in Ch. 3.2.1).

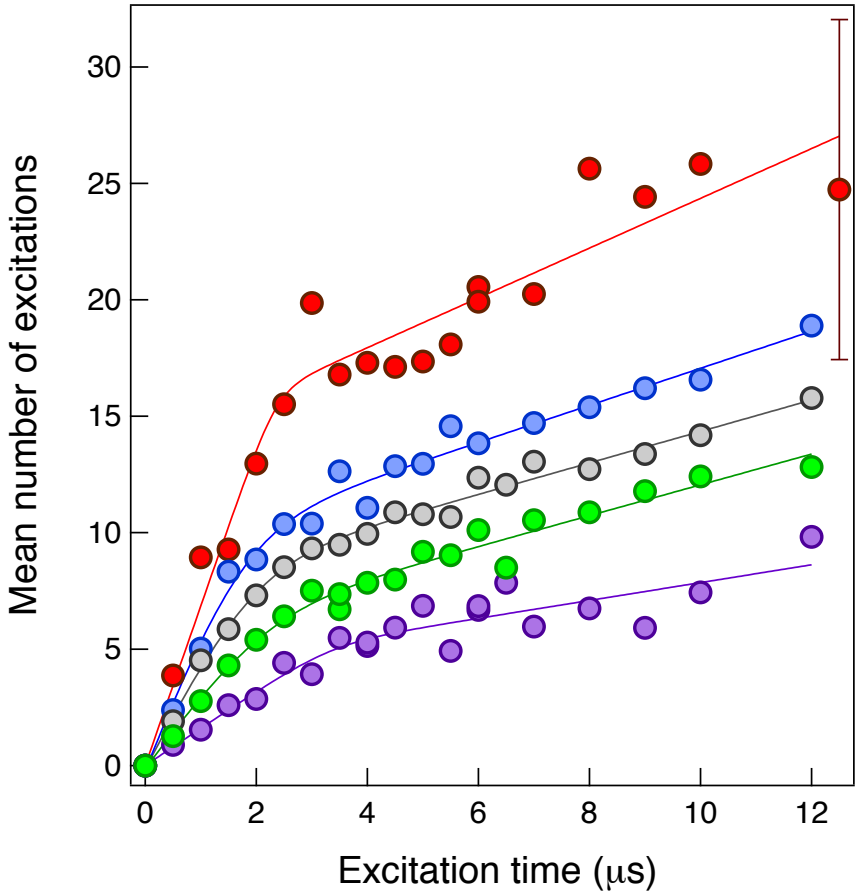

Figure 3.4: Time evolution of a Rydberg ensembles excited on resonance in which the number of atoms per superatom, $\tilde{N}$, was varied: $\tilde{N} = 342.2$ (red circles), $\tilde{N} = 111.7$ (blue circles), $\tilde{N} = 32.9$ (grey circles), $\tilde{N} = 14.9$ (green circles), $\tilde{N} = 9.7$ (violet circles). The MOT parameters were: $N = 101000$ atoms, size $V = 71.3\,\mu\text{m} \cdot 45.5\,\mu\text{m} \cdot 58.4\,\mu\text{m}$ and peak density $n_0 \approx 9.8 \cdot 10^{10} cm{-}3$. The Rabi frequency was: 741 ± 148 kHz. Each set of data was fit using an *ad hoc* function whose parameters are the slopes of regimes of the excitation dynamics, $\alpha 0$ and α_1, the coherence time of the system τ_{coh} and the interval Δt. A typical error bar that evidences the Poissoinian character of the counting distributions is also represented.

The MOT parameters here are: $N = 101000$ atoms, size $V = 71.3\,\mu\text{m} \cdot$

$45.5\,\mu\text{m} \cdot 58.4\,\mu\text{m}$, and the Rabi frequency was: $\Omega = 741 \pm 148\,\text{kHz}$. The results are shown in Fig.3.4. For each set of data we also indicate the number of atoms per superatom $\tilde{N} = 342.2$ (red circles), $\tilde{N} = 111.7$ (blue circles), $\tilde{N} = 32.9$ (grey circles), $\tilde{N} = 14.9$ (green circles), $\tilde{N} = 9.7$ (violet circles). We fit each set of data using an *ad hoc* function (continuous lines in Fig. 3.4), whose parameters are: $\alpha 0$ and α_1, corresponding to the slopes of the coherent and incoherent regime, respectively; τ_{coh}, the crossover time; and Δt, the range of variation of τ_{coh}.

$$f(t) = t \cdot \ \alpha_0 + (\alpha_1 - \alpha_0) \cdot \ \Delta t \cdot ln \left[exp \left(\frac{t - \tau_{coh}}{\Delta t} \right) + 1 \right] \tag{3.21}$$

In Fig. 3.5 we plot the data from the fits of Fig.3.4 as a function of the number of atoms per superatom, $\tilde{N}$. The error bars are also obtained from those fits. From these measurements we estimate the coherence time of our system to be around $\tau_{coh} \approx 2 \ldots 3\,\mu\text{s}$. This measurement has been done in the past [29] giving $\tau_{coh} \sim 2\,\mu\text{s}$, in good agreement with our observations.

The data corresponding to the coherent dynamics is expected to be proportional to $\sqrt{\tilde{N}}$:

$$\tilde{N} = \frac{4\pi}{3} r_b^3(n) \cdot n \tag{3.22}$$

Hence,we fit separately the coherent and incoherent dynamics sets of data, α_0 and α_1 points (red diamonds in Figs. 3.5 (a), (b), respectively) with a power function $y = A \cdot x^b$.

For the coherent case we obtain $b = 0.261 \pm 0.76$, and for the incoherent dynamics: $b = 0.212 \pm 0.56$, and both fits follow in good approximation the experimental data.

The fact that the values of α_0 and α_1 slightly change depending on the number of atoms with the superatom can be explained due to the inhomogeneities in the distribution of the both of the laser intensity along the interaction volume, which causes the atoms to oscillate with different frequencies depending on their position in the cloud. Additionally, the inhomogeneous distribution of the atomic density causes the collective dynamics to be much faster near the peak density point than in the outermost parts. Due to this, $\tilde{N}$ varies considerably across the atomic cloud, which, in the coherent dynamics case, can mask the collective oscillations preventing us from seeing them clearly. In fact, as the observable is an integration over the entire sample, it becomes hard to confirm the purely coherent or incoherent nature of the

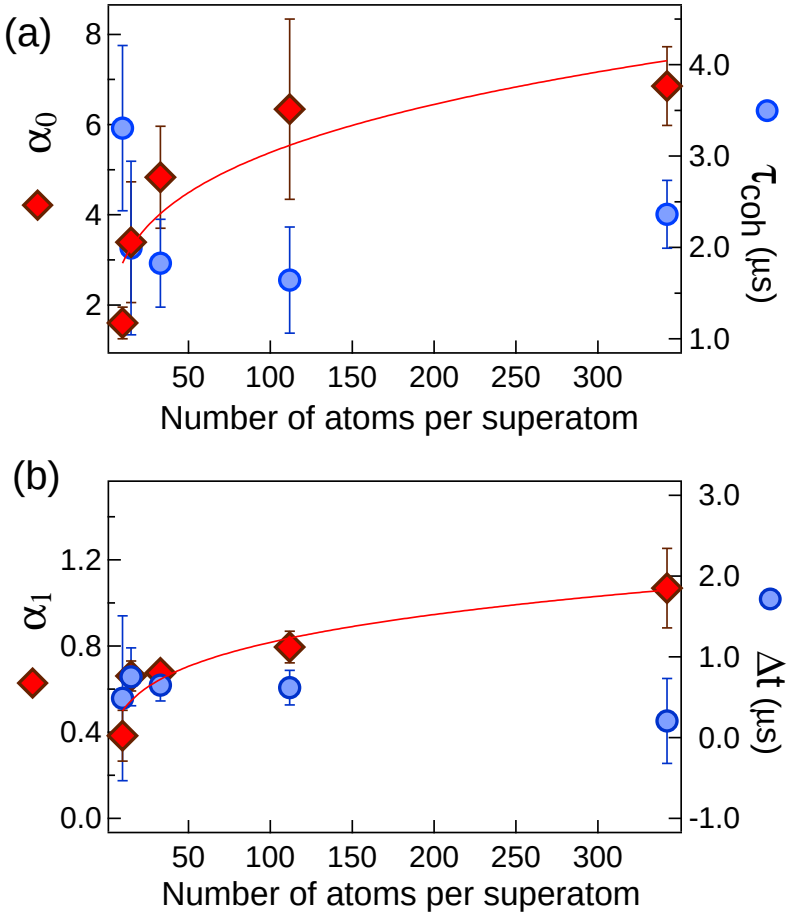

Figure 3.5: Fit parameters from Fig.3.4 data (α_0,α_1,τ_{coh}, Δt), plotted as function of number of atoms of the superatom, $\tilde{N}$. The error bars were obtained also from Fig.3.4 data. (a) α_0 points (red diamonds), corresponding to the slope of the curve in the coherent regime, were fit with a power function of exponent 0.261 ± 0.76. The coherence time of our system, τ_{coh} (blue points), shows also a dependence on $\tilde{N}$ and it has been estimated to be $2 \ldots 3\,\mu$s. (b) For the case of α_1 points (red diamonds) the exponent of the fit curve is 0.212 ± 0.56, Δt, (blue points) correspond to the range of variation of τ_{coh}.

evolution of the system [97]. Another direct consequence of this sensitivity to the density distribution is that the scaling of the data with $\sqrt{\tilde{N}}$ or $\tilde{N}$ does not always constitute a definitive proof of the character of the Rydberg dynamics. We will go back to this argument at the end of Ch. 3.2.2 where an example of this ambiguous scaling will be presented, as well as the reasons that justify such analysis at that time, and also an alternative interpretation.

3.2.1 Experimental observation of the inhomogeneous dynamics and conditioned excitation in a Rydberg ensemble

In this section we provide an experimental verification of the theoretical analysis of the incoherent evolution of a Rydberg gas developed in [30] and summarized in this Chapter. We studied the dynamics of a Rydberg system in the incoherent regime, defined according to the coherence time of our system: $\tau_{coh} = 2 \dots 3\,\mu$s. As we have already seen, the role that atomic interactions play has direct consequences on the incoherent Rydberg dynamics. So, we perform a set of experiments in which we vary the interaction parameter, R. This can be achieved by varying the density of the sample by several orders of magnitude using the depumping beam technique, consisting of depumping some of the atoms of the cloud into a hyperfine level of the ground state not coupled to the Rydberg transition, see Ch.2 for details. Also, the duration of the excitation pulses ranges from 0 to $100\,\mu$s in order to minimize the effects of the spontaneous decay from the $70S$ state, whose lifetime has been estimated to be $\tau_{lifetime} \approx 150\,\mu$s.

We generate Rydberg excitations in a quasi $1D$ system, see Ch. 2 for details, using a MOT of $N = 1.28 \cdot 10^6$ atoms and size $V = 172\,\mu\text{m} \cdot 122\,\mu\text{m} \cdot 146\,\mu\text{m}$. The laser was resonant ($\delta = 0MHz$) with the transition $|5S_{1/2}\rangle \rightarrow |70S_{1/2}\rangle$ and the Rabi frequency $\Omega = 807 \pm 160\,$kHz. The incoherent evolution of such a system was characterized by measuring the mean number of excitations as a function of time for different values of the the adimensional parameter, R. In Fig.3.6 (a) we presented the results of these measurements: red diamonds correspond to $R = 4.2$, green diamonds $R = 2.6$ and blue diamonds $R = 2$. In the case of large values of R (i.e., low interparticle distances), the dynamics grows fast, indeed, after $20\,\mu$s the saturation was clearly reached. As R becomes smaller (i.e., the interparticle distance among the atoms is bigger) the dynamics of the sample slows down and pulses of longer duration are needed in order to reach the plateau characteristic of the stationary state.

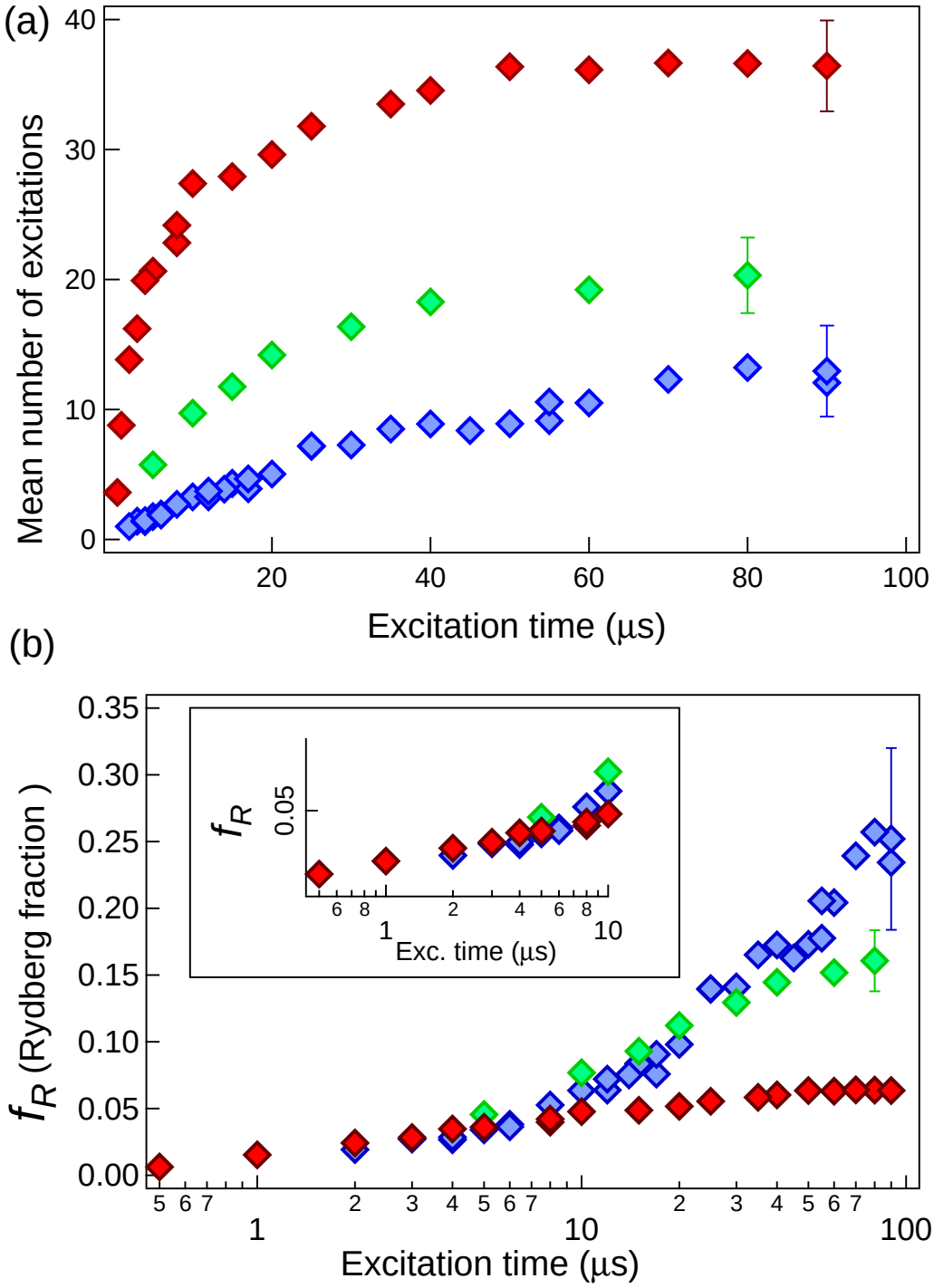

Figure 3.6: (a) Resonant Rydberg dynamics a function of the pulse duration for different values of the interaction parameter R: red diamonds correspond to $R = 4.2$, green diamonds $R = 2.6$ and blue diamonds $R = 2$. The MOT had $N = 1.28 \cdot 10^6$ atoms, size $V = 172\,\mu\text{m} \cdot 122\,\mu\text{m} \cdot 146\,\mu\text{m}$ and the Rabi frequency $\Omega = 807 \pm 160\,\text{kHz}$. The error bars correspond to the standard deviation for each set of data. (b) Rydberg fraction, f_R, as a function of the pulse duration. The error bars correspond to the measured standard deviation of the mean number of excitations.

In Fig.3.6(b) we show the Rydberg fraction, f_R, meaning the number of Rydberg excitations divided by the total number of atoms in the interaction volume, as a function of time, calculated for the same sets of data presented on the Fig.3.6(a). This analysis illustrates clearly the evolution of the system depending both on the value of R as well as on the excitation time at which the observation is done. For short excitation time values interactions do not influence the excitation process, as can be deduced from the dynamics behavior which in all cases is independent of the value of R, see the inset of Fig.3.6(b). For long excitation times the system is expected to be in the stationary state, where the value of the Rydberg fraction is $f_R \approx 1/2$. For the negligible interactions case (low R, blue diamonds) we observe a fast increase of the Rydberg fraction, reaching a maximum value of $f_R \approx 0.25$. As R increases (i.e. stronger interactions, green and red diamonds), the overall relaxation time increases too. The Rydberg fraction grows slowly with time, although the stationary state is not reached within the timescale of the experiment. As the lifetime of the $70S$ state is $\approx 150\,\mu$s, the duration of the pulse cannot be increased in order to check for the stationary state value of f_R. Moreover, for the $1D$ geometrical configuration, the emergence of a plateau before the system relaxes to the the stationary state is expected [30]. On the time scale at which the plateau should appear, the simultaneous excitation of neighboring atoms is strongly suppressed, i.e. the plateaus will appear more clearly for the highest R values. Experimentally, although the fully blockaded regime is reached (red diamonds set), we do not observe the plateau, mainly due to experimental timescale limitations, as well as the contribution from the inhomogeneous distribution of the density and Rabi frequency.

The experiments presented up to this point reproduce in good approximation the simulations of [30], showing clearly the slowing down effect on the dynamics of a Rydberg sample. An alternative analysis that can be done to bear out the kinetic constraints manifestation consists in calculating the excitation rate for different values of the mean distance between the excitations, a_{Rydb}. Intuitively, we expect that when Rydberg excitations are far from each other, the excitation rate does not depend on the density of the sample, but for interparticle distances smaller than the blockade radius, the excitation rate should decrease. This effect is expected to be more evident for the highest density cases, confirming the slowing down of the dynamics in the vicinity of the existing Rydberg excitations.

In Fig.3.7 we show the excitation rates, Γ_k, as a function of the mean interparticle distance calculated for the data sets of Fig.3.6: $R = 4.2$ red diamonds, $R = 2.6$ green diamonds and $R = 2$ blue diamonds.The continuous lines, red, green and blue, respectively; are guides to the eye.

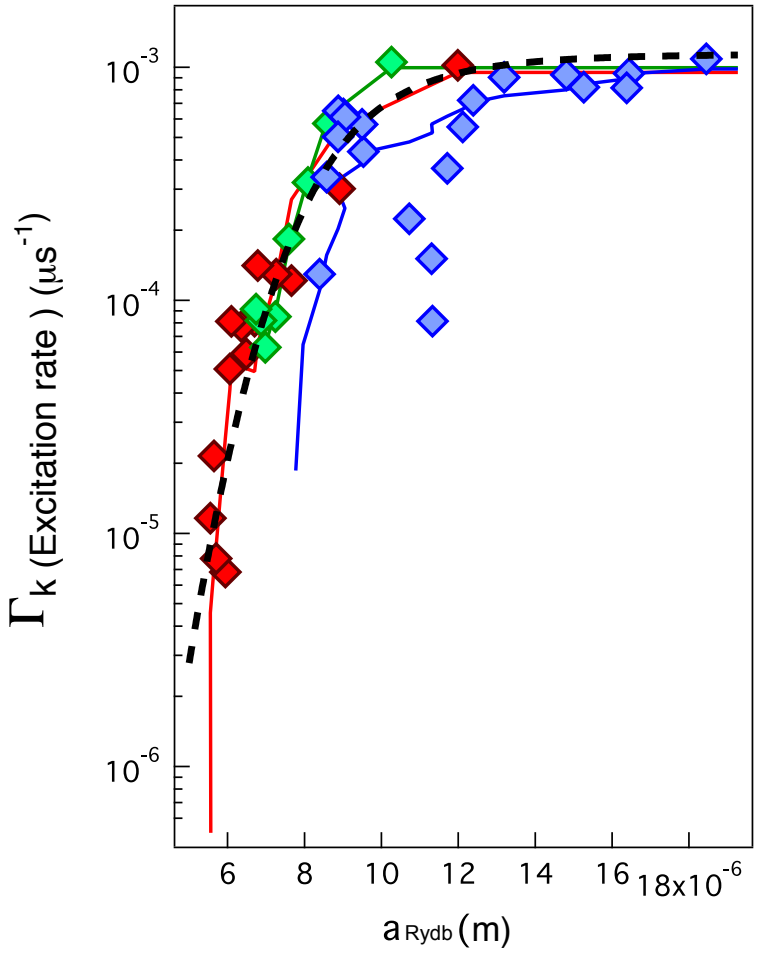

Figure 3.7: Excitation rate, Γ_k, as a function of the mean distance between the excitations, a_{Rydb} corresponding to the experimental data of Fig.3.6: $R = 4.2$ red diamonds, $R = 2.6$ green diamonds and $R = 2$ blue diamonds. The continuous lines (red, green and blue, respectively) are guides to the eye. The black dashed line corresponds to the analytic solution of Eq. 3.16 for the highest density conditions ($n_0 = 7.8 \cdot 10^{10}\,\mathrm{cm}^{-3}$).

To do these calculations, we considered an interaction volume of radial size $\sigma_{Blue} = 6\,\mu$m and length $\sigma_{IR} = 110\,\mu$m. The number of atoms within this volume was obtained from Eq. 2.5 (see 2 for the complete mathematical description):

$$N_{int} = N \cdot \mathrm{erf}\left(\frac{\sqrt{2}\sigma_{Blue}}{\sigma_y}\right) \cdot \mathrm{erf}\left(\frac{\sqrt{2}\sigma_{Blue}}{\sigma_z}\right) \cdot \mathrm{erf}\left(\frac{2\sigma_{IR}}{\sigma_x}\right)$$

giving: $N_{int} \approx 5197$ atoms within the interaction volume. This number was used to calculate the fraction of Rydberg atoms excited inside the interaction volume for a certain duration of the Rydberg pulse:

$$f_R =< N_{obs} > \cdot \frac{\eta}{(N_{int})_{eff}} \tag{3.23}$$

where $\eta \approx 0.4$ is the detection efficiency of our system and $(N_{int})_{eff}$ is the effective number of atoms remaining inside the interaction volume after the application of the depumping beam pulse. By differentiating each set of data we obtained the experimental excitation rates for the three cases. The mean distance between excitations a_{Rydb}, was calculated as:

$$a_{Rydb} = (n_R)^{-1/3} \tag{3.24}$$

where n_R is the density of Rydberg excitations inside the interaction volume.

For large values of a_{Rydb}, the three curves exhibit similar values of the excitation rate, indicating that new excitations are generated in the system independently of the interactions that are already present. For $a_{Rydb} < r_b \approx 10\,\mu$m the excitation rate decreases. This decrease is more pronounced for smaller mean distances, which lead to larger interactions (green and red curves). This evidences the slowing down of the dynamics in the vicinity of the excitations caused by the interactions as well as the low (but non-zero) probability of generating new excitations even at distances smaller than the blockade radius, that can be observed if the timescale of the experiment is long enough. The red, green and blue continuous lines are smoothing fits to the data, acting as guides for the eye.

We compare the experimental data to the theoretical calculation of the excitation rate, represented in Fig. 3.7 by the black dashed line. From Eq.3.4 and assuming $\Omega^2 >> \gamma_{\parallel}$, we obtain the expression for the excitation rate in the incoherent regime:

$$\Gamma \sim \frac{\Omega^2}{\gamma_\perp} \cdot \frac{1}{1 + \left(\frac{C_6 \cdot n_j}{|r_j - r_k|^6} \cdot \gamma_\perp\right)^2} \tag{3.25}$$

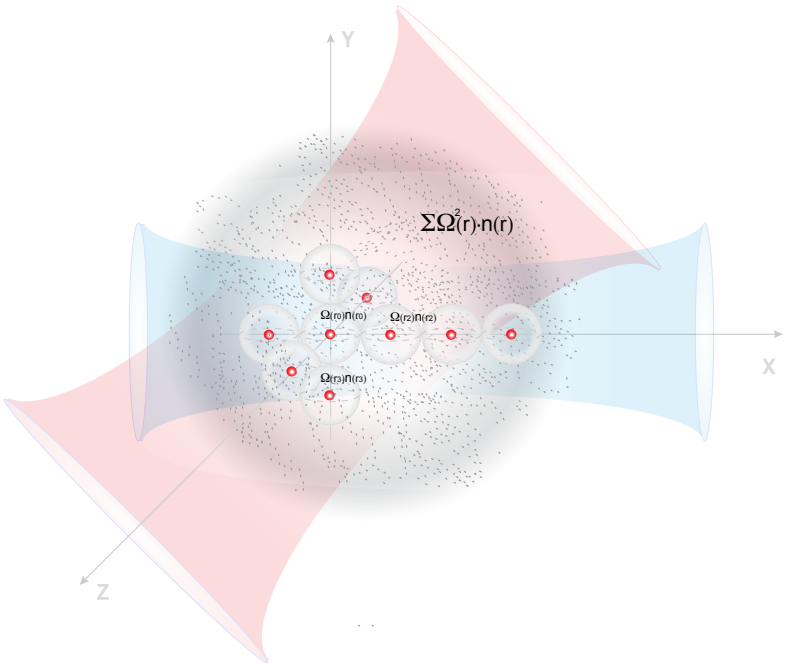

Figure 3.8: Illustration on the approximation method we use to take into account for the inhomogeneous distribution of the Rabi frequency and the density within the interaction volume. The collective Rabi frequency is estimated by summing the contributions (the local values of the Rabi frequency and the density) over the interaction volume.

Some of the parameters included in Eq. 3.25, like the Rabi frequency or the interparticle distance, are corrected here by a factor that accounts for the uncertainties these values present. We take into account that the experiment is performed in a $1D$ configuration, allowing us to consider that, on average, each excitation has $n_j = 2$ nearest neighbors. Regarding to the interparticle distance, we assume that the most probable position where a new excitation could be generated would be halfway between two already existing excitations: $a_{Rydb} = \frac{r_j - r_k}{2}$. Additionally, an extra factor $\alpha = 3$ is applied to a_{Rydb} to account for the uncertainties when measuring the size of the interaction volume, so: $\tilde{a}_{Rydb} = 3 \cdot \frac{a_{Rydb}}{2}$.

With respect to the Rabi frequency, we consider its inhomogeneous distribution along the sample (for the definition of gaussian distribution we use the one given in [98]):

$$\Omega(x, y, z) = \Omega_0 \cdot \exp\left(\frac{-x^2}{\sigma_{IR}^2}\right) \cdot \exp\left(\frac{-y^2}{\sigma_{Blue}^2}\right) \cdot \exp\left(\frac{-z^2}{\sigma_{Blue}^2}\right) \tag{3.26}$$

where $\Omega_0 = 1123 \pm 224.6\,\text{kHz}$ is the peak Rabi frequency in this experiment. The atomic density is also inhomogeneusly distributed along the sample:

$$n(x,y,z) = n_0 \cdot \exp\left(\frac{-x^2}{\sigma_{IR}^2}\right) \cdot \exp\left(\frac{-y^2}{\sigma_{Blue}^2}\right) \cdot \exp\left(\frac{-z^2}{\sigma_{Blue}^2}\right) \tag{3.27}$$

Then, the effective "mean" Rabi frequency can be calculated by summing the contributions of the local Rabi frequencies and densities over the interaction volume, see Fig. 3.8):

$$\Omega_{coll} = n(x,y,z) \cdot \Omega(x,y,z) \tag{3.28}$$

Finally, the excitation rate has to be normalized by the total number of atoms within the interaction volume, N_{int}:

$$\Gamma \sim \frac{\tilde{\Omega}_{coll}^2}{\gamma_\perp} \cdot \frac{1}{1 + \left(\frac{2 \cdot C_6}{\tilde{a}^6} \cdot \gamma_\perp\right)^2} \cdot \left(\frac{1}{N_{int}}\right) \tag{3.29}$$

Doing this approximation, we obtain an excitation rate which is a factor of ~ 10 lower than the experimental data. This may be due to the systematic errors when measuring the number of atoms with the CCD camera, which carries a systematic error of a factor of ~ 2; and also to errors in the estimation of the size of the interaction volume.

In Fig. 3.7, we show the theoretical curve represented as a black dashed line (it was adjusted by a factor ~ 10 in the vertical axis for an easier comparison with the experimental data). It reproduces in good approximation the experimental behavior, exhibiting as well the change of the slope of the curve around the blockade radius value for the $70S_{1/2}$ state: $\sim 10\,\mu$m. These results agree as well with the model of [30], providing a valid description of the incoherent dynamics of Rydberg excitations.

3.2.2 Rydberg tomography of an ultracold atomic cloud

At this point we have already proved the importance of know and control the density of the sample in Rydberg experiments, because the visualization of some interesting phenomena that emerge in these systems, like the manifestation of the kinetic constraints, are strongly dependent on this parameter. The depumping beam technique allowed us to vary the effective density of

the sample, i.e. the number of ground state atoms liable to be excited to the Rydberg state. However this is not the only way in which the density-related effects on Rydberg dynamics can be studied. In the studies of the current section we present a method that allows to change the atomic density within the interaction volume by moving the excitation beam across the sample in one spatial direction, i.e. doing a tomography of the cloud. We use this technique to study as well one of the most characteristic feature of Rydberg systems, the dipole blockade effect [24].

The dipole blockade regime was studied in different conditions: from experiments in which only two individual atoms were used [13, 14], to disordered clouds of cold atoms [25, 26, 99, 82, 84, 80, 100, 101], or Bose-Einstein condensates [80, 102]. Besides the creation of entanglement in the strongly blockaded regime was recently proved [48, 49]. Hence, using the above-described method we are able to spatially visualize the blockade phenomenon in an inhomogeneous gas of ultra-cold rubidium atoms.

In our experiment we create small clouds of ultra-cold 87-Rb atoms in a magneto-optical trap (MOT) whose parameters (loading flux from a primary two-dimensional MOT, magnetic field gradient, and size of the MOT beams) are chosen such as to obtain clouds with a Gaussian density profile: [1]

$$n(x,y,z) = \frac{N}{\sigma_x\sigma_y\sigma_z(\pi/2)^{3/2}} e^{-(\frac{x^2}{\sigma_x^2}+\frac{y^2}{\sigma_y^2}+\frac{z^2}{\sigma_z^2})} \tag{3.30}$$

Those clouds are scanned by moving the excitation beam along the x-direction (see Eq.(3.30)). In our experiments, MOTs have typical widths $\sigma_{x,y,z} \approx 21\,\mu$m and contain up to $N \sim 10^5$ atoms. The resulting peak density is $n \approx 2.5 \times 10^{10}\,\mathrm{cm}^{-3}$, which corresponds to a mean inter-particle spacing of around $3.5\,\mu$m.

We realize a scan of the position of one of the excitation lasers across the cold cloud, determine the number of Rydberg excitations detected as a function of the position and compare this distribution to the one obtained for the number of ions created by a two-photon ionization process via the intermediate $5P$ level. To get a good estimate of the mean number of ions and the variance, the experimental sequence is repeated 50 times for each set of parameters. In order to reveal the effect of the blockade on the Rydberg excitation, we probe different density regions by scanning the position of the $1D$ configuration laser beam at 421 nm vertically through the density profile of the MOT (see Fig.(3.9)) using a mirror equipped with a piezo-driven motorized actuator that allows us to control the position of the laser

[1] These results are published in [34], where a different definition of the Gaussian density profile of the cloud was used.

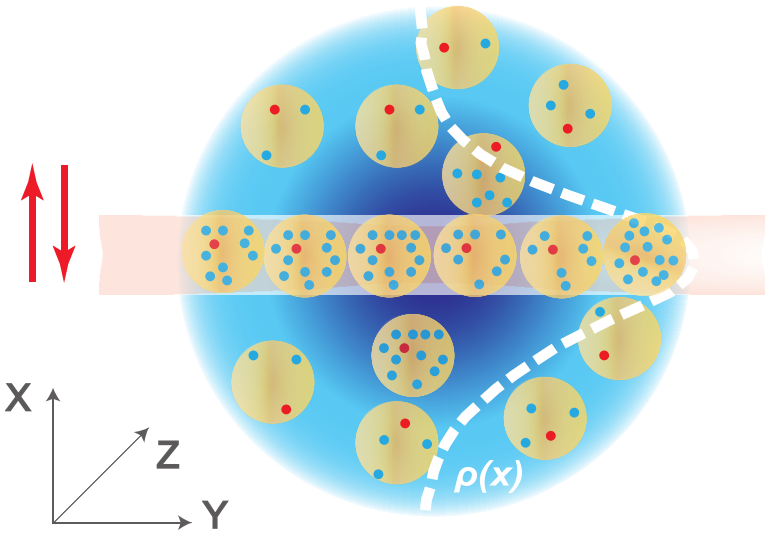

Figure 3.9: Experimental procedure for the Rydberg tomography of a cold atomic cloud. The vertical position of the 421 nm excitation laser was vertically scanned across the density profile of the atomic cloud represented here by $n(x) = n(x, y = 0, z = 0)$, i.e., the peak density at position x). The larger excitation beam at 1013 nm is not shown in the Figure.

beam in steps of 0.7 μm. A similar technique was demonstrated recently in [103]. Since the MOT has a roughly Gaussian shape in all three spatial directions and the size of the 421 nm laser beam is much smaller than the MOT size ($\sigma_{Blue} \sim 6\,\mu$m), we assume that the atomic density was roughly constant over the radial extent of that beam and had a Gaussian shape along its direction of propagation. Consequently, a variation of the position of the laser beam results in a variation of the mean atomic density inside the excitation volume defined by the beam width, while the effective length of the sample along the propagation direction of the beam remains constant.

In the experiment of direct ionization from the $5P_{3/2}$ state, we expect that the number of ions detected by the channeltron is directly proportional to the density profile of the MOT in the vertical direction. This is confirmed by the comparison between the ion signal as a function of position and the integrated density profile of the MOT obtained with a CCD camera, as it is shown in Fig.3.10(a). Repeating the scanning experiment with a two-step Rydberg excitation, we again obtain a roughly Gaussian dependence of the mean detected ion number (and hence the mean number of excitations) on the beam position, but this time the measured width of the distribution is noticeably larger.

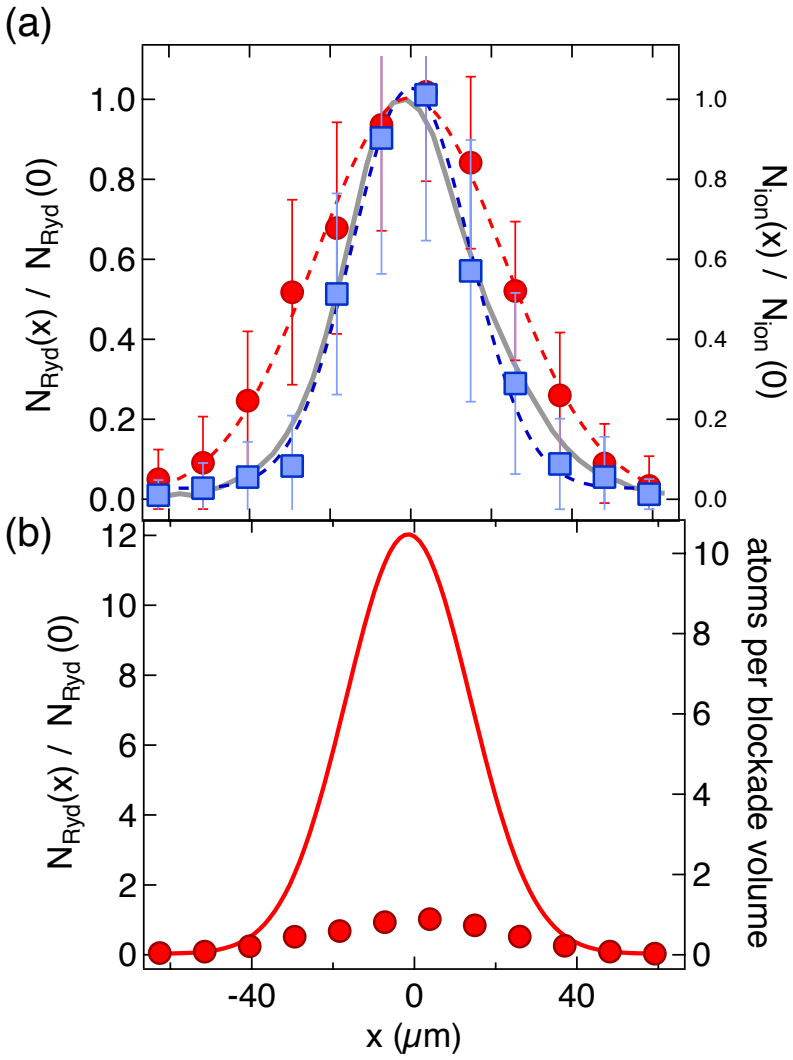

Figure 3.10: Spatial tomography of a MOT using Rydberg excitations to the $71D_{5/2}$ state. In (a), the normalized number of detected ions is plotted for the direct ionization from the $5P_{3/2}$ state using only the 421 nm beam (blue squares) and for the Rydberg excitation (red circles). The duration of the excitation pulse is $\tau = 1\,\mu$s for direct ionization process, in which $N_{Ions}(0) \approx 8$, and for the Rydberg excitation it is $\tau = 3\,\mu$s with $N_{Ryd}(0) \approx 12$. The error bars correspond to one standard deviation of each set of data. For comparison, the density profile of the MOT (integrated along the y and z-directions) is also shown (grey line). Dashed lines are Gaussian fits to the data. In (b), the normalized ion number for the Rydberg excitation plotted in (a) (without the error bars) is shown together with a Gaussian fit to the wings of that distribution with a fixed width equal to that of the MOT (solid line, left-hand side scale). The solid line also represents the spatial variation of the calculated number of atoms per blockade volume (right-hand side scale), obtained by multiplying $n(x, y = 0, z = 0)$ by the blockade volume obtained from the blockade radius of 10 μm.

This can be explained in terms of the Rydberg blockade: In the high-density region close to the centre of the atomic density distribution, the interactions between the Rydberg states leads to a suppression of the number of excited atoms compared to the non-interacting case, resulting in a flattening - and, therefore, broadening - of the distribution. It is important to note here that for the purposes of this work, we characterize the system by a single (peak) density at position x, $n(x) = n(x, y = 0, z = 0)$, neglecting the variation in the other directions, particularly along y. Whereas this approach does not capture the detailed dynamics of the system, it still leads to reasonable agreement with the expected variations and scalings.

Another way of visualizing the blockade effect consists in fitting a Gaussian curve to the wings of the spatial distribution, because there one can assume that interaction effects are negligible and hence the measured Rydberg number is roughly linearly proportional to the local density, as shown in Fig.3.9. Fixing the width of the Gaussian to that of the atomic density distribution but leaving the amplitude as a fitting parameter, we obtain the solid curve in Fig.3.10 (b). That curve shows the number of Rydberg excitations expected to be found in the absence of the Rydberg blockade effect based on the numbers observed in the low-density wings of the atomic cloud. At the centre of the distribution, the detected number of Rydberg atoms is suppressed by a factor of ~ 12 compared to the expected number. Fig.3.10(b) also shows the number of atoms per blockade sphere as a function of position, calculated assuming a blockade radius of around $10\,\mu$m expected for the $71D_{5/2}$ state [102] used in this experiment. While in the wings of the distribution ($50 - 60\,\mu$m from the center) that number is less than ≈ 0.1, justifying the above assumption of negligible interactions; towards the centre of the MOT it rises to around 10, in good agreement with the suppression by a factor 12 of the number of Rydberg excitations calculated above.

The suppression of excitations due to the Rydberg blockade was also clearly visible in a plot of the ion and Rydberg measurements as a function of the local density in the MOT, as seen in Fig.3.11 (a). Whereas the number of ions grows linearly with the density, the dependence of the number of Rydberg atoms on the density exhibits a decreasing slope as the density increases and is fitted with a power law with an exponent of around 0.43. A simple explanation for this dependence is that the collective Rabi frequency depends on the square root of the density (see below) and the number of excitations (for fixed time) depends roughly linearly on the collective Rabi frequency (as long as the saturated regime is not reached). This leads to an expected power-law dependence of the number of excitations on density with an exponent of around 0.5, close to the observed value.

Further evidence for the blockade effect was obtained by measuring the

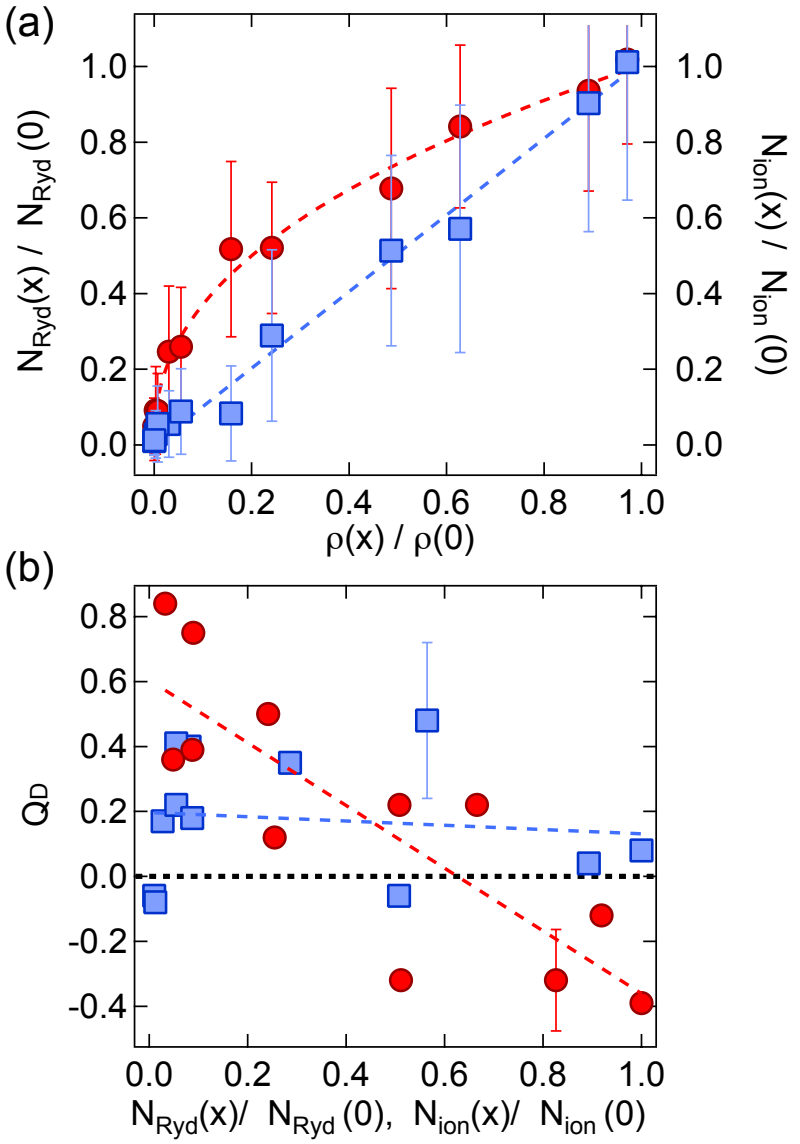

Figure 3.11: Characterization of the Rydberg excitations to the $71D_{5/2}$ state as a function of the MOT local density and statistics of the detected ions. In (a), the data of Fig.3.10(a) is plotted as a function of the normalized local density in the MOT. The Rydberg excitation (red circles) data are fitted with a power law with exponent 0.43 ± 0.02 whereas a linear function is used to fit the data corresponding to direct ionization (blue squares). In (b), the Mandel Q-factor of the detected ion signal for both experiments is shown as a function of the normalized number of detected ions. Typical error bars (one standard deviation) for the blue and red symbols are shown. Dashed lines are linear fits to guide the eye.

fluctuations in the number of detected ions.

In Fig.3.11 (b) the detected Q-factor, Q_D, is plotted as a function of the detected ion signal. For the case of Rydberg excitations (red circles) Q_D depends linearly on the mean number of excitations. The negative values of Q_D, reached at high values of the number of detected ions, constitute a clear indication of sub-Poissonian statistics due to the Rydberg blockade which lead to strong (anti-) correlation of the excitation probabilities. In the direct ionization experiment (blue squares), Q_D was approximately independent of the mean number and fluctuates between 0 and 0.4 which, given the limited sample size of 50, was compatible with a Poissonian process for which in practice we expect $Q_D \geq 0$ (since technical noise would result in a positive value of Q_D).

Additionally, we study the time evolution of the detected number of Rydberg atoms at three different positions of the 421 nm beam (i.e., in three different local densities $n(x)$): at the center of the cloud, at $n(x) \approx 1.0\sigma_x$ and at $n(x) \approx 1.4\sigma_x$ from the center, respectively. Fig.3.12 (a) shows the results obtained for each position of the beam.

Depending on the size of the sample, the blockade can be total (single excitation allowed) or limited [24]. As it was explained before, the excitation of a single Rydberg atom prevents, via the blockade mechanism, the excitation of other ground-state atoms within the radius r_b of the blockade sphere, as it is shown in Fig. 3.9.

At the time at which these experiments were performed we used the "superatom" picture in order to interpret our results. According to this picture, the timescale for the excitation dynamics should scale with $\sqrt{\tilde{N}}$ in case of coherent dynamics, where $\tilde{N}$ needs to be determined experimentally. For this reason, we rescaled the excitation time values of Fig. 3.12 (a) by a factor $\sqrt{n(x)/n(0)}$. In Fig. 3.12 (b) we show how the three curves fall on top of each other, indicating the expected dependence on $\sqrt{\tilde{N}}$ of the Rabi frequency. Since the publication of our paper we have gained more insight into the system, appreciating the fundamental difference between the coherent and incoherent excitation regime (see Ch. 3.2), and now conclude that the $\sqrt{\tilde{N}}$ scaling is valid only for the coherent part of the dynamics (the first $2 \ldots 3\,\mu$s), while the above experiment was conducted mainly in the incoherent regime (where the scaling is expected to be proportional proportional to $\tilde{N}$). The apparent agreement with the coherent scaling law is a result of the uncertainties of the experiment, mainly regarding to the estimation of the local density and to the fact that both the density and the Rabi frequency are inhomogeneously distributed along the interaction volume. All these factors contribute to the evolution of the system in different degrees, leading in the end to a dynamics curve similar to the one expected for the collective

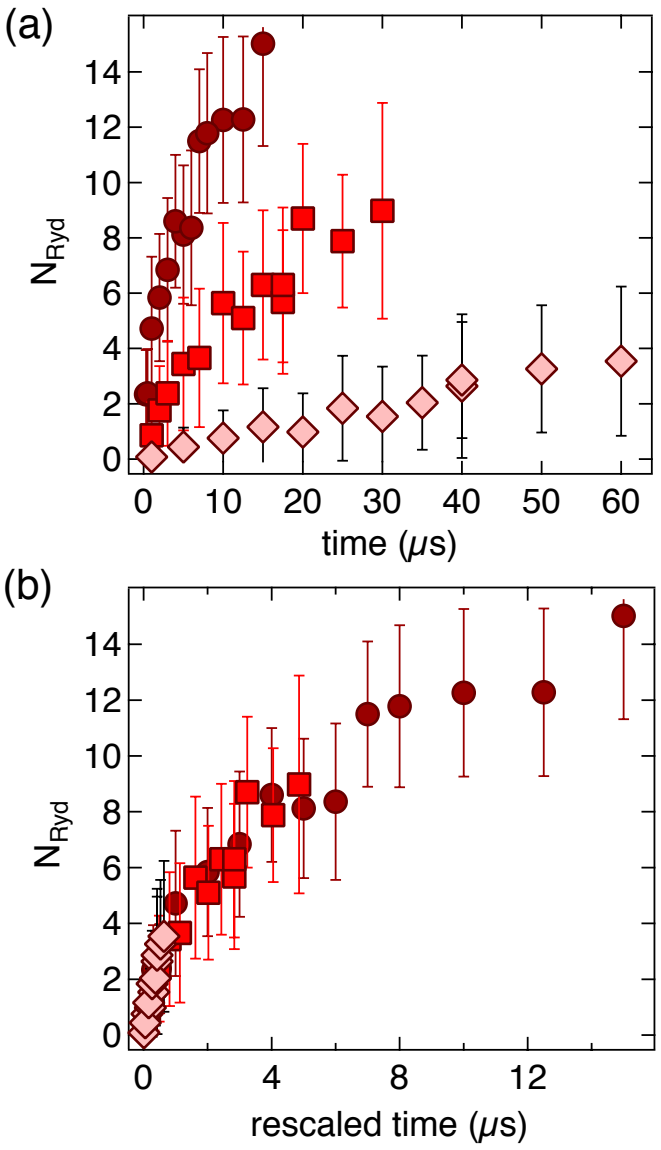

Figure 3.12: Excitation dynamics in the $88D_{5/2}$ Rydberg state for different beam positions: at the center of the MOT (dark red circles) and at distances of $n(x) \approx 1.5\,\sigma_x$ and $n(x) \approx 2\,\sigma_x$ from the MOT center (medium red squares and light red diamonds, respectively). Fig.3.12 (a) shows the mean number of detected Rydberg atoms as a function of time. In Fig.3.12 (b) the same data is plotted as a function of a renormalized time that takes into account the different collective Rabi frequencies due to the different local densities. The error bars correspond to one standard deviation of each set of data.

behavior but that in reality is a mixture between coherent and incoherent dynamics. In fact, by scaling the data with the incoherent dynamics law ($\sim \tilde{N}$) we also obtained a reasonable overlap between the curves, which indicates that more accurate experiments and models are necessary in order to clearly distinguish between the coherent and incoherent regimes.

3.3 Summary and perspectives

In this Chapter we presented an experimental study on the resonant Rydberg excitation dynamics in the incoherent and non-dissipative regime. Under these conditions we studied the effect of the strong interactions between Rydberg atoms, both in the saturated regime through an experiment which illustrates how the dipole blockade works, as well as in the non-saturated regime, where we observed that in these systems some regions exhibit faster dynamics than others, and a hierarchical excitation process whereby each new Rydberg excitation conditions the successive ones. We also present a series of experiments in which we find evidence of a crossover between coherent and incoherent dynamics. This distinction turned out to be not always clear, mainly due to the inhomogeneous distribution of the densities and the Rabi frequency along the sample. Indeed, we tried to verify the universal scaling laws predicted for the dynamics of a Rydberg ensemble in the different regimes [80] with the Rabi frequency and the number of atoms within the superatom, $\tilde{N}$, obtaining different results. Regarding the scaling with Ω, we got a good agreement when scaling the excitation time values with $\sim \Omega^2$ (suggesting that the dynamics of our system is mainly incoherent), whereas when the same data were rescaled with $\sim \Omega$ (the expected law in the coherent regime), the curves diverge from each other. By contrast, when when we applied the same reasoning to the scaling with the number of atoms inside the superatom, $\tilde{N}$, we did not got the same degree of agreement as in the Rabi frequency case. We observed different slopes on the dynamics curve for the two regimes, as well as signatures of the crossover between them. From those experiments we estimated the coherence time of our system to be: $\tau_{coh} \approx 2 \ldots 3\,\mu$s. This value of τ_{coh} is quite sensitive to the number of atoms of the superatom, which could be explained due to the inhomogeneous distribution along the sample both of the laser intensity as well as of the atomic density, leading to a global evolution which is a sum of all the different local contributions. This high sensitivity to the density effects, already noticed in [80], means that the scaling laws with $\tilde{N}$ become ambiguous in some cases, making it necessary to look for other indicators of the coherent or incoherent nature of the system. Although some steps in this direction have been taken both in the coherent dynamics case [104, 105], as well as on the incoherent

regime [106, 107], the lack of a solid explanation of the behavior of the dynamics of those systems suggest that further theoretical investigations, with realistic experimental conditions taken into account, need to be carried out.

Chapter 4

Generation of Rydberg aggregates under non-dissipative conditions

Strong interactions in Rydberg system have been studied almost exclusively in resonantly excited Rydberg ensembles, where they manifest themselves either as spatial correlations [22, 21] or through a reduction of fluctuations [29]. However, the emergence of those interactions is not limited to that regime. For instance, the effect of those interactions is observable in the evolution of the Rydberg dynamics off-resonance, where they enhance the generation of new excitations[108, 109, 35, 110], in contrasts to the blockade and dynamical constraint that happens on resonance.Furthermore, for off-resonant excitation of strongly interacting Rydberg systems in a dissipative regime, one expects to create highly correlated many-body states exhibiting, among other characteristics, intermittency and multi-modal counting distributions [57, 54, 55, 56].

The dynamics presents some peculiarities not fully understood yet. In this chapter we present a systematic study of the off-resonant dynamics of a Rydberg system, performed to provide a more complete description of the aforeseaid processes. Thus, in the non-dissipative regime we study how the excitation process evolves making use of a technique described in Ch. 2, which allows us to focus properly in the regime of our interest. The information contained in the histograms of the full counting distributions of those experiments serves to establish the main differences either between the resonant and the off-resonant excitation processes, but also among the different stages of the off-resonant dynamics.

4.1 Off-resonant excitation of Rydberg atoms

Figure 4.1(b-d) illustrates the different excitation regimes. Away from resonance (Fig.4.1(d)), the excitation of Rydberg atoms can happen mainly in two ways. One possibility is that two atoms at a distance r from each other could be simultaneously excited via a resonant two-photon excitation process if:

$$C_6/r^6 = 2\hbar\Delta \tag{4.1}$$

where $C_6 = \hbar \times 1.2\,\mathrm{THz}\,\mu\mathrm{m}^6$, is the van-der-Waals coefficient for the $70S_{1/2}$ Rydberg state.

Here, a typical detuning of $+10\,\mathrm{MHz}$, corresponds to a resonant distance $r = 6 \pm 0.1\,\mu\mathrm{m}$ (where the range in r is due to the finite laser linewidth of about $0.7\,\mathrm{MHz}$). As already mentioned, in order to verify the above condition, the detuning values and the van der Waals interaction strength must present the same sign.

Alternatively, an initial off-resonant Rydberg excitation could be generated and be followed by the resonant excitation of a nearby ground state atoms located at the appropiated distance (where the energy shift due to the interactions is compensated by the laser energy):

$$C_6/r^6 = \hbar\Delta \tag{4.2}$$

This resonant condition is the opposite of the blockade effect (Fig.4.1(c)), where the interaction *suppresses* the excitation process, allowing at most one single (collective) excitation within a blockade radius.

The timescale for generating off-resonant excitations through the two-photon process can be estimated from the two-photon Rabi frequency expected for the pair excitation of two Rydberg atoms with an intermediate singly-excited state detuned by Δ from resonance:

$$\Omega_{off} = \Omega^2/(2\delta) \tag{4.3}$$

Thus, for our typical Rabi frequency values ($\Omega \approx 2\pi \times 200\,\mathrm{kHz}$) and a detuning of $\delta/2\pi = +2\,\mathrm{MHz}$, the expected time needed for generating off-resonant excitations is: $\tau_{off} \approx 100\,\mu\mathrm{s}$; where $\Omega_{off} \approx 2\pi \times 10\,\mathrm{kHz}$, much smaller than the collective Rabi frequency $\Omega_{coll} \approx 2\pi \times 1.4\,\mathrm{MHz}$ (for a number $N_{db} \approx 50$ of atoms inside a blockade volume , [24, 81]). The generation

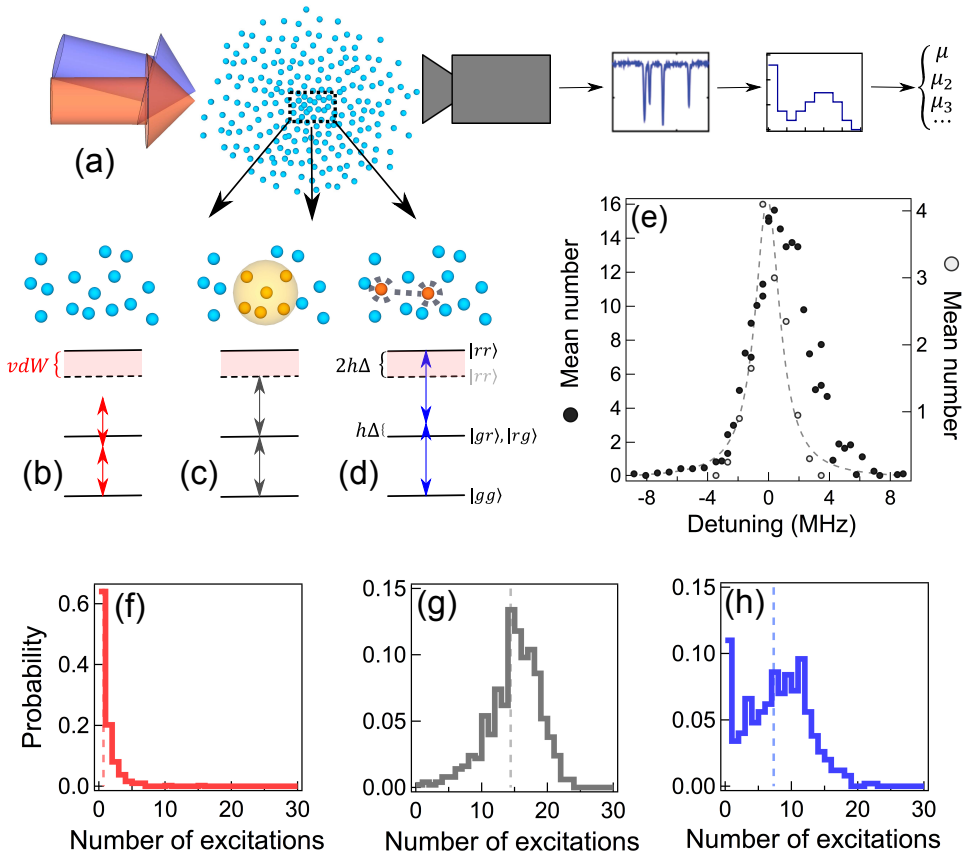

Figure 4.1: (a) Schematic representation of the experimental procedure. The histograms and full counting statistics (i.e., the moments of the counting distribution) are calculated from the individual counts of the detected Rydberg excitatons.(b-d) Resonant and off-resonant excitation two-photon processes for interacting Rydberg atoms. For resonant excitation (c) the van-der-Waals interaction between the atoms shifted a second excitation out of resonance, leading to the dipole blockade effect and the generation of the blockade spheres. Off resonance, interactions between pairs could either lead to resonant excitation (d) or to strong suppression of excitations (b). In (e) a plot of the mean number of Rydberg excitations as a function of detuning revealed the interaction-induced resonances for positive detuning, which showed up as an asymmetry of the lineshape. The excitation durations were $1\,\mu$s (grey symbols, right vertical axis) and $20\,\mu$s (black symbols, left vertical axis). (f-h) Histograms of the counting distributions $P(x)$ as a function of the excitation number x in the resonant and off-resonant regimes. For positive detuning $\delta/2\pi = +3.5\,$MHz (h) the histogram exhibited a bimodal structure, whereas on resonance (g) it presented a single peak. For negative detuning $\delta/2\pi = -3.5\,$MHz (f) the mean number of excitations was considerably smaller than in (h). The dashed vertical lines indicated the mean number of excitations. The Rabi frequency was $2\pi \times 400\,$kHz, the interaction volume $10^{-7}\,\mathrm{cm}^3$ and the density $1.8 \times 10^{11}\,\mathrm{cm}^{-3}$.

of subsequent excitations from an already excited atom can occur faster: $\tau_{off} \approx 50\,\mu$s.

By contrast, for a detuning with opposite sign to that of the van-der-Waals interaction, neither single-particle nor pair excitations are resonant, leading to an overall suppression of the excitation probability (Fig.4.1(b)).

Clear signatures of those interactions can be found already in the excitation spectra, as is shown in Figure 4.1(e), where the mean number of Rydberg excitations as a function of detuning is plotted for two different excitation durations. For the $1\,\mu$s pulse (white dots), off-resonant excitations are negligible , leading to a symmetric lineshape. For a $20\,\mu$s pulse (black dots), however, the excitation time is an appreciable fraction of $\tau_{off} \approx 100\,\mu$s, and off-resonant excitations become visible resulting in a lineshape that is clearly asymmetric with respect to zero detuning.

Further evidence for the different excitation regimes is found in the histograms of the counting distributions (Fig. 4.1(f)-(h)). In order to obtain the full counting distribution of the Rydberg excitations we perform 500 repetitions of the experiment. As seen in Fig 4.1(f)-(h), on resonance the distribution is roughly Poissonian (it becomes sub-Poissonian in the fully blockaded regime, as seen in Fig. 4.1(b)). By contrast, for positive detuning the distribution becomes multi-modal with a dominant feature close to zero excitations and another one centered around a mean value of 12. For the negative detuning, the histogram confirms the expected strong suppression of excitations.

The main features of this experiment are reproduced by a numerical simulation (Fig.4.2 (a)-(d)) developed in collaboration with the group of P. Pillet (Laboratoire Aimé Cotton, Orsay, France).based on an extension of the Dicke model applied to Rydberg excitations (see the basic foundations in Ch.1.4). Some other recent works like,[95] also adapted the Dicke model to describe the excitation of Rydberg atoms.

The collective Dicke states contain the full statistical information about the collective Rydberg excitation and therefore allow the calculation of all the moments of the excitation statistics. The improved Dicke model, used here as a support for the correct understanding of our experimental results, takes into account the time-dependent coupling between the Dicke states, which become increasingly important as the number of Rydberg excitations increased.

We do not expect the model to reproduce the experimental results in a perfect way, as several details of the experiment (inhomogeneous density of the cloud, other Rydberg levels, decay from the excited state, finite velocity of the atoms) are not taken into account. Nevertheless, Fig. 4.2 shows that for a reasonable choice of parameters in the simulation, which are similar

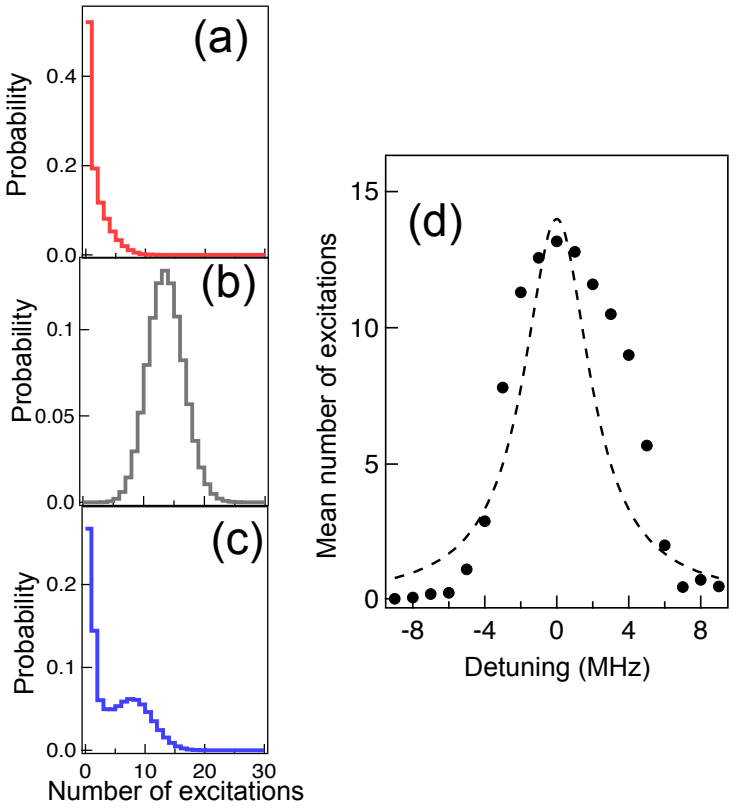

Figure 4.2: (a-c) Numerical simulations of the counting distributions for $\Delta/2\pi = -5, 0, 5$ MHz, respectively. The finite detection efficiency in the experiment is taken into account through a convolution with a binomial function. In (d) the Rydberg mean values obtained from that simulation are plotted as a function of detuning. Comparison with a Lorentzian fit (dashed line) centered at zero detuning highlights the asymmetry of the lineshape. The parameters used for the simulation are: Rabi frequency 130 kHz, excitation duration 4 μs, density $9 \times 10^{10}\,\mathrm{cm}^{-3}$ and interaction volume $8.9 \times 10^{-8}\,\mathrm{cm}^3$.

to the experimental ones, the results agree quite well with the measured data. In particular, the agreement at the level of the full counting statistics (histograms in Fig. 4.2 (a)-(c)) is satisfactory. For positive detuning the histogram exhibits a bimodal structure, while a single peak is essentially observed on resonance and very few atoms are excited for negative detuning.

4.2 Off-resonant Rydberg dynamics in the non-dissipative regime

The results obtained in previous section evidence strong qualitative differences in the excitaton of Rydberg atoms on and off resonance. Those studies were performed at fixed time values, however, it is possible to obtain more information about the correlations present on those systems by observing its evolution in time. Thus, in this section we present a systematic study of the off-resonant dynamics of a Rydberg system, which will allow us to gain more insight into the nature of the phenomena observed in that regime.However, before showing our results, a review of the theoretical description developed in [111] will be detailed.

4.2.1 Theoretical description

As in Ch. 3, we consider a system of N non interacting two-level atoms irradiated by a coherent laser field. The laser frequency is ω_L, and the energy difference between the ground and the excited states is ω_{gr}. Thus the detuning can be expressed as: $\delta = \omega_L - \omega_{gr}$. The system oscillates between the two levels with a *generalized* Rabi frequency: $\tilde{\Omega}(r) = \sqrt{\Omega(r)^2 + \delta^2}$ and amplitude $\frac{\Omega(r)^2}{\Omega^2(r)+\delta}$. From this, it is possible to predict the number of observed Rydberg excitations as:

$$N_{Rydb}(t) \approx \int n(r) \frac{\Omega(r)^2}{\Omega^2(r) + \delta} \cdot sin^2 \left(\frac{\Omega^2(r) + \delta^2}{2} \cdot t \right) \, \mathrm{d}V \tag{4.4}$$

where $n(r)$ is the local density.

As discussed in Ch. 3 , when atoms do not interact with each other, the system can be described as the single atom case. It must be taken into account only that, in case that the Rabi frequencies are not uniformly distributed along the sample, the oscillations of the number of atoms would be damped. The analysis of the interacting system case was performed using the theory developed in [30, 111], explained in detail in Ch. 3, but applied this time to the excitation of Rydberg atoms off-resonance.

Briefly, we know that the excitation rate, $\hat{\Gamma_k} = \Gamma_k/(\Omega^2/\gamma_\perp)$ (where k refers to the k^{th} position in the lattice, see Ch. 4) can be written as:

$$\hat{\Gamma} = \frac{1}{1+\epsilon_k^2} \tag{4.5}$$

where:

$$\epsilon_k = R^6 \left[\Delta - \sum_{j \neq k} \frac{n_j}{|r_k - r_j|^6} \right] \tag{4.6}$$

where $R = \frac{1}{a}\left(\frac{C_6}{\hbar\gamma_\perp}\right)$, a is the interparticle distance, and Δ is the rescaled detuning. Considering that the $70S_{1/2}$ state presents repulsive interactions, i.e. for positive detuning values, the rate of Eq.4.5 would be optimal at a distance given by the *facilitation* radius, r_{fac}:

$$r_{fac} = \left(\frac{C_6}{\hbar\delta}\right)^{1/6} = \left(\frac{\Omega_0}{\delta}\right)^{1/6} \cdot r_b \tag{4.7}$$

where r_b is the blockade radius: $r_b = \left(\frac{C_6}{\hbar\Omega_0}\right)^{1/6}$. As an example, for a detuning of $\delta = +10\,\text{MHz}$, Rabi frequency $\Omega_0 = +1\,\text{MHz}$, and the blockade radius of the $70S_{1/2}$ Rydberg state, $r_b = 10\,\mu\text{m}$; the facilitation radius is: $r_{fac} \approx 6.82\,\mu\text{m}$

The term *facilitation* radius was already used in [111] in analogy with kinetically constrained glass models, where the presence of excitations also alters the rate for the transitions of neighboring sites and thus, "facilitates" the dynamics [112, 113, 114].

Thus, the points that satisfy the equation:

$$0 = \sum_{j \neq k} \frac{n_j}{|r_{fac,k} - r_j|^6} - \Delta \tag{4.8}$$

define a facilitation surface for the k^{th} atom, $S_k(\Delta)$. Within this area, the atomic interactions compensate the energy difference, leading to resonant excitation dynamics. Due to the laser linewidth, $\gamma_\perp$, the distance r_{fac} presents an uncertainty, Δr_{fac}, dependent as well on the detuning. Taking this into account it is possible to define a facilitation volume, V_{fac}, from Eq.4.8. All atoms within this volume are resonant with the Rydberg transition with an excitation rate: $\Gamma_0 = \Omega^2/\gamma_\perp$. The size of the facilitation volume depends on the contributions of all the Rydberg atoms present in the sample. Each new excitation increases the volume size, leading to the formation of spatial structures, known as *aggregates* [35, 82, 22, 110, 73]. In analogy to the resonant case, the evolution is considered hierarchic due to the fact that atoms are excited sequentially. Hence, the probability of exciting one atom is conditioned to the previous excitations, whereas the probability of exciting simultaneously two or more atoms within the same facilitation volume is negligible.

As an example, we report here on the description of the off-resonant excitation process assuming the presence in the sample of an initial Rydberg excitation. The excitation rate of an atom situated at a distance r in the limit $\Omega^2 >> \gamma_\perp\gamma_\parallel$ is given by:

$$\Gamma(r) = \frac{\Omega^2}{\gamma_\perp}\frac{1}{1+\frac{1}{\hbar\gamma_\perp^2}\left(\hbar\delta - \frac{C_6}{r^6}\right)^2} \tag{4.9}$$

which means that Rydberg atoms are generated on resonance within the first facilitation volume. This volume can be imagined as an spherical shell of radius r_{fac}, allowing us to express it as:

$$V_{fac} = \frac{4\pi}{3}[(r_{fac}+\Delta r)^3 - r_{fac}^3] = \frac{2\pi\gamma_\perp}{3\delta^{3/2}}\left[1+\frac{\gamma_\perp}{6\delta}+\frac{\gamma_\perp^2}{108\delta^2}\right]\sqrt{\frac{C_6}{\hbar}} \tag{4.10}$$

where:

$$\Delta r = \left(\frac{C_6}{\hbar}\right)^{1/6}\frac{\gamma_\perp}{6\delta^{7/6}} \tag{4.11}$$

For the same parameters used to give a typical value of the facilitation radius ($\delta = +10\,\text{MHz}$, $\Omega_0 = 1\,\text{MHz}$ and $r_b = 10\,\mu\text{m}$) we obtain $\Delta_r \approx 0.082\,\mu\text{m}$

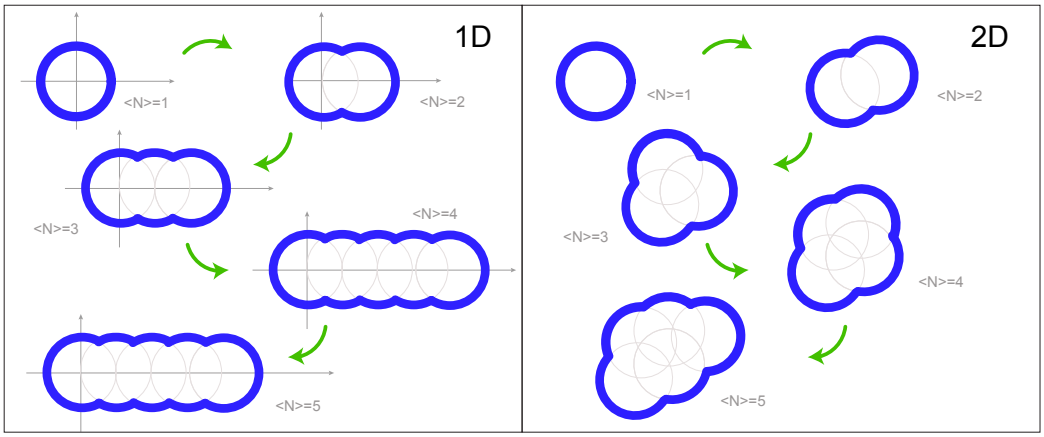

Figure 4.3: Illustration on the growth of the aggregate in $1D$ and $2D$. The facilitation surface (highlighted in blue) grows with the number of excitations.

The growth of the aggregate depends on many factors, not only on the evolution of the facilitation volume. First, the maximum number of subsequent excitations in the chain reaction process is proportional to the excitation time from the moment at which the first excitation is generated. Furthermore, for each step the generation of the subsequent excitation depends on the number of atoms within the facilitation volume:

$$\check{N} = V_{fac} \cdot n_{r_{fac}} \tag{4.12}$$

where $n(r_{fac})$ is the local density at r_{fac}. Clearly, the larger $\check{N}$, the higher is the probability of continuing the chain reaction. As mentioned above, the shape of the facilitation volume is defined considering the contributions of all the excitations. In order to illustrate this, we considered the case of a $1D$ system, where the excitations mainly happen along one axis (for instance, $\hat{x}$ axis). If the first excitation is placed on $x = 0$, then the second will happen at a distance r_{fac} form this point. The facilitation volume created from this second excitation is defined from Δ_r and the surface:

$$\hbar\delta - \frac{C_6}{(x^2+y^2+z^2)^3} - \frac{C_6}{((x-r_{fac})^2+y^2+z^2)^3} = 0 \tag{4.13}$$

from which it is possible to estimate that the third excitation will happen at a distance $r = 2r_{fac} + \Delta r$. Taking into account the strong dependence of the distance on the interaction strength ($\sim 1/r^6$), the contribution of the

previous excitations to the facilitation volume along the axis is negligible $\left(\frac{\Delta r}{r} \approx 1\%\right)$. For this reason, we assumed that all the excitations happen at a regular distance r_{fac} away from the others.

Figure 4.3 illustrates the aggregate growth. Although the width Δr_{fac} is not represented in the figure, we observed that the exact value of the facilitation volume and the one obtained taken into account the contribution of just one atom were practically the same, so the difference between them was neglected. From this, it is possible to extend the analysis to the subsequent excitations, accounting for the evolution of the facilitation volume. Hence, as the interaction volume is defined by the laser beams, the number of Rydberg excitations generated in the chain reaction process will be different depending on the geometrical configuration ($1D$ or $3D$) used in each experiment.

4.2.2 Experimental results

In this section we present the experimental results of the study of the dynamics of atoms off-resonantly excited to the $70S_{1/2}$ Rydberg state. We will show that these results are described in good approximation by the theory presented in the previous section. Moreover, making use of the full counting statistics analysis, we will extract additional information from the counting distributions that will be used to explain the correlations that emerge in these systems.

Dynamics of the off-resonant chain reaction excitation process

We can gain more insight into the mechanism of formation of those excitations by comparing the dynamics of Rydberg ensembles generated both resonantly and off-resonance under non-dissipative conditions ($\tau_{exc} < 150\,\mu$s). We create a MOT of $N = 78000$atoms and size $V = 50\,\mu\text{m} \cdot 40\,\mu\text{m} \cdot 44\,\mu\text{m}$. In this case we use the $3D$ laser beam configuration with Rabi frequencies of $1.6 \pm 0.32\,$MHz. In Fig.4.4 we present the results of these experiments: $\delta = 0\,$MHz (red diamonds), and off-resonance, both for positive ($\delta = +19 \pm 1\,$MHz, blue diamonds) and negative ($\delta = -19 \pm 1\,$MHz, green diamonds) detuning values: $\delta = \pm 19 \pm 1\,$MHz. In the three cases, the dashed lines are guides to the eye. On resonance we observe very fast dynamics for short τ_{excit} values, followed by a slow down of the dynamics at intermediate τ_{excit} values, due to the manifestation of the kinetic constraints (see Ch.4).

As anticipated before, the dynamics off-resonance exhibit different behavior not only with respect to the resonant case, but also comparing the results for the different signs of the detuning. Hence, during the first $5\,\mu$s of the process, where $\langle N \rangle < 1$, the dynamics behavior is independent of the sign of the detuning, as can be appreciated in the inset of the graph.

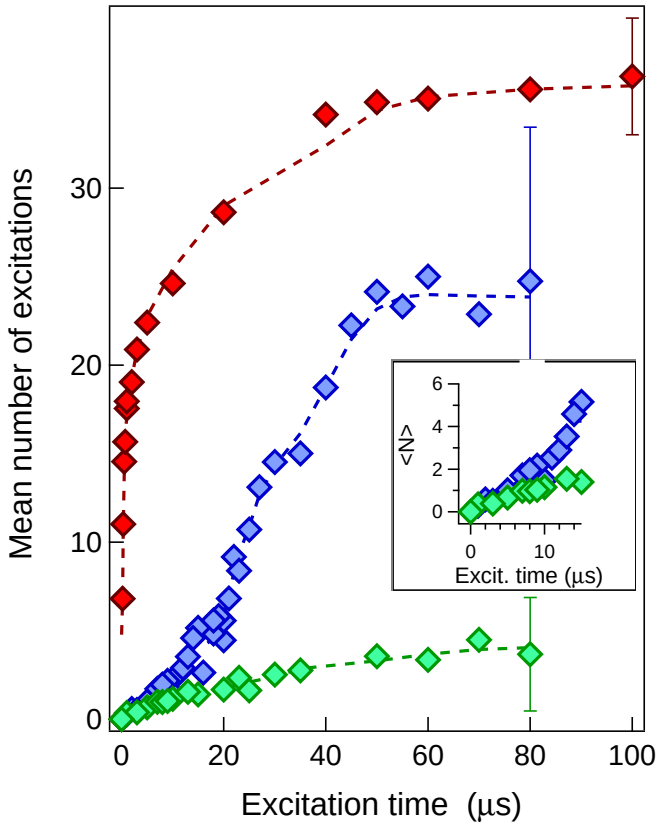

Figure 4.4: On and off resonance Rydberg excitation dynamics: red diamonds correspond to $\delta = 0\,\text{MHz}$, blue diamonds to $\delta = +19 \pm 1\,\text{MHz}$ and green diamonds to $\delta = -19 \pm 1\,\text{MHz}$. In the three cases, the dashed lines are guides to the eye. The error bars correspond to the measured standard deviation for each set of data. The experiment was performed using the $3D$ laser beam configuration with Rabi frequencies of $\Omega/2\Pi = 1.6 \pm 0.32\,\text{MHz}$ in a MOT of $N = 78000$ atoms and size $V = 50\,\mu\text{m} \cdot 40\,\mu\text{m} \cdot 44\,\mu\text{m}$ and density $1.6 \cdot 10^{11}\,\text{cm}^{-3}$.

This interval of time corresponds to the first stage of the off-resonant excitation process where no Rydberg atoms are present in the sample.Once the first excitation (on average) occurs, ($\tau > 5\,\mu\text{s}$), the two curves start to diverge. In the positive detuning case (blue diamonds), each atom located at the right distance could be shifted into resonance and thus be excited to the Rydberg state, leading to an increase of the excitation rate. By contrast, for the negative detuning case (green diamonds), the excitation rate does not increase because the resonant condition is never satisfied. This explains why the curve is almost flat even for the highest values of the excitation time.

From these results, we distinguish three different stages in the off-resonant excitation process:

- An *ignition* stage, characterized by an excitation rate corresponding to the single atom case, which in the limit $\delta >> \gamma_\perp$ is:

$$\Gamma(\delta) \approx \frac{\Omega^2 \gamma_\perp}{\delta^2} \tag{4.14}$$

- A *facilitation* stage, where the initial Rydberg excitation serves to begin the aggregate growth process throughout subsequent excitation of the neighboring atoms, leading to a chain reaction excitation process with a rate:

$$\Gamma_0 = \frac{4\Omega^2}{\gamma_\perp} \tag{4.15}$$

- An *avalanche* stage, where the size of V_{fac} is maximum and interesting phenomena arise, specially in the highly dissipative regime.

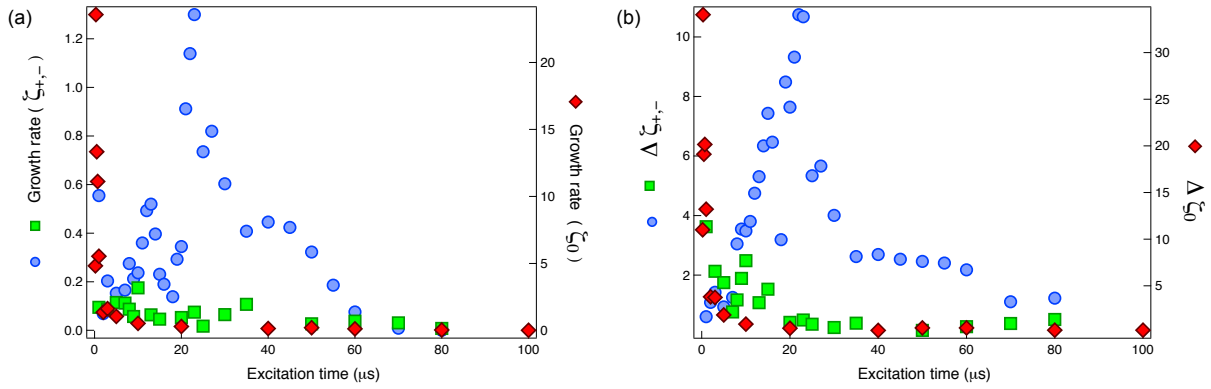

Figure 4.5: Growth rates ($\zeta_i(\tau)$) calculated for the experimental data shown in Fig. 4.4: $\delta = 0\,\text{MHz}$ (red diamonds), $\delta = +19 \pm 1\,\text{MHz}$ (blue circles) and $\delta = -19 \pm 1\,\text{MHz}$ (green squares). In (b) we show the error of these measurements obtained from the standard deviation of the experimental data shown in Fig. 4.4.

A direct comparison between the dynamics in the first and second stages must be done carefully. An absolute estimation of the excitation rate is not simple, due to the inhomogeneous distribution of the Rabi frequency and the atomic density within the facilitation volume. Nevertheless, we observed that the ratio between the excitation rate in these two stages was independent of those quantities and reproduced the single atom one:

$$\Gamma_0/\Gamma(\delta) \simeq 4\delta^2/\gamma^2 >> 1 \tag{4.16}$$

According to this expression we expect an increase of the excitation rate when the dynamics goes from the ignition to the facilitation stage. In order to quantify the evolution of the excitation rates, we can calculate the growth rates as:

$$\zeta_{0,\pm}(\tau) = [N(\tau_1) - N(\tau_2)/(\tau_1 - \tau_2)] \tag{4.17}$$

where ζ_+, ζ_- indicate the growth rates for positive and negative values of the detuning, respectively and ζ_0 refers to the resonant case.

Fig.4.5(a) shows the results of these calculations for the three values of the detuning of the experimental data presented in Fig.4.4: $\delta = 0$ (red diamonds), $\delta = +19 \pm 1\,\mathrm{MHz}$ (blue circles) and $\delta = -19 \pm 1\,\mathrm{MHz}$ (green squares). Fig.4.5(b) shows the error $\Delta\zeta_i$ of the results presented in Fig.4.5(a) obtained from the standard deviation of the measurements presented in Fig. 4.4.

The resonant case, exhibits a strong decrease of the growth rate for $\tau > 1 - 2\,\mu$s due to the blockade effect, reaching a similar value to the one shown by the negative detuning case (green squares). By contrast, the data corresponding to the positive detuning, shows an increase of the growth rate for $20\,\mu\mathrm{s} < \tau < 50\,\mu\mathrm{s}$, reaching its maximum at $\zeta_{+,max} = 1.3\,\mu\mathrm{s}^{-1}$. This value agrees with the expected one, calculated according to Eq. 4.14. For the negative detunig case, however, the value given by Eq. 4.14 and $\zeta_- = 0.075\,\mu\mathrm{s}^{-1}$ differs by a factor of ~ 10. These calculations were done neglecting the fact that both the Rabi frequency and the density of the sample are inhomogeneously distributed in the cloud, which can explain the differences between the measured values and the calculated ones. In fact, this difference is more pronounced when the calculation is done for the data taken on resonance. From the measured values, we obtained a growth rate $\zeta_{0,max} \approx 23$ at $\tau = 0.2\,\mu$s. By estimating the excitation rate taking into account the peak values of the Rabi frequency and the density, we obtain a value of Γ which is higher than the experimental one by a factor of ~ 100. For this reason we repeat this calculation but, this time, calculating the Rabi frequency and the density values for the different blockade spheres. Doing this, a value $\Gamma \approx 68$ is obtained, in good agreement with the experimental observation. This result evidences once more (see Ch. 3) the extremely sensitivity to the Rabi frequency and density distribution of these experiments. Here a factor of 30 is missing between the theoretical calculation and the one taken into account the inhomogeneous distribution along the sample.

Fig.4.5(a) also shows two different saturation values for the resonant and the positive detuning cases. The latter one is difficult to interpret because it depends strongly both on the density of the sample as well as on the detuning. These parameters determine the probability of continuing the aggregate growth when changing $\check{N}$. An intuitive interpretation could be that the growth of the aggregate is interrupted before occupying the whole interaction volume, which can be explained due to the decrease of the density for big sizes of the aggregate.

In the following, we will show the technique employed to skip the first stage, in order to focus the experiments on the facilitation stage. The avalanche stage has been also studied in detail and the results of that investigation will be presented in an independent Chapter of this thesis, Ch. 5.

Controlling the aggregates growing: idea of the seed

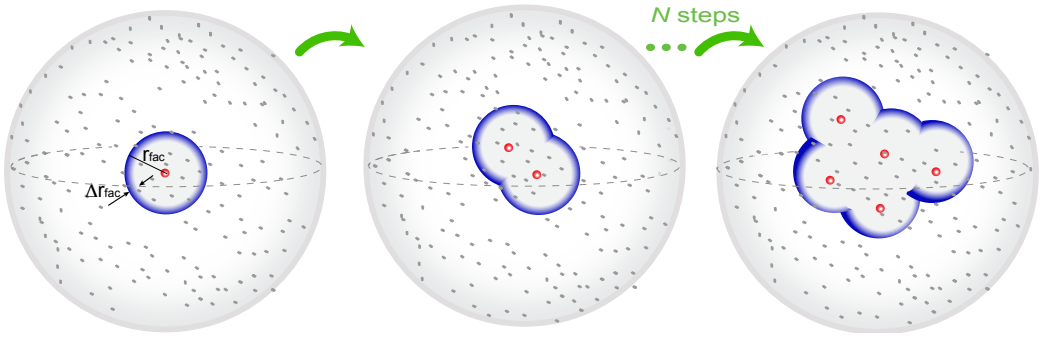

Figure 4.6: Illustration describing the seed technique. When the seed is inserted in the center of the sample, it generates a facilitation volume around it (left). An atom within this volume satisfies the off-resonant excitation condition, leading to the formation of an aggregate (center). The growth of the aggregate is a sequential process that happens in any spatial direction (right). After N steps, the aggregate will have N excitations. This value is very sensitive to the conditions of the aggregate growth (i.e. density).

The conclusions obtained regarding to the off-resonant excitation rate motivated a series of experiments to try to control it. To do so, we took into account that the growth of the aggregate during the facilitation stage depends on the presence of an initial Rydberg excitation, which starts the chain reaction. In the experiments shown previously this event could happen at any time of the dynamics, but now we present a technique which allows us to insert in the system an initial Rydberg excitation, acting as a seed, in order

to isolate the facilitation stage and study the chain-reaction process more in detail. Figure 4.6 illustrates this concept. The *seed* was generated in the system using the technique described in Ch.2. The duration and timing of the seed impulse were easily controllable, allowing us to control the mean number of seeds generated, as well as the precise moment at which it was inserted in the sample. Once a seed is present in the sample, it defines a facilitation volume, V_{fac} within which the excitations to the Rydberg state happen with an excitation rate: Γ_0. The generation of a seed is not a deterministic process, but presents a statistical uncertainty. By irradiating the cloud with a resonant light pulse of duration τ_{seed} we obtained a certain value of $\langle N_{seed} \rangle$, which was kept around 1 in order to neglect processes with multiple seeds and consider predominantly the cases having 0 or 1 seed. Nevertheless, this should not create strong restrictions. In fact, if more than 1 seed is generated in the sample, then we expect to create several independent aggregates, that could also combine among themselves while growing. For this reason, the maximum number of excitations depends more on the conditions of the aggregate growth, like the density, than on the initial number of seeds, as we have experimentally proven with an experiment that will be shown in the following.

In order to test qualitatively the effect of the seed on the dynamics, we perform an experiment using the $3D$ configuration, in which a fixed number of seeds $\langle N_{seed} \rangle \simeq 2$ is inserted at different times of the dynamics: $\tau = 10\,\mu\text{s}, 24\,\mu\text{s}, 45\,\mu\text{s}$ The MOT we use has $N = 170000$ atoms, size $V = 160\,\mu\text{m} \cdot 100\,\mu\text{m} \cdot 130\,\mu\text{m}$ and density of $n \approx 1.55 \cdot 10^{11} cm^{-3}$.The Rabi frequency of the resonant process is set to a low value: $\Omega = 270 \pm 54\,\text{kHz}$ in order to minimize the creation of spontaneous seeds before the desired time, and the excitation laser was detuned by $\delta = +75 \pm 1\,\text{MHz}$. The results of this experiment are shown in Fig.4.7, from which it is clear that the beginning of the facilitation stage corresponds to the times at which the seed was inserted in the sample. To verify the effect of the number of seeds on the dynamics, we realize an experiment, always using the $3D$ configuration, in which we measure the mean number of excitations as a function of the mean number of seeds. The laser pulse of fixed total duration of $\tau = 100\,\mu\text{s}$ is divided in two parts: a first one on resonance (τ_{seed}), in order to create the seed; and, a second one off-resonance, where the facilitation stage occurs. The mean number of seeds is changed by varying τ_{seed} using the technique described in Ch.2.

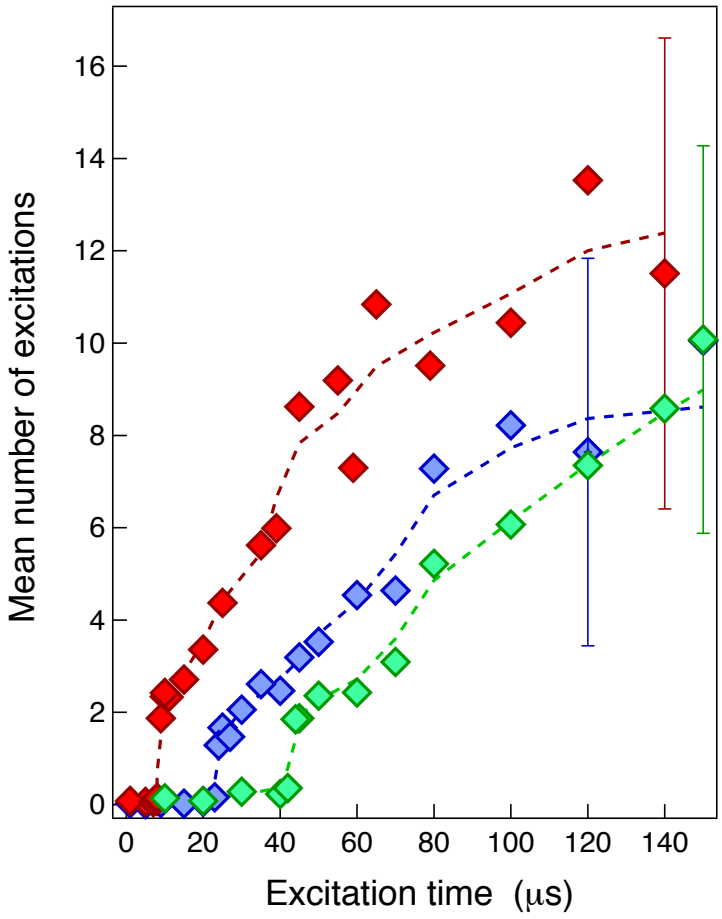

Figure 4.7: Off-resonant Rydberg excitation dynamics using an initial seed in $3D$. A fixed number of seeds $\langle N_{seed}\rangle \simeq 2$ was inserted at different times of the dynamics: $\tau = 10\,\mu$s(red diamonds), $25\,\mu$s (blue diamonds), $45\,\mu$s(green diamonds). Dashed lines are guides to the eye. The excitation laser was detuned by: $\delta = +75 \pm 1\,$MHz, the Rabi frequency of process was: $\Omega = 270 \pm 54\,$kHz and the MOT density was: $n \approx 1.55 \cdot 10^{11} cm^{-3}$

In this experiment, τ_{seed} is varied from 0 to $0.5\,\mu$s which lead to a variation in the mean number from $\langle N_{seed}\rangle = 0$ to $\langle N_{seed}\rangle = 5$. Consequently, the mean number of excitations $\langle N\rangle$ is obtained after an off-resonant impulse of duration $\tau - \tau_{seed}$. The MOT has $N = 90000$ atoms, size $V = 60\,\mu\text{m} \cdot 50\,\mu\text{m} \cdot 55\,\mu\text{m}$ and density of $n \approx 8.5 \cdot 10^{10} cm^{-3}$. The excitation laser is detuned by: $\delta = +27 \pm 1\,$MHz and the Rabi frequency of the process is: $\Omega = 280 \pm 56\,$kHz. Fig.4.8 shows the results of this experiment. On it, $\langle N\rangle$ increases notably once the seed is present in the sample, which we interpret as a clear sign of the growth of the aggregate. Furthermore, we observe that after a certain number of seeds, $\langle N_{seed}\rangle \approx 1$, the saturation value of $\langle N\rangle \sim 20$ is reached, indicating that the aggregate stopped growing. This confirms our

initial hypothesis that the number of seeds does not influence the maximum number of excitations that can be reached by the chain reaction process.

The Mandel Q-factor exhibits high positive values, characteristic of super-Poissonian statistics, when the $\langle N_{seed} \rangle \leq 1$; whereas, for larger ones, the Q-factor goes close to zero, indicating Poissonian behavior.

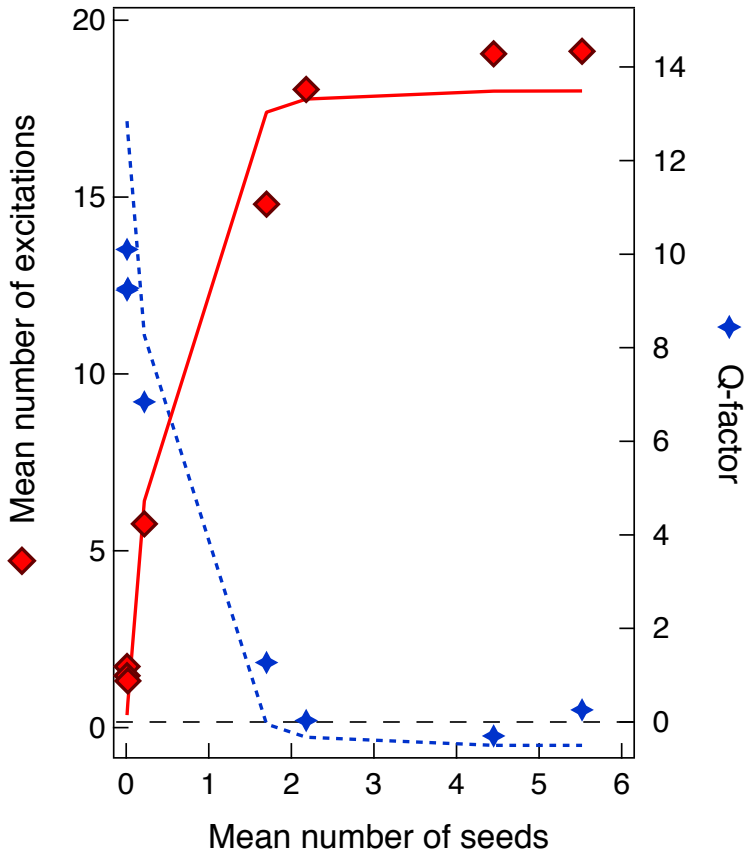

Figure 4.8: Mean number of excitations as a function of the mean number of initial seeds (red points) and Mandel Q-parameter as a function of the mean number of seeds (blue). The lines (continuous red line for the mean number of excitations, dashed blue line for the Mandel Q-parameter) correspond to a simple model which simulates the excitation dynamics taking into account the probability of having no seed or having at least one seed in the system. The laser pulse duration was fixed to $\tau = 100\,\mu$s. The excitation laser was detuned by: $\delta = +27 \pm 1\,$MHz, the Rabi frequency of process was: $\Omega = 280 \pm 56\,$kHz and the MOT density was: $n \approx 8.5 \cdot 10^{10} cm^{-3}$

In Fig.4.8 we also include the results of a simple model (continuous red line for the mean number of excitations and dashed blue line for the Mandel Q-parameter) which accounts for the probability of having no seed or having

at least one seed, and that represents a very good approximation of the excitation dynamics. The mean number of excitations can be obtained from:

$$\langle N \rangle^{th} = P(N_{seed} = 0) \cdot N_1 + P(N_{seed} \geq 1) \cdot N_2 \tag{4.18}$$

a bimodal probability distribution, where N_1 and N_2 the mean number of excitations of each mode, $P(N_{seed} = 0)$ is the probability of having no seed, and $P(N_{seed} \geq 1)$ the probability of having, at least, one seed.

Additionally,we consider the following hypothesis:

- The probability of having one seed is Poissonian, so $P(N_{seed} = 0)$ and $P(N_{seed} \geq 1)$ are given by:

$$\begin{aligned} P(N_{seed} = 0) &= e^{-\langle N_{seed} \rangle} \\ P(N_{seed} \geq 1) &= 1 - e^{-\langle N_{seed} \rangle} \end{aligned} \tag{4.19}$$

- In the absence of any seed, the chain reaction does not start and, consequently, $N_1 = 0$. By contrast, in presence of one seed at least, this model assumes that the chain reaction process continues up to $N_2 = 20$.

The good agreement obtained between the simulation results and the experimental observations shows that the simple bimodal model is able to determine in good approximation the final number of excitations.

Analysis of the histograms of the counting distributions

In the previous section we provided a description of the facilitation stage of the off-resonant excitation dynamics, where the aggregates growth determined the final mean number of Rydberg excitations of the system. However, this is not enough in order to describe completely the process. Some experimental works [35, 29, 110, 82, 101] proved the usefulness of the analysis of the full counting distributions, which can be a powerful tool in order not only to understand better the excitation of Rydberg atoms off-resonance but also to highlight the main differences of the off-resonant processes and the resonant ones. Here we focused on the analysis of the histograms of the counting distributions as a function of different parameters, like the detuning or the density of the sample.

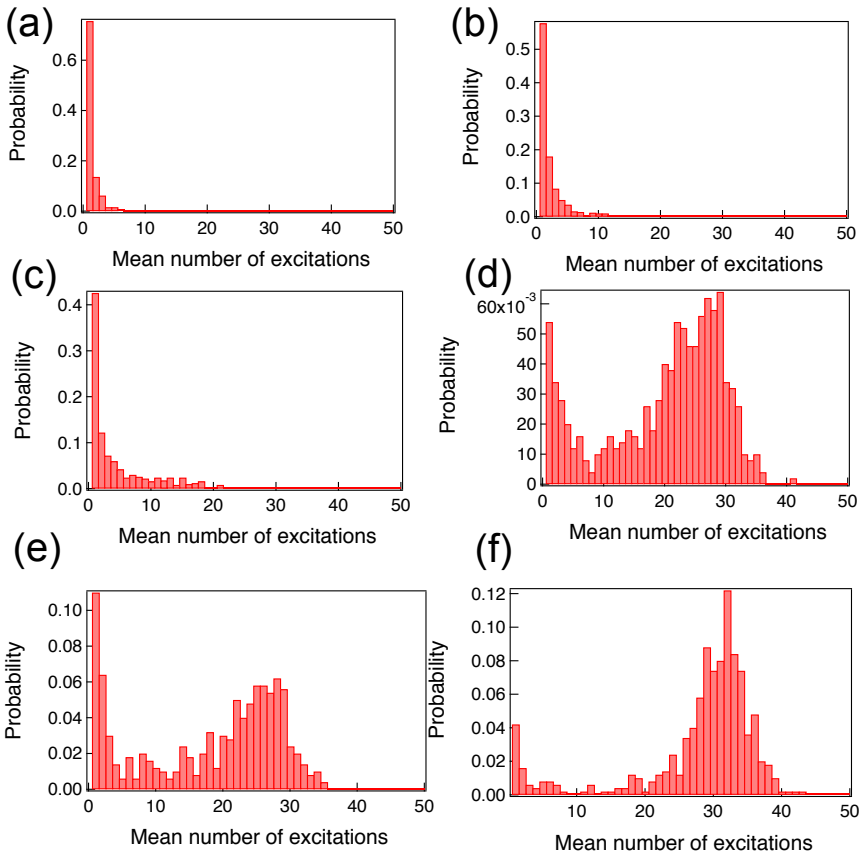

Figure 4.9: Histograms of the counting distributions of the excitation of Rydberg atoms off-resonance as a function of the excitation time. The experiments were performed using the $3D$ configuration of the laser beams with a Rabi frequency of 290 ± 58 kHz. The excitation laser was detuned by $\delta = +10 \pm 1$ MHz. The histograms correspond to different values of the excitation time (a) $\tau_{exc} = 5\,\mu$s; (b) $\tau_{exc} = 10\,\mu$s; (c) $\tau_{exc} = 20\,\mu$s; (d) $\tau_{exc} = 30\,\mu$s; (e) $\tau_{exc} = 50\,\mu$s; (f) $\tau_{exc} = 100\,\mu$s

In order to illustrate this, we present in Fig.4.9 the histograms of the counting distributions of a Rydberg sample off-resonantly excited as a function of the excitation time. The detuning of the excitation laser was set to $\delta = +10 \pm 1$ MHz and the Rabi frequency of the process was 290 ± 58 kHz. This experiment was done using the $3D$ configuration with a MOT containing $N = 80000$ atoms, size $V = 45\,\mu\text{m} \cdot 42\,\mu\text{m} \cdot 44\,\mu\text{m}$ and density $n \approx 1.6 \cdot 10^{11} cm^{-3}$. The histograms exhibit a different shape as τ_{exc} is increased. Thus, for $\tau_{exc} < 20\,\mu$s (Fig. 4.9(a),(b)) the histograms present only one peak centered around zero; whereas, for $\tau_{exc} \geq 20\,\mu$s the presence

of a second peak centered around the mean number of excitations becomes evident.

In the experiments the density is not uniform, and precisely this fact, together with the probabilistic nature of the start of the facilitation stage, are the dominating factors in the aggregate growth. In analogy to the experiment of Fig. 4.9, we measured the histograms of the counting distributions of the off-resonant excitation of Rydberg atoms when an initial seed is used.

These results were also compared to a model which reproduces qualitatively the evolution of counting distributions within the facilitation volume for different numbers of atoms within the facilitation volume, $\check{N}$. The model simulates the behavior of a $1D$ system with density $n(x) = n_0 exp\left[-\frac{x^2}{2\sigma^2}\right]$. An initial excitation placed at the center of the system allows the chain reaction process to begin. Additionally, we assumed that the Rabi frequency is high enough so that if, at least, one atom is present in the facilitation volume, then one Rydberg excitation is generated with 100% probability.

In this model we considered just two quantities: the number of steps of the excitation chain, K, and the number of ground state atoms within the facilitation volume, $\check{N}$. For each step, the model calculates the probability $P_i(\check{N})$ of having at least one atom in the ground state within V_{fac}. Regarding $P_i(\check{N})$, we made some extra assumptions:

- *Independency*: atoms in the ground state do not interact with each other so, their relative positions within the volume are independent.

- *Regularity*: the number of atoms contained in the facilitation volume is proportional to the volume and to the atomic density.

- *Stationarity*: taking into account the typical time and temperature values ($T \sim 150\,\mu$K, averaged velocity $0.23\,$m/s) of the experiments, the positions of the atoms within the sample may be considered fixed. So, the probability of having a certain number of atoms within a certain volume is independent of time.

These assumptions allowed us to consider the number of ground state atoms contained in the facilitation volume to be described by a Poisson distribution. Hence, given $\langle\check{N}\rangle$, it is possible to calculate the probability of having $\check{N}$ atoms within the facilitation volume:

$$P(\check{N}) = \frac{\check{N}^{\langle\check{N}\rangle}}{N!} e^{-\langle\check{N}\rangle} \tag{4.20}$$

As we already know, in order to start the sequence of steps it was necessary to have, at least, one seed which for convenience was set to $x = 0$. Thus, for a given mean number of seeds, $\langle N_{seed} \rangle$, the probability of having $\check{N}$ atoms within the facilitation volume was:

$$P_{start} = [1 - P_{seed}(0)] = [1 - e^{\langle N_{seed} \rangle}] \tag{4.21}$$

In the model, the facilitation volume was estimated considering only the contribution of the previous step excited atom:

$$V_{fac}(\delta) = 4\pi r_{fac}^2(\delta) \cdot \Delta r(\delta) \tag{4.22}$$

Additionally, we considered that the system evolves only towards the positive values of x, as is represented in Fig.4.10.

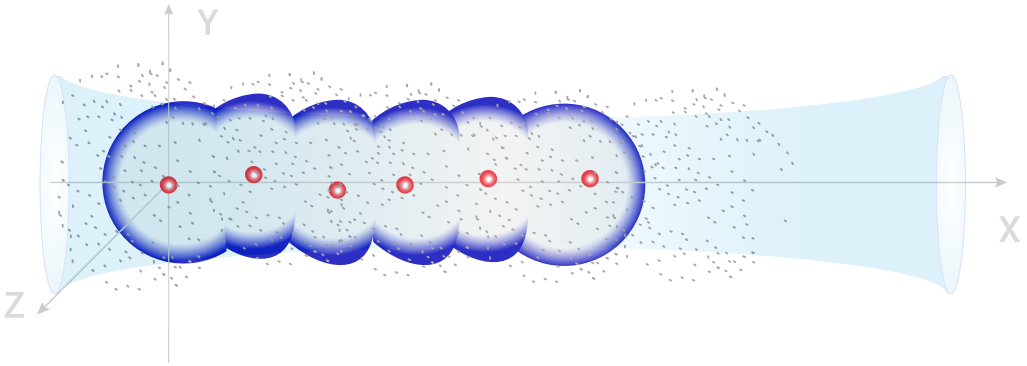

Figure 4.10: Illustration on the quasi $1D$ model with the 421 nm beam on the x axis.

The mean number of atoms within the facilitation volume for a given value of the local density can be obtained:

$$\langle \check{N}(x) \rangle = [4\pi r_{fac}^2 \cdot \Delta r] \cdot n_0 exp\left[\frac{-x^2}{2\sigma^2}\right] = N_0 exp\left[\frac{-x^2}{2\sigma^2}\right] \tag{4.23}$$

Then, assuming a Poissonian probability distribution, this value determines the probability of having at least one atom within the facilitation volume and continue the chain reaction:

$$P(\check{N} \geq 1) = 1 - P(0) = 1 - e^{\langle \check{N}(x) \rangle} \tag{4.24}$$

The maximum number of steps of the process was determined by the Rabi frequency and the excitation time, assuming that each single step happens within the coherent regime, $\sim \Omega \cdot \tau$.

The probability of doing at least K steps is given by:

$$P_A = \prod_{i=1}^{K} (1 - exp[-N_0 \cdot exp[-i^2 \cdot \frac{r_{fac}^2}{2\sigma^2}]]) \tag{4.25}$$

whereas, the probability of not continuing the chain reaction is:

$$P_B = exp[-N_0 \cdot exp[-(K+1)^2 \cdot \frac{r_{fac}^2}{2\sigma^2}] \tag{4.26}$$

Consequently, the probability of doing exactly K steps,corresponding also to the number of Rydberg atoms, is:

$$P_K = P_{start} \cdot P_A \cdot P_B \tag{4.27}$$

Finally, the mean number of excitations to the Rydberg state happening after the seed can be calculated as:

$$\langle N \rangle = \sum_{K=1}^{M} K \cdot P_{norm}(K) \tag{4.28}$$

where P_{norm} is the normalized probability:

$$P_{norm}(K) = \frac{P(K)}{\sum_{i=1}^{M} P_i} \tag{4.29}$$

with M the maximum number of steps.

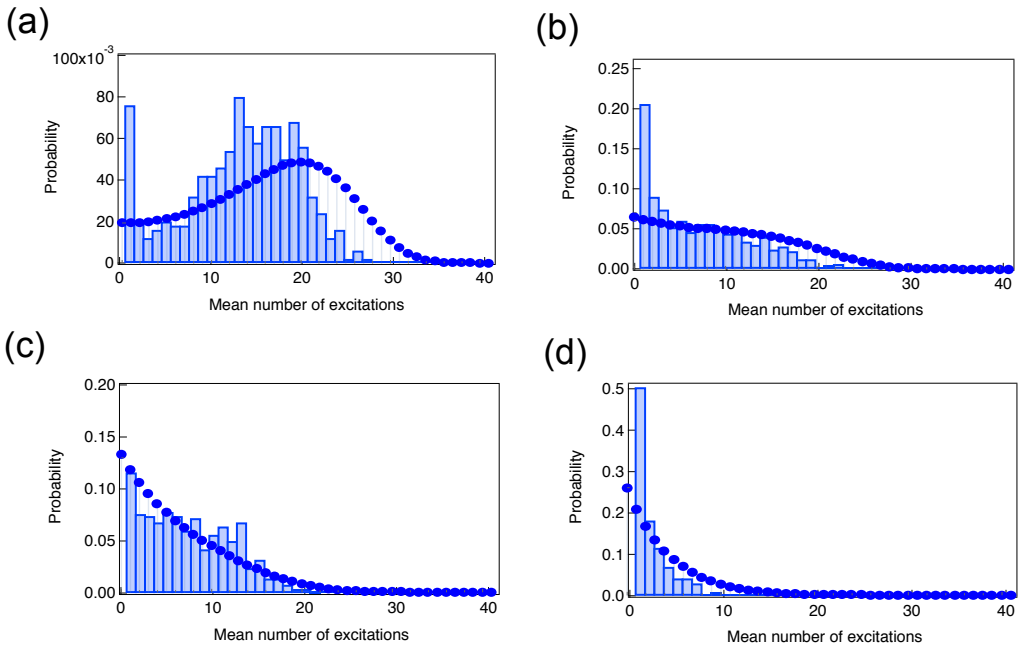

Figure 4.11: Histograms of the counting distributions of the excitation of Rydberg atoms off-resonance as a function of the detuning (bars) together with numerical simulations (points). The experiments were performed using the $1D$ configuration of the laser beams. The Rabi frequency was $520 \pm 100\,\text{kHz}$, the laser was detuned by $\delta = +12 \pm 1\,\text{MHz}$ and the excitation time was set to $\tau = 100\,\mu\text{s}$. The density of the sample was varied using the depumping beam technique (a) $\delta = +12\,\text{MHz}$; (b) $\delta = +15\,\text{MHz}$; (c) $\delta = +18\,\text{MHz}$; (d) $\delta = +22\,\text{MHz}$.

To start with, we study the qualitative behavior of the histograms of the counting distributions of a Rydberg sample excited off-resonance as a function of the size of the facilitation volume, which, from Eq.4.10 we know is proportional to δ. To perform this experiment we use a MOT of $N = 2.9 \cdot 10^6$ atoms and size $V = 224\,\mu\text{m} \cdot 132\,\mu\text{m} \cdot 172\,\mu\text{m}$ with maximum density of $n_0 = 1 \cdot 10^{11}\,\text{cm}^{-3}$. Here we use the $1D$ laser beam configuration with Rabi frequency $520 \pm 100\,\text{kHz}$. In Fig.4.11 we report on the results of these experiments for detuning ranging from $\delta = +12\,\text{MHz}$ to $\delta = +22\,\text{MHz}$. Our results show that the histograms present bimodal character only for low values of the detuning, which can be explained considering the variation of the size of the facilitation volume. Hence, for high values of the detuning the facilitation volume decreases, because $V_{fac} \propto \delta^{-3/2}$ for each step and, the same happens with the mean number of atoms within it. A lower value

of $\langle \check{N} \rangle$ means a lower probability of continuing the excitation sequence. We perform also the numerical simulation using the $1D$ model described above (blue points) for each case, which reproduces qualitatively the variation of the distributions character: from monomodal to bimodal. In the latter case, however, the simulations show only one peak centered around the mean value of the excitations but not the one centered around zero, which can be explained due to the simplicity of the model.

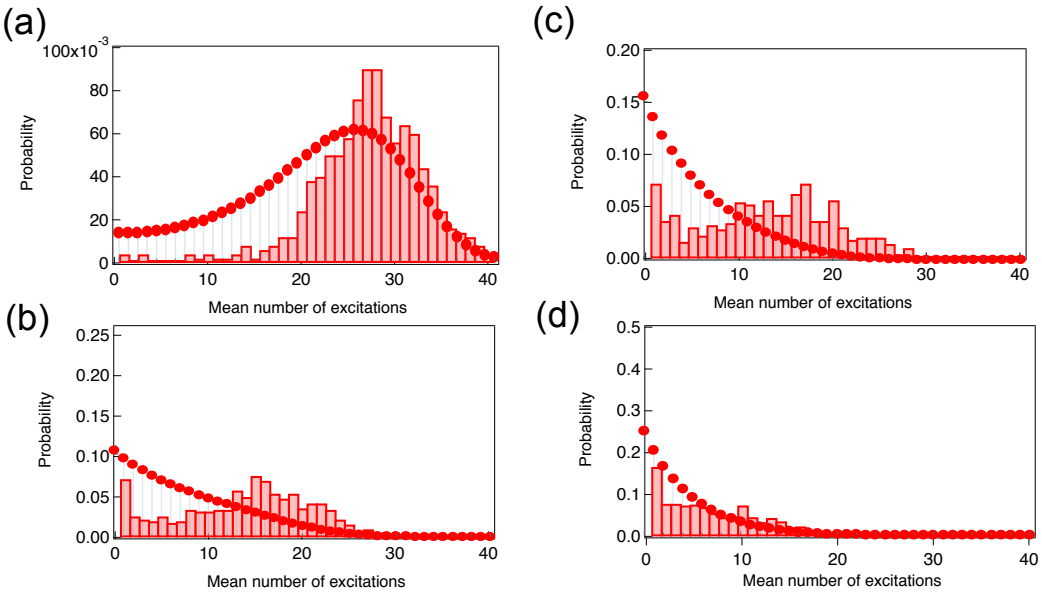

Figure 4.12: Histograms of the counting distributions of the excitation of Rydberg atoms off-resonance as a function of the density of the sample (bars) together with numerical simulations (points). The experiments were performed using the $1D$ configuration of the laser beams. The Rabi frequency was $520 \pm 100\,\mathrm{kHz}$, the laser was detuned by $\delta = +12 \pm 1\,\mathrm{MHz}$ and the excitation time was set to $\tau = 100\,\mu\mathrm{s}$. The density of the sample was varied using the depumping beam technique: (a) $n \simeq 9.1 \cdot 10^{10}\,\mathrm{cm}^{-3}$; (b) $n \simeq 4.7 \cdot 10^{10}\,\mathrm{cm}^{-3}$; (c) $n \simeq 4.0 \cdot 10^{10}\,\mathrm{cm}^{-3}$; (d) $n \simeq 3.3 \cdot 10^{10}\,\mathrm{cm}^{-3}$.

In order to study the qualitative behavior of the counting distributions with the the number of atoms within the facilitation volume, $\check{N}$, the density of the cloud was varied using the depumping beam technique (see Ch. 2), from $n(x) \simeq 9 \cdot 10^{10}\,\mathrm{cm}^{-3}$ to $n(x) \simeq 2.6 \cdot 10^{10}\,\mathrm{cm}^{-3}$. In Fig.4.13 we show the histograms corresponding to the counting distributions of a Rydberg sample excited off-resonance using an initial seed for different values of the density of the sample (red color). In those experiments, we used a MOT of $N = 3.8 \cdot 10^6$ atoms and size $V = 250\,\mu\mathrm{m} \cdot 155\,\mu\mathrm{m} \cdot 197\,\mu\mathrm{m}$. Also in this case, the experiment

was performed in $1D$, with Rabi frequency of $520 \pm 100\,\mathrm{kHz}$. In all cases, the laser was detuned by $\delta = +12 \pm 1\,\mathrm{MHz}$ and the excitation time was set to $\tau = 100\,\mu\mathrm{s}$.

For the highest density cases, the distributions are clearly bimodal (Fig.4.13(a)-(c)) whereas, when the density is lower than $n \simeq 3.0{\cdot}10^{10}\,\mathrm{cm}^{-3}$ (Fig.4.12(d)), the histograms exhibit just one peak centered around zero. The numerical simulations using the $1D$ model (red points) reproduce in good qualitative agreement the behavior of the observed counting distributions. In order to improve the degree of this agreement, we increased the density of the sample by a 30% in the calculations. This is justified, on one hand, due to the uncertainties on the measurement of this parameter, and, on the other, due to the extremely sensitivity that the model presents to this parameter.

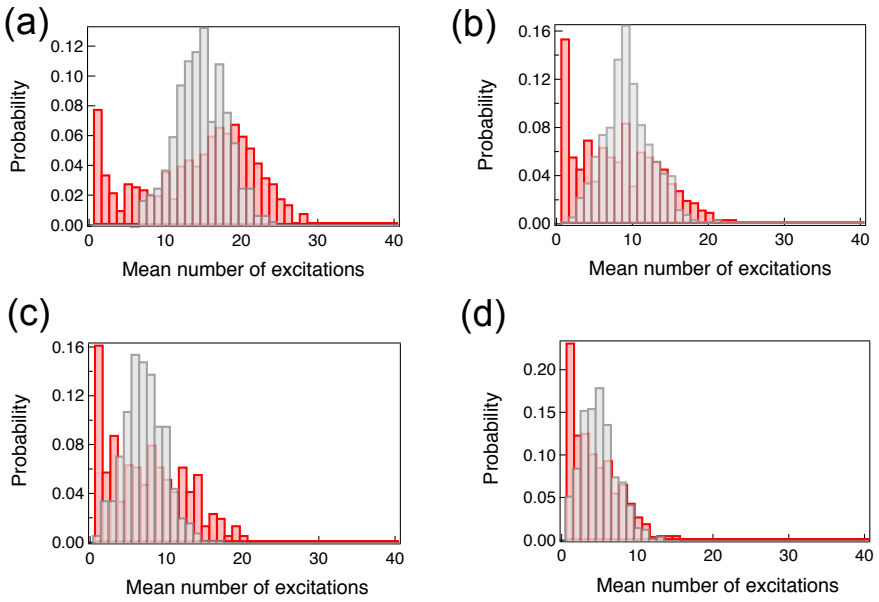

Figure 4.13: Histograms of the counting distributions as a function of the density of the sample for off-resonant Rydberg excitation case (red histograms) as well as for the resonant excitation case (grey histograms). The density of the sample was varied using the depumping beam technique. The figures in the same row, presented similar values of density and mean number of excitations: (a) $\delta = +12\,\mathrm{MHz}$, $n(x) \simeq 9.1 \cdot 10^{10}\,\mathrm{cm}^{-3}$, $\langle N \rangle \simeq 13.2$ (red); $\delta = 0\,\mathrm{MHz}$, $n \simeq 7.6 \cdot 10^{10}\,\mathrm{cm}^{-3}$, $\langle N \rangle \simeq 13.7$ (grey). (b)$\delta = +12\,\mathrm{MHz}$, $n \simeq 4.0{\cdot}10^{10}\,\mathrm{cm}^{-3}$, $\langle N \rangle \simeq 7.2$ (red); $\delta = 0\,\mathrm{MHz}$, $n \simeq 3.0{\cdot}10^{10}\,\mathrm{cm}^{-3}$, $\langle N \rangle \simeq 8.3$ (grey). (c) $\delta = +12\,\mathrm{MHz}$, $n \simeq 3.2 \cdot 10^{10}\,\mathrm{cm}^{-3}$, $\langle N \rangle \simeq 6.5$ (red); $\delta = 0\,\mathrm{MHz}$, $n \simeq 2.0 \cdot 10^{10}\,\mathrm{cm}^{-3}$, $\langle N \rangle \simeq 6.2$(grey). (d) $\delta = +12\,\mathrm{MHz}$, $n \simeq 2.6 \cdot 10^{10}\,\mathrm{cm}^{-3}$, $\langle N \rangle \simeq 3.4$ (red); (h) $\delta = 0\,\mathrm{MHz}$, $n \simeq 1.1 \cdot 10^{10}\,\mathrm{cm}^{-3}$, $\langle N \rangle \simeq 4$ (grey).

For comparison, we repeated the same experiment on resonance, in or-

der to observe the qualitative differences between the two processes. The experiments were realized using a MOT of $N = 2.6 \cdot 10^6$ atoms and size $V = 255\,\mu\text{m} \cdot 145\,\mu\text{m} \cdot 190\,\mu\text{m}$, and Rabi frequency of $503 \pm 100\,\text{kHz}$. Also here we used the depumping beam technique to vary the density of the sample from $n \simeq 7.6 \cdot 10^{10}\,\text{cm}^{-3}$ to $n \simeq 0.33 \cdot 10^{10}\,\text{cm}^{-3}$.In this case, the excitation time was reduced to $\tau = 15\,\mu\text{s}$ to obtain mean number of excitations similar to the ones of the off-resonant case. In Fig.4.13 we compared the qualitative behavior of the counting distributions. The grey histograms (Fig.4.13 (b),(d),(f) and (h)) corresponds to the histograms obtained for $\delta = 0\,\text{MHz}$, whereas the red ones (Fig.4.13 (a),(c),(e) and (g)) showed the results obtained for $\delta = +12\,\text{MHz}$. On resonance, the distributions preserved its monomodal shape, centered around a mean value that decreases with the density, for the whole range of study; whereas, off-resonance, the counting distributions exhibited a bimodal shape for the highest density values and a peaked shape centered around the mean number of excitations for the lowest density cases, as we also seen in Fig.4.12.

The comparison between red ($\delta = +12\,\text{MHz}$) and grey ($\delta = 0\,\text{MHz}$) histograms in Fig.4.13 evidences the qualitative differences between the excitation of Rydberg atoms on resonance and off-resonance. On resonance, the correlations become less and less important while the density decreases (see also Ch.3); starting, for the highest density case, with a sub-Poissonian distribution, consequence of the dipole blockade, and finishing with a Poissonian, centered around the mean value, for the lowest value of the density. By contrast, off-resonance the role of the interactions determines the aggregates formation even at low densities; where due to the chain reaction mechanism, the presence of at least one excitation influences the subsequent ones and creating strong correlations in the system. This is evidenced by the shape of the distributions, which off-resonance are exponential with a long tail towards high numbers, whereas, for the resonant case this shape is not observed.

4.3 Summary and perspectives

In this Chapter we analyzed the formation of off-resonant Rydberg excitations as well as the dynamics in this regime. Under non-dissipative conditions, we identified experimentally three different stages within this process: ignition, facilitation and avalanche. In order to focus our studies in the facilitation stage, we presented a simple technique in which a seed is inserted in the sample allowing us to skip the first stage and realize a controllable study of the second one. By analyzing the full counting statistics of our measurements, we manage to observe how the chain reaction excitation process evolves in time. Specially, the histograms of the distribution of the excitation

events revealed the extremely sensitivity of this process on the detuning or the density of the sample. These results help us to understood how the chain reaction excitation process works, as well as to obtain an agreement with the theoretical predictions of [111]. Moreover, we observed that, under certain conditions, those distributions present bimodal shape, that are compatible with intermittency phenomena or coexistence of dynamical phases as predicted theoretically in [54, 56] and observed experimentally in [57, 115]. This issue will be discussed in more detail in Ch. 5, where the avalanche stage of the off-resonant excitation of Rydberg atoms will be studied under highly dissipative conditions.

Chapter 5

Full counting statistics analysis and phase diagram of a strongly dissipative Rydberg gas

In Ch. 4 we introduced the three different stages of the off-resonant excitation of Rydberg atoms: ignition, facilitation and avalanche. The first two were discussed in detail in the previous chapter. Here we focus our attention on the latter one, the avalanche stage. For this regime and in presence of dissipation, evidences of diverse rich phenomena have been identified, like intermittency and/or coexistence of quantum phases [54, 56], or bistability [115]. By analyzing the full counting statistics of the excitation events we will show the signatures of those phenomena we found in a Rydberg cold gas in the dissipative regime.

Hence, a brief description of the Ising model, used to the theoretical description of our system, will be given in Ch. 5.1. Some specifications about the open Ising models and how dissipation affects those systems, as well as the model developed in [54] will be summarized in Ch. 5.1.1, in order to highlight the main points that will be useful for our analysis. In Ch. 5.2 we will present our experimental results on the generation of Rydberg excitations off resonance under high dissipative conditions and the analysis of the full counting distributions.

5.1 Quantum Ising model

In order to describe the quantum Ising model we consider spins 1/2 on a lattice. The Hamiltonian [116] of the model is given by:

$$H = -(g\sum_{j}\hat{S}_{x}^{j} + J\sum_{j,k}\hat{S}_{z}^{j}\hat{S}_{z}^{k}) \tag{5.1}$$

where $\hat{S}_{x,y,z}^{j}$ correspond to the spin-1/2 matrices at the lattice site j:

$$\hat{S}_x = \frac{1}{2}\begin{pmatrix} 0 & 1 \\ 1 & 0 \end{pmatrix};\ \hat{S}_y = \frac{1}{2}\begin{pmatrix} 0 & -i \\ i & 0 \end{pmatrix};\ \hat{S}_z = \frac{1}{2}\begin{pmatrix} 1 & 0 \\ 0 & -1 \end{pmatrix}$$

The nearest neighbors pairs of lattice sites are $\langle j,k\rangle$, J corresponds to a coupling constant and g is the transverse coupling field. This model is known as the *transverse Ising model*, because the first term accounts for a transverse magnetic field applied perpendicular to the axis of the Ising interaction (second term of the Hamiltonian), which favors parallel alignment between the neighboring spins. Depending on the values of g and J different situations arise within this system:

- $g = 0$, $J > 0$. In this case the ground state is given by the ferromagnetic states in which all the spins take the value $S_z^j = 1$ or $S_z^j = -1$ (spin up $|\uparrow\rangle$ or spin down $|\downarrow\rangle$). Correspondingly, the ground state is doubly degenerate.

- $g > 0$, $J > 0$. As the transverse field is increased from zero, it can flip spins between $S_z^j = 1$ or $S_z^j = -1$, introducing quantum fluctuations.

- In the limit $g/J \to \infty$ or, equivalently, $J = 0$ and $g > 0$ all the spins are aligned in the x direction ($S_x = 1$) in the ground state. The ground state in this case is unique. However, although the spins are completely "ordered" in terms of S_x, the ground-state configuration appears disordered in the S_z basis.

From this emerges the qualitative different nature of the ground state of the system between the two limits $g/J = 0$ and $g/J \to \infty$. The transition from one regime to the other predicts an abrupt change in the ground state of a many-body system due to its quantum fluctuations. This is used to argue the existence of a phase transition between the two limiting cases, that occurs at a critical point. In order to find it, the exact solution of the $1D$ Ising model in a transverse field can be found using the Jordan-Wigner transformation [117, 118]. From this solution, it is possible to define two phases: an ordered phase with $g < g_c$; and a disordered phase with $g > g_c$. The critical point: $g_c = g = J$ evidences a second order phase transition at a critical value of the transverse field. Thus, the quantum phase transitions (QPTs) arise as a result of competing interactions in a quantum many-body system.

For higher-dimensional systems, there is no exact analytical solution of the problem. However a sharp phase transition between the ordered and the disordered phases can be numerically found. [119, 120]

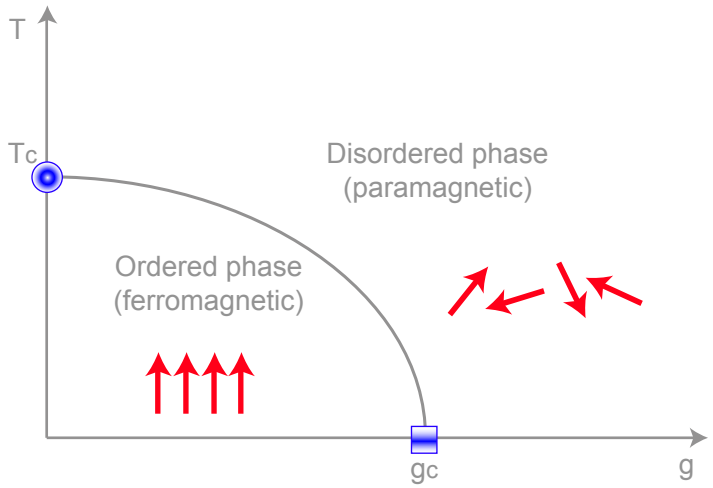

Figure 5.1: Schematic of the 2-dimensional quantum Ising model phase diagram. The square denote a quantum phase transition (at $g_c = 0, T$) and the cricle a thermal one (at $g = 0, T_c$) . Figure taken from [**?**].

Fig. 5.1 shows the phase diagram for the two-dimensional quantum Ising model in a transverse field. When $T = 0$, there is a quantum phase transition at g_c. In addition, when $g = 0$ the system becomes the two-dimensional classical Ising model which exhibits a thermal second order phase transition at $T/J = 2.2691\ldots$ so there is a quantum phase transition at $(g_c = 0, T)$ and a thermal one at $(g = 0, T_c)$. These two transitions are typically connected by a line of thermal critical points [**?**], as is shown in Fig. 5.1.

5.1.1 Dissipative quantum Ising model

The problem of dissipation in quantum systems dates back to almost thirty years ago, when macroscopic quantum tunneling and coherence in superconducting quantum interference devices (SQUIDs) were proposed [121]. Recently, the interest in the behavior of interacting atomic samples in the presence of dissipation has experienced a notable increase. Recent experiments with cold atoms study the effect of spontaneous emission, since it is an inherent characteristic of these systems. In particular, evidences of the the emergence of quantum phases and rich dynamics as a consequence of interplay between coherent and dissipative evolution have been shown [110, 35, 54, 56, 122].

In the frame of this thesis, we study the effect of dissipation in an Ising-like system, as we will see in the following pages. Theoretically, this problem has been treated [54], where the authors study the behavior of an open Ising model in a transverse magnetic field in the presence of dissipation. The system consists of N spin-1/2 particles arranged in a lattice of spacing a and coupled to a thermal bath of zero temperature. The coupling to the thermal bath is assumed to take place at the single-particle level and it is mediated by the Lindblad operators, J_ν [123], which induce sudden changes of the state of the system and, therefore, describe spontaneous emission events of quanta into the bath. In Fig. 5.2 we show a schematic representation of the open Ising model discussed in [54].

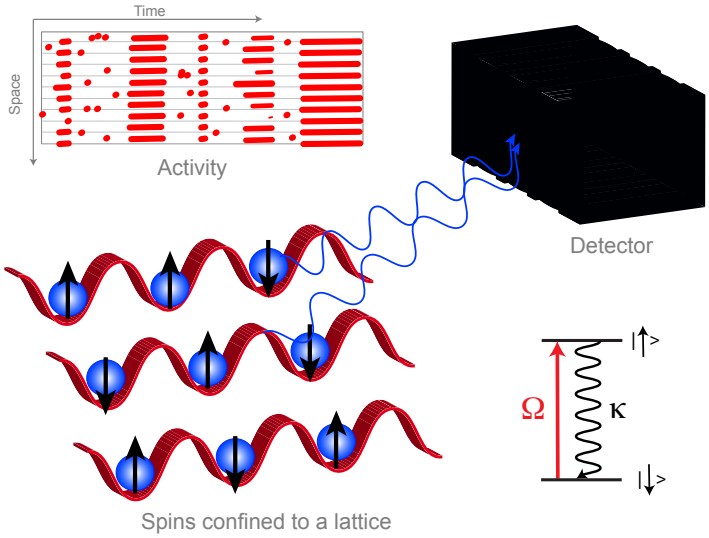

Figure 5.2: Schematic representation of the quantum Ising model in the transverse magnetic field.

Their interest relies on the statistics of these emission events and their connection to the quantum dynamics of the system. To do so, they employ the thermodynamics of trajectories approach [124], which has shown that dynamical phase behavior can be uncovered by means of an activity order parameter [125, 126, 127]. In their case, the mean emission rate of quanta from the open quantum system into its environment (events often referred to as quantum jumps [56]) has been identified as the dynamical order parameter. The activity is proportional to the magnetization, the parameter that defines a phase transition in the traditional quantum Ising model. By studying the behavior of the system as a function of this parameter, they observed two dynamical phases: an active (whose trajectories are dense in quantum jumps and characterized by a large activity parameter) and an inactive one (where quantum jumps rarely occur and that shows small values of the activity

parameter). In the middle of the two, there is a discontinuity region which indicates a phase transition of first order between the active and the inactive phases. As we will see experimentally in the following sections, the analysis of the histograms of the activity reveals that for certain combinations of parameters, the distributions show bimodality, one peak will correspond to the active phase and the other to the inactive one. These results will be used to interpret our experimental observations.

5.2 Full Counting Statistics and phase diagram of a strongly dissipative Rydberg gas

As it was explained in Ch. 2, the information contained in the full counting distribution and the analysis of higher statistical moments provides more insight into the properties of our system. Indeed, a comparison of the counting distributions for different durations (Fig.5.3), in which the Rabi frequency was adjusted in order to keep the mean value constant, confirms that the distributions become more strongly bimodal for longer excitation durations, as has been previously shown inf Fig. 4.9. This is confirmed by the increase in the bimodality parameter with excitation duration (inset of Fig.5.3). Moreover, it has been theoretically predicted that dissipation favors the appearance of bimodality [54, 55, 56].

As we have already seen in Fig. 4.13 the excitation of Rydberg atoms on resonance and off-resonance exhibit strong qualitative differences that become evident in the shape of the histograms of the counting distributions. This effect is also visible under strong dissipative conditions. Figs.5.4(a) and 5.4(b) show the off- and on-resonant counting distributions, respectively, for two mean values ($< N >= 6$ (dashed lines) and $< N >= 23$ (solid lines)), indicated by the arrows in the inset of (a), which shows the mean number of Rydberg excitations as a function of the Rabi frequency. These distributions illustrate that also under strongly dissipative conditions, the distribution exhibits a bimodal character for off-resonant excitation; whereas the distribution on resonance is clearly sub-Poissonian.

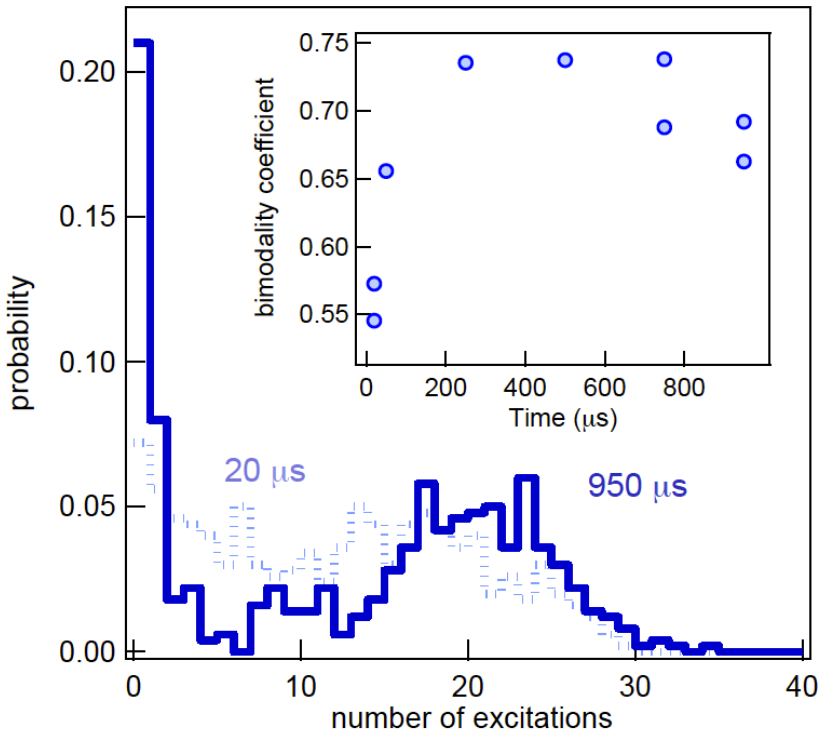

Figure 5.3: Experimental results showing the crossover to the dissipative regime. The detuning was $\delta/2\pi = +11.5$MHz and Rabi frequency was adjusted in order to keep the mean value constant. As the duration of the excitation is increased from $20\,\mu$s (dashed line) to $950\,\mu$s (solid line), the counting distributions become more strongly bimodal. The inset shows the bimodality parameter as a function of the excitation duration.

Our experimental results are compared to three simple models in order to highlight the main features of the dependence of the various quantities on the mean, $\bar{x}$. For the resonant case, we use a perfectly monomodal model (green dashed line inFig.5.4(b)), with mean $\bar{x}$ and central moments $(\mu_{2,3,4,...})_{obs} = 0$ (the detection efficiency η has been included here, as indicated by the subindex "obs", see Ch. 2); and a Poissonian monomodal model, with mean $\bar{x}$ and central moments $\mu_2 = \mu_3 = \bar{x}$, and $\mu_4 = \bar{x}(1 + 3\bar{x})$ (continuous grey line inFig.5.4(b)).

For the data off-resonance, we use again the Poissonian model (continuous grey line inFig.5.4(a)); and as a bimodal model, similar to the one we have already used in Ch.4.2.2, with two excitation modes at x_1 and x_2, probabilities $1 - \alpha$ and α, respectively, and having mean $\bar{x} = (1 - \alpha)x_1 + \alpha x_2$ and central moments $\mu_n = (1 - \alpha)(x_1 - \bar{x})^n + \alpha(x_2 - \bar{x})^n$ (red dashed line inFig.5.4(b)). The differences between both excitation regimes can be clearly seen by analyzing the second, third and fourth central moments of the dis-

tribution ($\mu_{2,3,4}$) as well as their associated normalized quantities, like the Mandel Q parameter, the skewness, the binder cumulant or the bimodality coefficient.

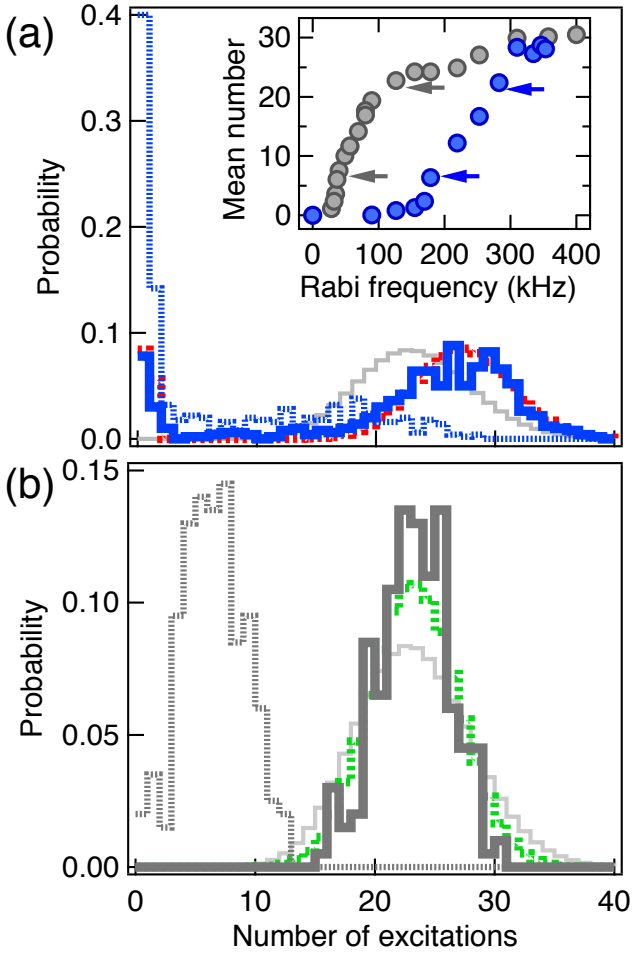

Figure 5.4: (a) Off-resonant ($\delta/2\pi = +11.5\,\mathrm{MHz}$) and (b) resonant counting distributions, for equal mean numbers 6 (dashed lines) and 23 (solid lines), respectively (indicated by the arrows in the inset of (a)), which shows the mean number of Rydberg excitations as a function of the Rabi frequency). The dotted lines are the results of the bimodal model in (a) (in red color) and of the perfectly monomodal model in (b) (in green color), whereas the solid light gray lines show the distributions expected for Poissonian distribution with the same mean values.

We report this analysis in Fig.5.5.The lines in graphs (a-f) are obtained from the simple theoretical models explained above: the bimodal model (blue

dashed line), with $x_1 = 1$ and $x_2 = 65$ Rydberg excitations; the Poissonian model (grey dotted line); and the monomodal model (grey dot-dashed line). In these calculations, the detection efficiency of $\eta \approx 40\%$ was taken into account. For the bimodal model case, the theoretical values were scaled by a factor of ≈ 0.5 in order to facilitate a qualitative comparison with the experimental data. The interaction volume is $3.6 \cdot 10^{-6}\,\mathrm{cm}^3$, the density $1 \cdot 10^{11}\,\mathrm{cm}^{-3}$ and the duration of teh excitation $\tau_{exc} = 950\,\mu\mathrm{s}$.

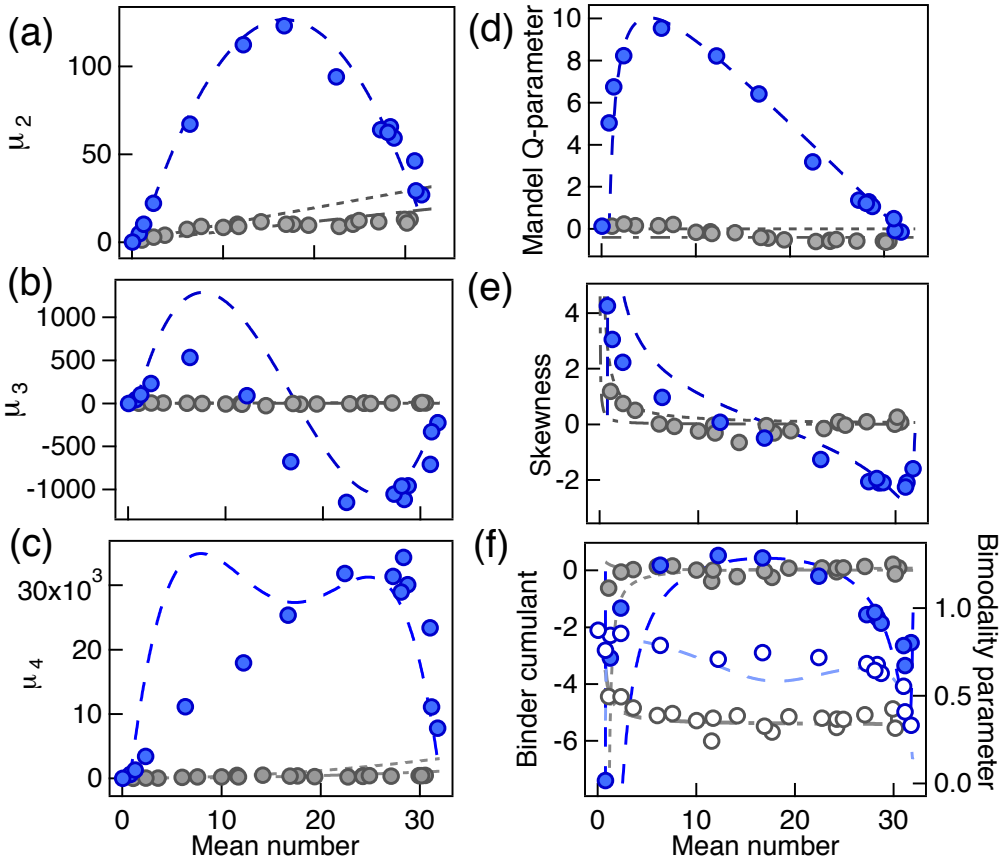

Figure 5.5: (a-c) The second, third and fourth central moments of the off-resonant (blue points) and on-resonant (gray points) counting distributions. (a-f) show the associated normalized quantities: Mandel Q-factor, skewness, and Binder cumulant as well as the bimodality coefficient. The lines in graphs (a-f) are the results of the simple bimodal (dashed), with $x_1 = 1$ and $x_2 = 65$ Rydberg excitations, Poissonian monomodal (grey dotted) and perfectly monomodal (grey dot-dashed) models described in the text.

For the case of μ_2 and the Mandel Q-factor dependence on the mean number, on resonance we see that those quantities are consistent with Pois-

sonian distributions (grey dotted lines) for small mean numbers but become increasingly sub-Poissonian for larger numbers as the system enters the fully blockaded regime. By contrast, in the off-resonant case μ_2 initially *increases* with the mean, reaching a peak at about half the maximum number of excitations (the Mandel Q-factor has a maximum at smaller mean numbers due to its normalization). As can be seen in Fig.5.5(a-f), the results of the off-resonant case are in qualitative agreement with a simple bimodal model (blue dashed line). In particular, the bimodality coefficient (Fig.5.5(f)) of the off-resonant counting distributions is consistently higher $(0.7 - 0.8)$ than for the resonant case (~ 0.4), emphasizing the qualitative difference between the two regimes. However, it is also obvious, that while the agreement is excellent for μ_2, it is less good for the higher central moments. This demonstrates the usefulness of the full counting statistics, which allows comparisons with theoretical predictions that are far more sensitive than the mean and standard deviation alone.

The results shown in Fig.5.3 can also be interpreted in terms of a dynamical phase transition between a paramagnetic and an antiferromagnetic phase in a dissipative Ising model with a transverse field, as shown recently in [54, 56]. Based on [54], where the authors propose a way to realize experimentally the quantum dissipative Ising model using Rydberg atoms, in Fig.5.6 we show a phase diagram for our system as a function of the Rabi frequency and the detuning. Although in [54] (and also in [56]) the atoms are assumed to be arranged in a crystalline structure, the distance-selective resonance mechanism described above means that in our experiment the Rydberg excitations should arrange themselves in a regular array with a spacing that depends on the detuning [73]. In our observations, the mean Rydberg number as a function of the Rabi frequency exhibits a smooth crossover between 0 excitations and a maximum number of around 30 excitations (see also Fig.5.5(a)), where the position of the crossover depends on the detuning. This is expected from the analogy with an Ising spin system [46], where the critical value of the transverse field (which corresponds to the Rabi frequency in our system) increases with increasing Ising interaction (the detuning in our case). Moreover, the distinct increase in the Mandel Q-factor in the transition region is compatible with the intermittent behavior of the system theoretically predicted in [54, 56] (as evidenced by the bimodal counting statistics in that region) due to the coexistence of active and inactive phases. In order to prove that interpretation directly, however, it will be necessary to observe the time evolution of a single experimental realization, e.g., through the observation of photons emitted during the decay process, [115]. Together with other recent experimental results [110, 57, 115], our work has inspired several theoretical investigations in the field [122, 111, 128, 129, 130, 131]. In

[131], the authors make use of a variational principle, described in [130], to study the non-equilibrium steady states of dissipative quantum many-body systems.

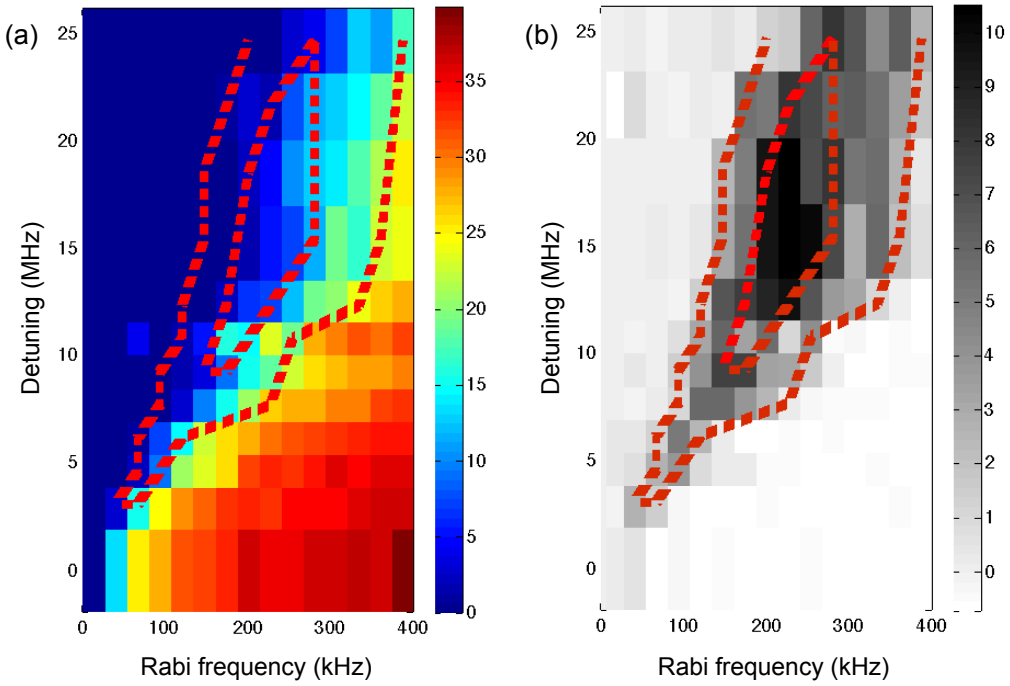

Figure 5.6: Phase diagram in the dissipative regime. (a) shows the mean number of Rydberg excitations and (b) the Mandel Q-factor as a function of Rabi frequency and detuning. In (a) and (b) the red dashed lines indicate the transition to $Q > 1$ and to $Q > 7$. The interaction volume is $3 \times 10^{-7}\,\mathrm{cm}^{-3}$ and the density $1.6 \times 10^{11}\,\mathrm{cm}^{-3}$.

The authors simulate the stationary state of a dissipative Rydberg gas using the parameters of the experiment shown in Fig. 5.6, obtaining a very good agreement between the theoretical and the experimental phase diagrams. However, their interpretation differs from the one given in [54]; where the authors refer to a phase diagram evidencing the existing of two-dynamical phases and a coexistence region. In [131] the authors interpret their results as a first-order first transition between a low-density gas and a high density liquid, ending in a critical point whose absence in our resultsmight be due to experimental limitations related to the Rabi frequency and the dephasing rate. Considering these new interpretations, it is clear that further theoretical and experimental investigations are required in order determine the exact nature of the observed transition.

5.3 Summary and perspectives

In this Chapter we continued the investigations started in Ch. 4, focusing on the avalanche stage of the off-resonant excitation. By increasing the role that dissipation plays in the excitation dynamics of such systems, a different picture compared to the one described in Ch. 4 emerges. Strong correlations within the sample emerge and become visible through super-Poissonian counting distributions ($Q > 0$). Besides, for off-resonant excitation it was predicted that this highly correlated many-body state systems show intermittency and multimodal counting distributions. We found that some of these features are clearly observable in our experiments. By analyzing the full counting statistics of our measurements, we realized that it contains much more information of the behavior of our system than what we can extract from mean or standard deviation, typically measured in experiments like ours. We found strongly bimodal probability distributions, which can be compatible with intermittency or the coexistence of dynamical phases [54, 56]. Recent publications interpreted our results as a signs of a first-order phase transitionin [131], which leaves for now, this problem as a still open question. Further experiments and theoretical analysis of the dissipative open quantum systems will be needed to shed light on those interpretations.

More generally, our analysis technique should be useful for the characterization of Rydberg excitations in optical lattices , in which, e.g., the Ising model can be realized, and in experiments with chirped excitation lasers aimed at the adiabatic creation of Rydberg crystals [17, 18, 132]. More generally, the full counting statistics will be an important tool for unveiling many-body effects in Rydberg excitations [35, 110].

Chapter 6

Spin models with Rydberg atoms. Characterization of Rydberg-Rydberg interactions

Spin hamiltonian models have been used to study a wide range of strongly interacting systems present in nature, from quantum magnetism [133], to the coherent energy transfer in quantum systems [134], and photochemistry or photosynthesis [135]. However, the complexity of those systems makes it difficult to get exact analytical solutions for many interacting spins, and even on powerful computers exact numerical solutions can only be found for the simplest cases. For that reason it has recently been suggested to use fully controllable laboratory systems to implement these models.

Rydberg atoms have been proposed as candidates to realize spin models to explore the physics of strongly correlated systems. As described in Ch. 1, Rydberg atoms interact via dipole-dipole potentials, which are many orders of magnitude stronger than all other interactions between neutral atoms or molecules. As an example, with the atomic ground state and the Rydberg state defining an effective spin-1/2, it is possible to describe the many-body dynamics in terms of a model of interacting spins [1, 136, 137]. Besides, they also provide a platform for the exploration of nonequilibrium phase transitions created by the competition between coherent and dissipative dynamics within an open system [138].

The study of the effects of Rydberg-Rydberg interactions in the dynamics of these systems is the common denominator among the chapters of this thesis. Up to this point we have focused our investigations on systems described by Ising-type Hamiltonians [16, 17, 19, 139, 140]. Additionally, the experiments presented up to this point are perfomed in the incoherent dynamics regime and exhibit interaction potentials of van-der-Waals type ($V_{vdw} \sim 1/r^6$).

Here, we present the investigations done during a 4-month period in the "Physikalisches Institut" of the University of Heidelberg (Germany) under the supervision of Prof. Matthias Weidemüller, in the frame of a Thesis cotutelle between the University of Pisa and the University of Heidelberg. During this period I was involved in studying the role of the dipole-dipole interactions in Rydberg systems (with a dipole-dipole potential, $V_{dd} \sim 1/r^3$), which can be described by a Heisenberg XX - type Hamiltonian. This analysis allows us to reproduce the dipolar exchange process between, for instance, S and P Rydberg states. By exploring the different regimes of the interaction, we are able to identify different degrees of correlation within the system as well as to get a better understanding of the energy exchange process. Furthermore, these results also served to characterize a new component of the experimental setup, a microwave pulse generator used to excite atoms to the P-Rydberg states.

6.1 Description of the problem and general working of the program

The main purpose of the work presented here was to study the dipolar population exchange between S and P Rydberg states excited using a microwave system. In Ch.2 we described the two-photon excitation technique which allows to excite cold atoms from the ground state to S and D Rydberg states. The excitation to P states, by contrast, requires the absorption of an additional photon, which can be done by using a microwave source. Those experiments served to measure the dipole-dipole interaction strength independently and set the basis for the study of energy transport experiments with direct $S - P$ exchange.

A recent work reports on the the investigation of the dipole-mediated transport of Rydberg excitations using an interaction enhanced imaging method [141] (a similar method has been proposed also in [142]). This method consists of exciting some atoms to the Rydberg state (*impurities*) embedded in a bath of ground state atoms which could be rendered transparent by realizing an electromagnetically induced transparency (EIT) scheme [143], making use of an additional Rydberg state (*probe* atoms). In a three-level systems consisting of two long-lived states ($|g\rangle$, $|r\rangle$) and one rapidly decaying level ($|e\rangle$), coherently coupled by two laser fields, named probe (Ω_p) and coupling (Ω_c, see Fig. 6.1) EIT can occur in a narrow spectral range. In EIT, the two light fields interfere destructively, in a way that presence of a strong coupling field changes the optical properties of the sample respect to the weak probe field, rendering an otherwise strongly absorbing medium, into a transparent one. A simple sketch of the EIT scheme is represented in

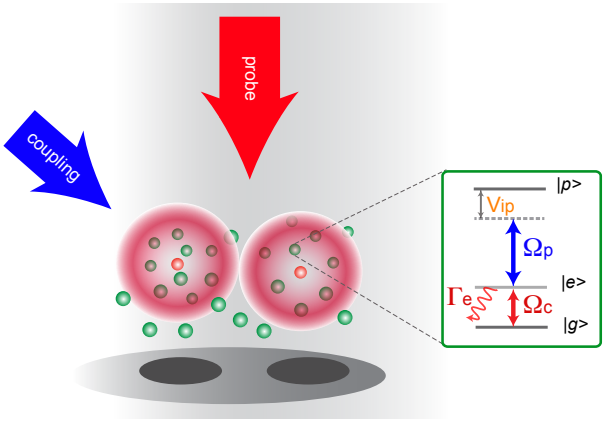

Figure 6.1: Mechanism of the enhanced imaging technique. The impurities (indicated as orange spheres) interact with the Rydberg states of the surrounding bath of probe atoms (green spheres) within a radius R_{ip}. The interactions, of strength V_{ip}, shift the Rydberg levels of the probe atoms breaking the EIT condition. As a consequence the atoms in the vicinity of an impurity are rendered absorbing.

Fig. 6.1. The imaging is done by mapping the properties of the impurities Rydberg state onto a strong optical transition using EIT and taking advantage of the fact that the impurity-probe interactions enhance the signature of the former ones. First, the atoms that will be imaged (the impurities) are excited to the Rydberg state $|i\rangle$ (orange spheres in Fig. 6.1).The impurities are embedded in a bath of ground state atoms which are made transparent by realizing an EIT system involving a probe Rydberg state, $|p\rangle$. The impurity Rydberg atom shifts the Rydberg states of the surrounding atoms thereby introducing an effective detuning of the coupling field. This effective detuning is given by the interaction energy between the impurity and the probe atom, V_{ip}, and depends on their spatial separation d.

A way to increase the enhancement of this imaging system consisted in using a Förster resonance, which allows one to maximize the impurity-probe interactions. On or close to a Förster resonance the impurities and probe atoms interact via dipolar exchange: $V_{ip}(r) = V_{dd}(r) = C_3/r^3$ [144, 145], leading to a coherent excitation transfer of the impurity to a probe atom. In [141] the authors report on the observation of the dipole-mediated energy transport dynamics of Rydberg atoms as well as the way used to control these dynamics by tuning the interactions and the coupling to the environment.

The energy transport phenomenon is not new, in fact, it has been extensively studied, specially in biological systems [135, 146, 147]. In this context, some theoretical publications predict an optimal efficiency of this transport for dephasing rates which are on the order of the coherent couplings [148, 149].

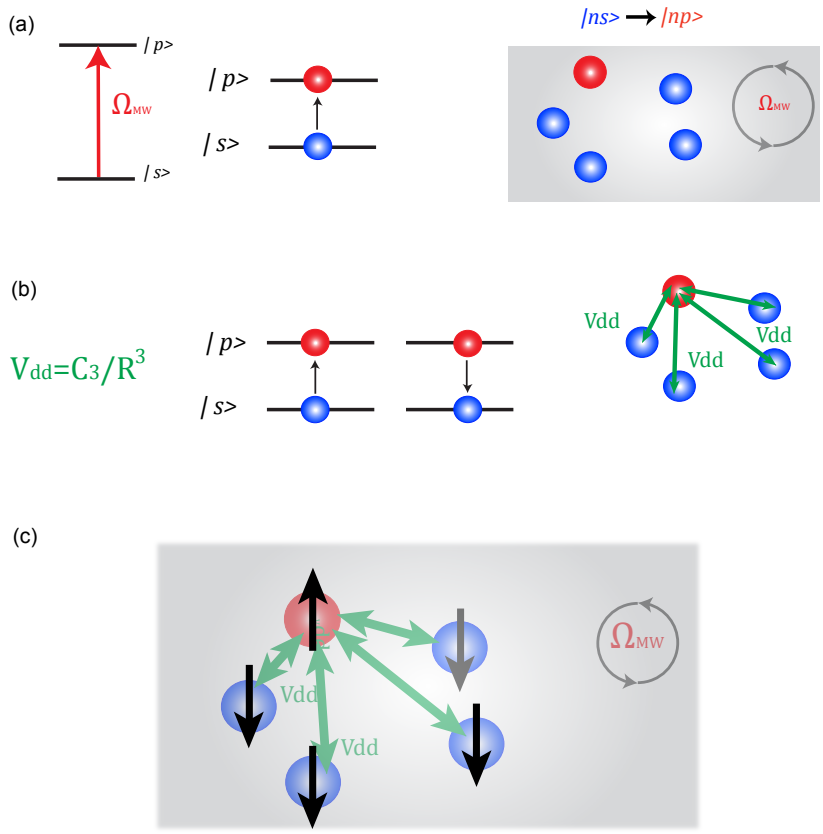

Figure 6.2: Illustration of the excitation to P Rydberg states by a microwave coupling field and dipolar exchange process. (a) Once a $P-$Rydberg excitation is generated in the system by means of the microwave coupling, the dipole-dipole interaction between it and the other $S-$ Rydberg atoms lead to an exchange of energy between the two states. (b) The dynamics, (c), is the sum of the contributions of the microwave coupling and the dipolar exchange.

The large dipole moments of Rydberg atoms renders them the perfect candidates to study the dipolar energy transfer. These experiments can be realized similarly to those of [141], using Rydberg P states as impurities in order to restrict the transport channels to $|nS, nP\rangle \rightarrow |nP, nS\rangle$.

To investigate this problem theoretically, we first solved numerically the evolution in time of a system of $N \leq 7$ atoms, which are already in an S-Rydberg state. Neither the excitation to the S-state nor the effects of the interactions among the remaining ground state atoms are included in the simulations. In our case, atoms are initially in the $|48S_{1/2}\rangle$ state. This ensemble is then irradiated by a microwave field of frequency $\sim 6\,\mathrm{GHz}$ and Rabi frequency Ω_{MW}, such that one atom is excited to the $|48P\rangle$ state. By making these simplifications, the coupling of atom in the $|48S_{1/2}\rangle$ level to the $|48P_{1/2}\rangle$ level can be treated as a two-level system. Fig. 6.2 (a) illustrates this process.

The microwave field irradiates the sample and, once a $P-$Rydberg excitation is generated in the system, Fig. 6.2 (a), the dipole-dipole interaction between it and the other $S-$Rydberg atoms becomes manifest leading to an exchange of energy between the two states, Fig. 6.2 (b). Considering the interaction of the impurity with each one of the probe atoms separately, two Rydberg atoms in the positions j^{th}, k^{th} interact with:

$$\hat{V}_{dd} = \frac{C_3}{|r_j - r_k|^3} \tag{6.1}$$

Hence, the total process will be the sum of the contributions both from the coupling and the dipole-dipole exchange, as can be seen in Fig. 6.2(c)

This system can be described in terms of a Heisenberg XX Hamiltonian that reads:

$$\hat{H} = \frac{\Delta}{2}\sum_{j}^{N}\hat{S}_z^{(j)} + \sum_{j=1}^{N}\Omega_{MW}\cdot\hat{S}_x^{(j)} + \sum_{j=1}^{N}\sum_{k=1,k\neq j}^{N} V_{dd}(\hat{S}_+^{(j)}\cdot\hat{S}_-^{(k)} + \hat{S}_-^{(j)}\cdot\hat{S}_+^{(k)}) \tag{6.2}$$

where: Ω_{MW} is the microwave Rabi frequency, Δ is the detuning and $r_{j,k}$ are the positions of the j^{th}, k^{th} atoms respectively.

As building blocks for the Hamiltonian we use the 1/2-Spin matrices:

$$\hat{S}_x = \frac{1}{2}\begin{pmatrix} 0 & 1 \\ 1 & 0 \end{pmatrix};\ \hat{S}_y = \frac{1}{2}\begin{pmatrix} 0 & -i \\ i & 0 \end{pmatrix};\ \hat{S}_z = \frac{1}{2}\begin{pmatrix} 1 & 0 \\ 0 & -1 \end{pmatrix}$$

From these matrices we define the raising and lowering operators for site j as:

$$\hat{S}_{\pm}^{(j)} = (\hat{S}_x^{(j)} \pm i\hat{S}_y^{(j)}) \tag{6.3}$$

For a single atom we set the basis:

$$|s\rangle = \begin{pmatrix} 1 \\ 0 \end{pmatrix}; \;\; |p\rangle = \begin{pmatrix} 0 \\ 1 \end{pmatrix}$$

Therefore:

$$|s\rangle\langle p| = \hat{S_+}; \qquad |p\rangle\langle s| = \hat{S_-} \tag{6.4}$$

The simulations are performed using two different configurations: a $1D$ lattice, in which atoms are placed in a chain separated by a distance a; or a $3D$ spatial configuration in which atoms are placed in a sphere of radius r in random positions. Due to this, several spatial arrangements are realized and, the final result will be the average over them. Fig. 6.3 illustrates both configurations.

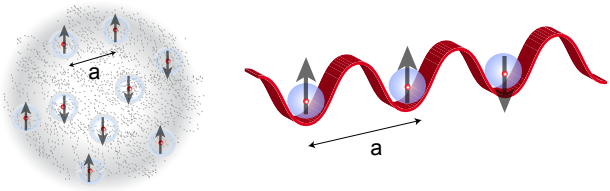

Figure 6.3: Illustration of the spatial configurations employed in our simulations. (a) $3D$ (b) $1D$

These two configurations were choosen for different reasons. While the $1D$ lattice provides an excellent context for studying the behavior of few interacting particles, or how the system size and the interactions character affect the dynamics; the $3D$ configuration offers a more realistic results that can be directly compared to experimental measurements.

6.2 Excitation dynamics in a 1D lattice

The simplest case of study is a system of two atoms coupled to the p-state with Ω_{MW} and that interact with each other through V_{dd}. For this case, at $\Delta = 0$, the Hamiltonian matrix in the $|ss, sp, ps, pp\rangle$ basis is:

$$\hat{H} = \begin{pmatrix} 0 & \frac{\hbar\cdot\Omega_{MW}}{2} & \frac{\hbar\cdot\Omega_{MW}}{2} & 0 \\ \frac{\hbar\cdot\Omega_{MW}}{2} & 0 & V_{dd} & \frac{\hbar\cdot\Omega_{MW}}{2} \\ \frac{\hbar\cdot\Omega_{MW}}{2} & V_{dd} & 0 & \frac{\hbar\cdot\Omega_{MW}}{2} \\ 0 & \frac{\hbar\cdot\Omega_{MW}}{2} & \frac{\hbar\cdot\Omega_{MW}}{2} & 0 \end{pmatrix}$$

In it, the two competing energies of this system, Ω_{MW} and V_{dd} are present. By varying the ratio between them: $U = V_{dd}/\hbar \cdot \Omega_{MW}$, we distinguish three different regimes of the dynamics:

- $U << 1$: weakly interacting regime. The Rabi frequency, Ω_{MW}, dominates the dynamics and no visible effects caused by the interactions are expected

- $U \approx 1$: competing regime. The two energies, V_{dd} and $\hbar \cdot \Omega_{MW}$ are similar, leading to the emergence of a competition between the two forces. The contribution of Ω_{MW} is constant whereas the interaction will increase with time because more atoms will contribute.

- $U >> 1$: Strongly intreacting regime. Characterized by a small contribution of $\hbar \cdot \Omega_{MW}$ and a total dynamics clearly dominated by V_{dd}.

Fig. 6.4 illustrates these regimes. In it, we show variation of the population in the p-state as a function of the rescaled time: $\tilde{t} = \tau_{exc}/\tau_{Rabi}$ for $N = 2$ atoms using the $1D$ configuration. The Rabi frequency was set to: $\Omega_{MW} = 2\pi \cdot 1.48\,\text{MHz}$ and the values of the interaction parameter were:(a) $U = 0.1$, (b)$U = 1$, (c)$U = 5$. Here and throughout the whole chapter, all the atoms are initially in the $48S$-state (thus, the population in the $48P$-state is zero).

In the weakly interacting regime, Fig. 6.4(a), the Rabi frequency dominates the total dynamics, as evidenced by the clear Rabi oscillations between the S and P-state. Beatings and revivals of the decaying oscillations are clearly visible. In Fig. 6.4(b), the Rabi frequency and the interactions have similar values. An irregular pattern on the oscillations can be appreciated due to the competition between the interaction and the Rabi frequencies. When the driving field is much weaker than the interaction strength, Fig. 6.4(c), although signatures of the Rabi oscillations due to the microwave field are still visible, the dipole-dipole interaction clearly dominates the dynamics.

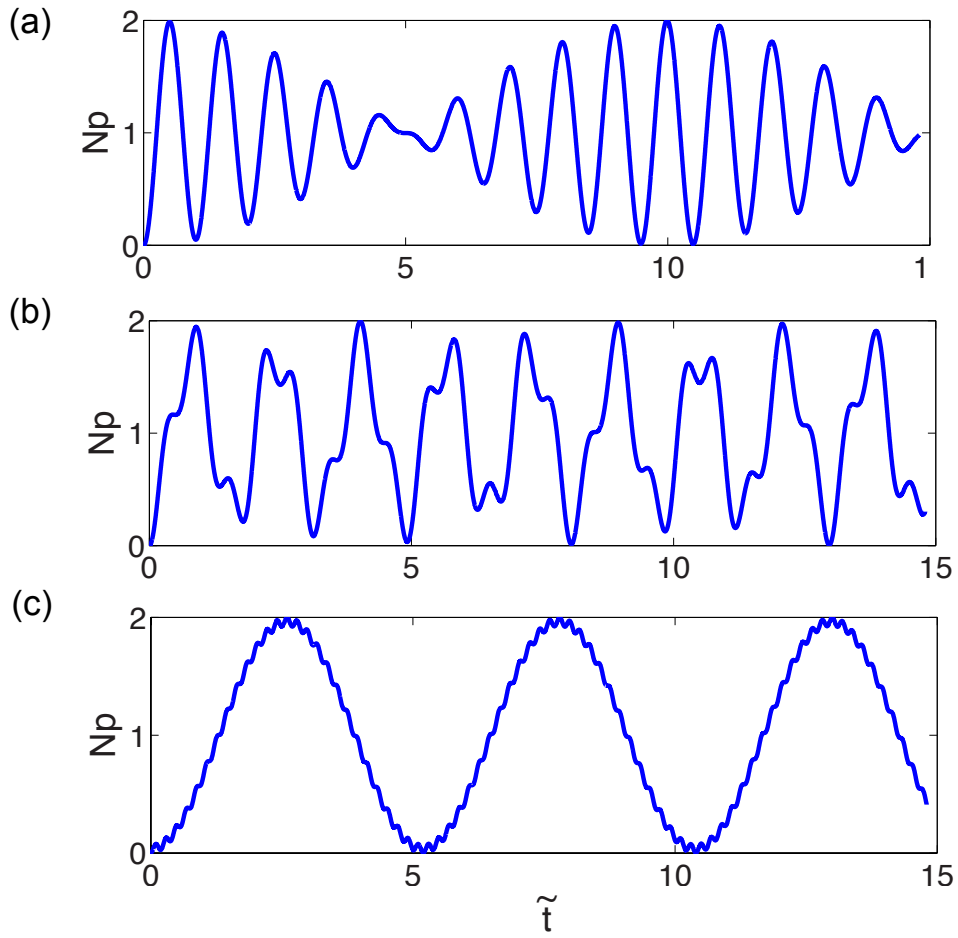

Figure 6.4: Dynamics for two atoms illustrating the different interaction regimes characterized through the dimensionless parameter $U = V_{dd}/\Omega_{MW}$: (a) $U = 0.1$, (b) $U = 1$, (c) $U = 5$. In all cases the Rabi frequency is: $\Omega_{MW} = 2\pi \cdot 1.48\,\text{MHz}$ and $N = 2$ atoms.

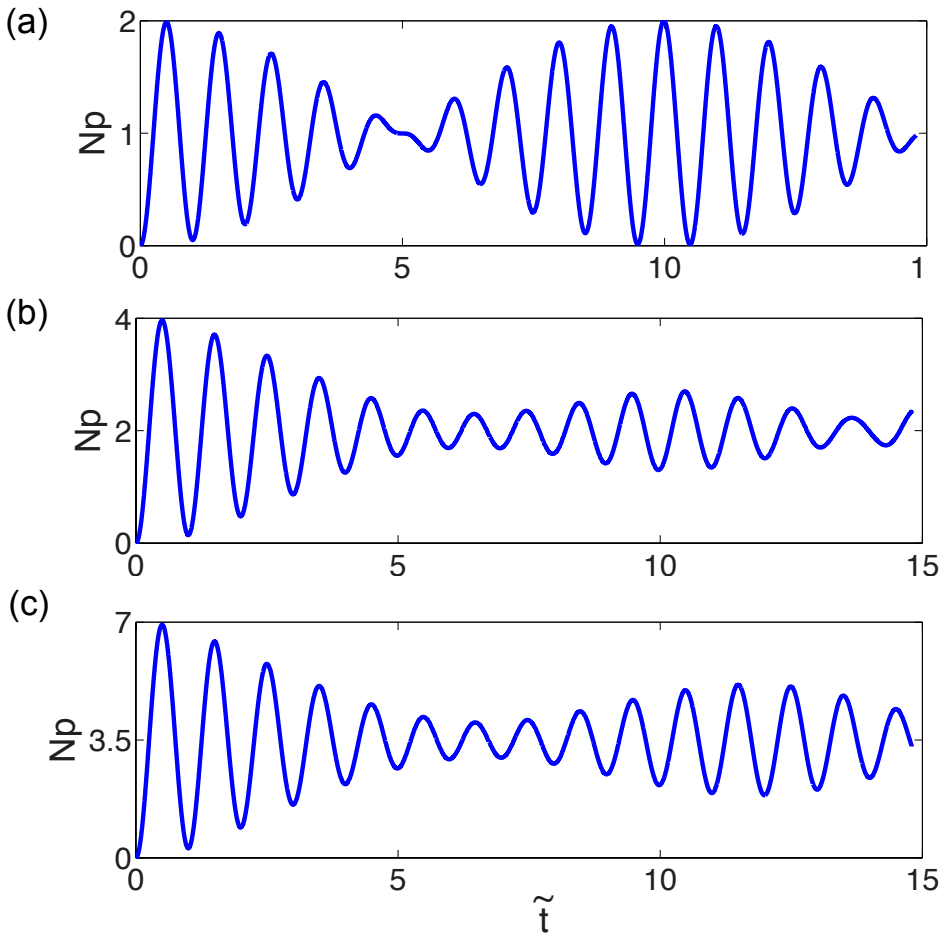

Figure 6.5: Dynamics of the Rydberg P-state population (Np) for different number of atoms: (a) $N = 2$, (b)$N = 4$, (c) $N = 7$. In all cases $\Omega = 2\pi \cdot 1.48\,\mathrm{MHz}$ and $U = 0.1$. As the number of atoms increases, more energy components are included in the Hamiltonian, which gives rise to a more pronounced damping and requires longer times for revivals in the oscillations to occur.

When more atoms are added to the system, a noticeable change in the dynamics occurs, as a consequence of the $\sim 1/r^3$ dependence of the interaction strength. Contrary to the van der Waals interaction case ($\sim 1/r^6$), where the significant contribution to the interactions is only due to the nearest neighbors; in this case also next-nearest neighbours participate in the exchange in a significant way. As a consequence, the competition between Ω_{MW} and the atomic interactions, shows a different picture where the $1/R^3$ dependence is visible. In Fig. 6.5 we compare the cases of: (a) $N = 2$ atoms, (b) $N = 4$ atoms and (c) $N = 7$ atoms.

When comparing the dynamics of $N = 4$ and $N = 7$ atoms in a lattice taking into account the interactions among all of them (Fig. 6.6 (a), (b), respectively evidenced in blue) and only with the nearest neighbors (Fig. 6.6 (b), (d), evidenced in red) the dynamics is very different. In cases (c), (d) atoms in the outermost positions of the chain interact only with each other (the ones placed in middle positions interact with two) which explains the reduction of the amplitude of the oscillations.

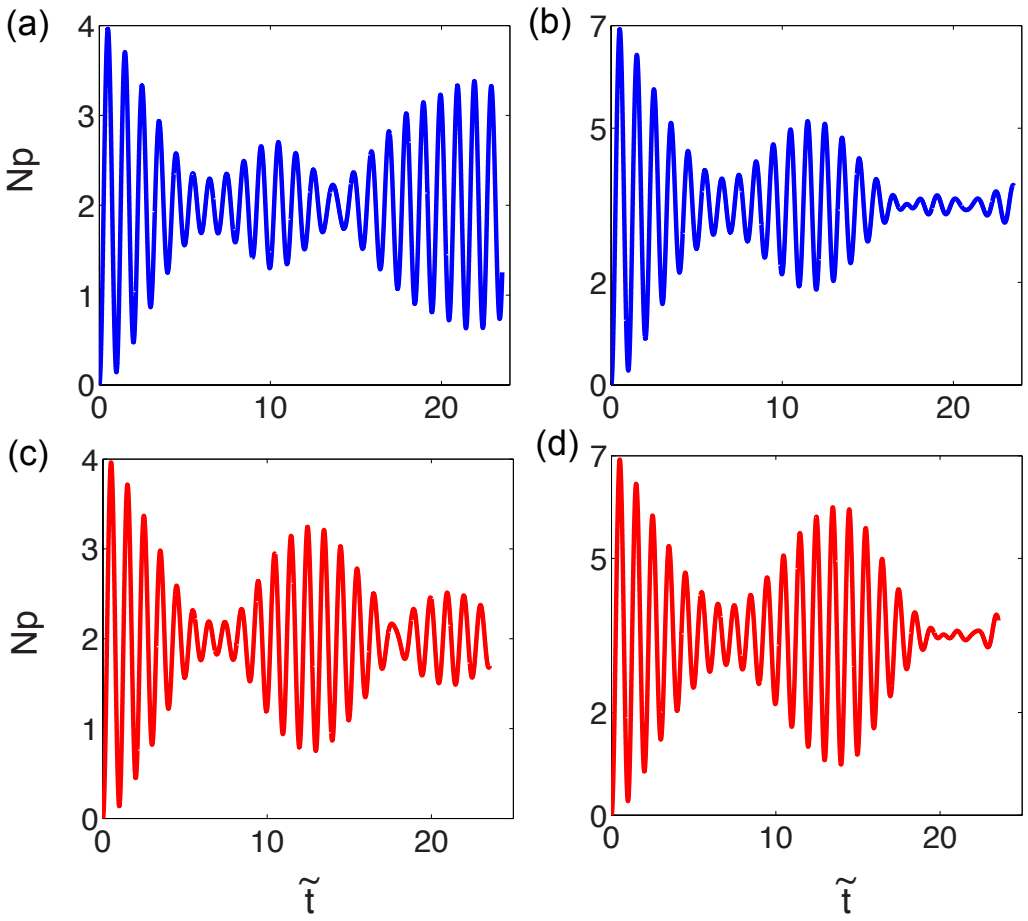

Figure 6.6: Dynamics of the Rydberg P-state population (Np) for $N = 4$ atoms (a),(c) and $N = 7$ atoms (b),(d). In all cases $\Omega = 2\pi \cdot 1.48\,\mathrm{MHz}$ and $\tilde{U} = 0.1$. In (a)-(b), the interaction is calculated taken into account all the atoms present in the lattice. In (c)-(d), only the interaction with the nearest neighbors is included.

6.3 Rydberg excitation dynamics in a 3D system and characterization of microwave Rabi oscillations

To study of the dipole-dipole interactions in the $3D$ system, N atoms are placed in a sphere with homogeneous density, $n(x)$, in random positions. In order to obtain sufficiently good statistics, the program is run 100 times and the results presented in this section correspond to the average over all the repetitions. For parameters like density or Rabi frequency values, similar values to those given in [150] were chosen, in order to reproduce the conditions of the experiments.

We start with the simplest case, i.e. the study of the dynamics for $N = 2$ atoms. In analogy to the $1D$ case, we define an dimensionless interaction parameter, $\tilde{U}$, that will be used to characterize the interaction regime: $\tilde{U} = (C_3 \cdot n_S/\hbar \cdot \Omega_{MW})$, where also three different interaction regimes (weakly, competing or strongly interacting) are defined depending on the value of $\tilde{U}$. n_S is the density of Rydberg atoms in the S state.

In Fig. 6.7 we show the dynamics for $N = 2$ atoms for different values of the $\tilde{U}$ parameter: (a) $\tilde{U} = 0.1$, $n_S = 2.84 \cdot 10^8\,\mathrm{cm}^{-3}$; (b) $\tilde{U} = 1$, $n_S = 2.84{\cdot}10^8\,\mathrm{cm}^{-3}$; (c) $\tilde{U} = 5$, $n_S = 1.42{\cdot}10^9\,\mathrm{cm}^{-3}$. In all cases the Rabi frequency was set to a typical value from the experiments [150]: $\Omega_{MW} = 2\pi \cdot 1.48\,\mathrm{MHz}$.

In the weakly interacting case, (a), the dynamics exhibits a steep slope in the first Rabi cycle ($\approx 0.68\,\mu$s) and oscillations around the stationary state for longer times. As the interactions role become more and more important (Fig. 6.7 (b) and (c), respectively), the initial slope of the curve is less pronounced (the dynamics becomes slower) and the saturated regime is reached for longer times: ~ 2 Rabi cycles ($\approx 1.35\,\mu$s) for the competitive regime and ~ 6 Rabi cycles ($\approx 4\,\mu$s) for the strongly interacting case.

When we look at higher values of N, Fig. 6.8, in the weakly interacting case ($\tilde{U} = 0.1$) for the 2 atom case we see Rabi oscillations for short values of the excitation time and for longer ones a light damping is visible. This effect is more evident for higher N values due to the fact that more atoms are contributing to the exchange process.

Similar behavior is observed when, instead of changing N, we vary the density of the sample or the Rabi frequency. Fig. 6.9 shows the dynamics of the Rydberg population of the P-state for different values of the density of the S-Rydberg excitations (from top to bottom): $n_S = 0.6 \cdot 10^7\,\mathrm{cm}^{-3}$ (green curve), $n_S = 1.0 \cdot 10^7\,\mathrm{cm}^{-3}$ (blue curve), $n_S = 5 \cdot 10^7\,\mathrm{cm}^{-3}$ (black curve) and $n_S = 2.84 \cdot 10^8\,\mathrm{cm}^{-3}$ (red curve). As parameters we use: $N = 7$ atoms and $\Omega_{MW} = 2\pi \cdot 1.48\,\mathrm{MHz}$ for the microwave Rabi frequency. These parameters were chosen with the idea of simulating the conditions described

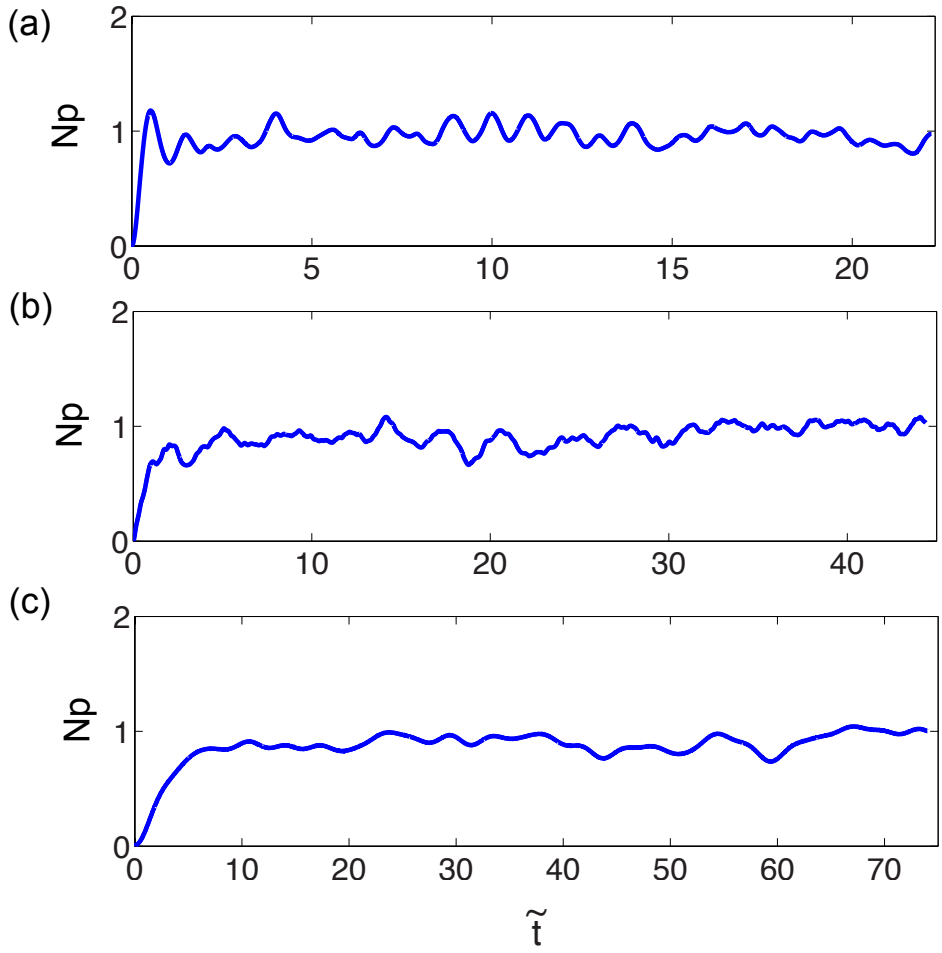

Figure 6.7: Dynamics for two atoms illustrating the different interaction regimes characterized through the adimensional parameter $\tilde{U}$: (a) $\tilde{U} = 0.1$, $n_S = 2.84 \cdot 10^8\,\mathrm{cm}^{-3}$, $a = 32.8\,\mu\mathrm{m}$; (b) $\tilde{U} = 1$, $n_S = 2.84 \cdot 10^8\,\mathrm{cm}^{-3}$, $a = 15.2\,\mu\mathrm{m}$; (c) $\tilde{U} = 5$, $n_S = 1.42 \cdot 10^9\,\mathrm{cm}^{-3}$, $a = 8.9\,\mu\mathrm{m}$. The Rabi frequency is: $\Omega_{MW} = 2\pi \cdot 1.48\,\mathrm{MHz}$.

in the experiments reported in [150].

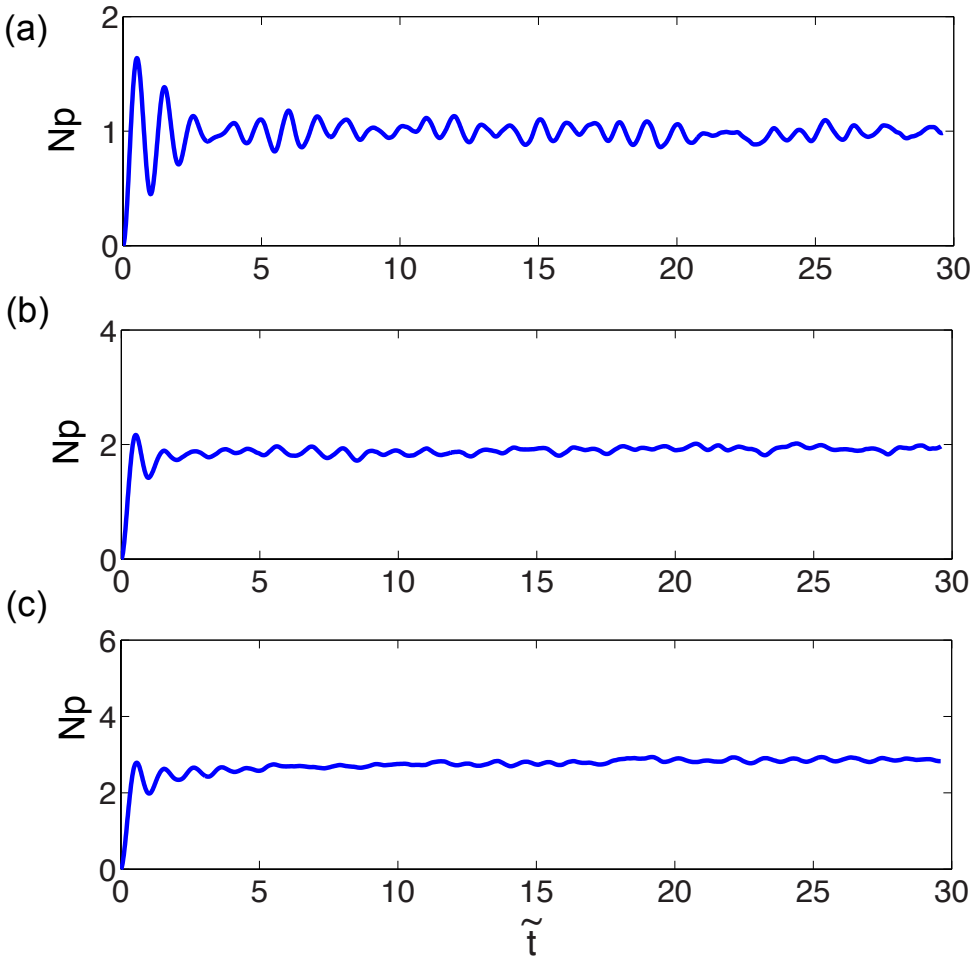

Figure 6.8: Dynamics for different values of N illustrating weakly interacting regime for: (a) $N = 2$ atoms; (b) $N = 4$ atoms; (c) $N = 6$ atoms. In all cases: $\tilde{U} = 0.1$, $\Omega_{MW} = 2\pi \cdot 1.48\,\mathrm{MHz}$ and $n_S = 2.84 \cdot 10^7\,\mathrm{cm}^{-3}$.

At low Rydberg densities (green curve), Rabi oscillations between S and P states are clearly visible with a light damping. However, the more the density increases (blue, black and red curves) the more damped out are the oscillations, as a consequence of the interaction exchange process. This explanation agrees with [151], where the authors claim that the transition from strong damping to coherent Rabi oscillations is determined by the competition between the exchange rate with the nearest-neighbors and the microwave Rabi frequency. Qualitatively, these results are in good agreement with the simulations shown in Fig. 6.7 as well as with the experiments [150], as proves Fig. 6.11.

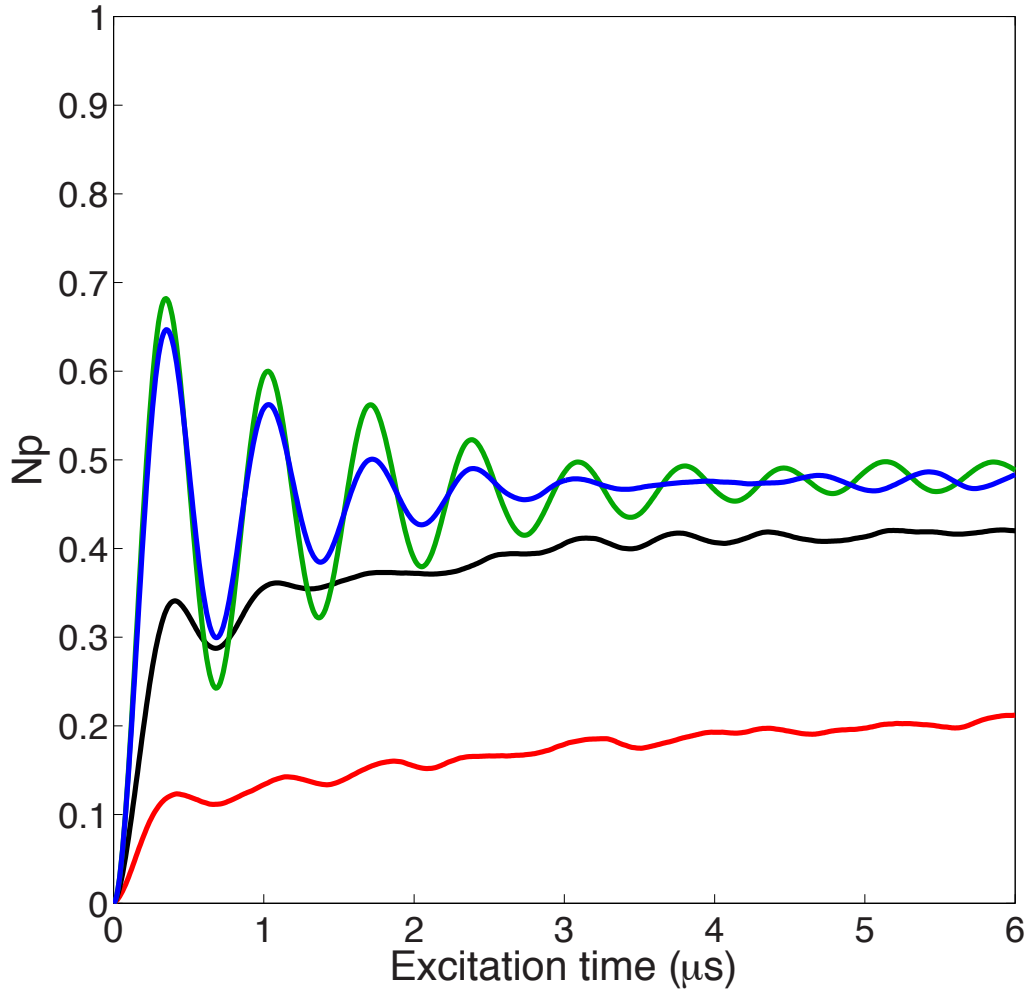

Figure 6.9: Dynamics for different values of different densities: (a) $n_S = 0.6 \cdot 10^7\,\mathrm{cm}^{-3}$, (b) $n_S = 1.0 \cdot 10^7\,\mathrm{cm}^{-3}$, (c)$n_S = 5 \cdot 10^7\,\mathrm{cm}^{-3}$ and (d)$n_S = 2.84 \cdot 10^8\,\mathrm{cm}^{-3}$. In all cases: $N = 7$ atoms and $\Omega_{MW} = 2\pi \cdot 1.48\,\mathrm{MHz}$.

In Fig. 6.10 the density of the S-Rydberg excitations was fixed to $n_S = 5.0 \cdot 10^7\,\mathrm{cm}^{-3}$ and the number of atoms to $N = 7$. The simulations were performed for different values of the Rabi frequency, in order to compare the theoretical curves of different Ω_{MW} values with the estimated value of the Rabi frequency given by the experiments: $\Omega_{MW} \approx 2\pi \cdot 1.48\,\mathrm{MHz}$ (see [150]).

Also this analysis evidences the different interaction regimes: $\tilde{U} << 1$ (red curve), $\tilde{U} \sim 1$ (blue curve) and $\tilde{U} >> 1$ (black and green curves). Thus, when the Rabi frequency is much lower than the interactions ($\tilde{U} << 1$, red curve), the dipole-dipole exchange dominates the dynamics slowing it down (in fact, the stationary state is not reached within the experimental time scale) and damping out the oscillations. Increasing the Rabi frequency up to a similar

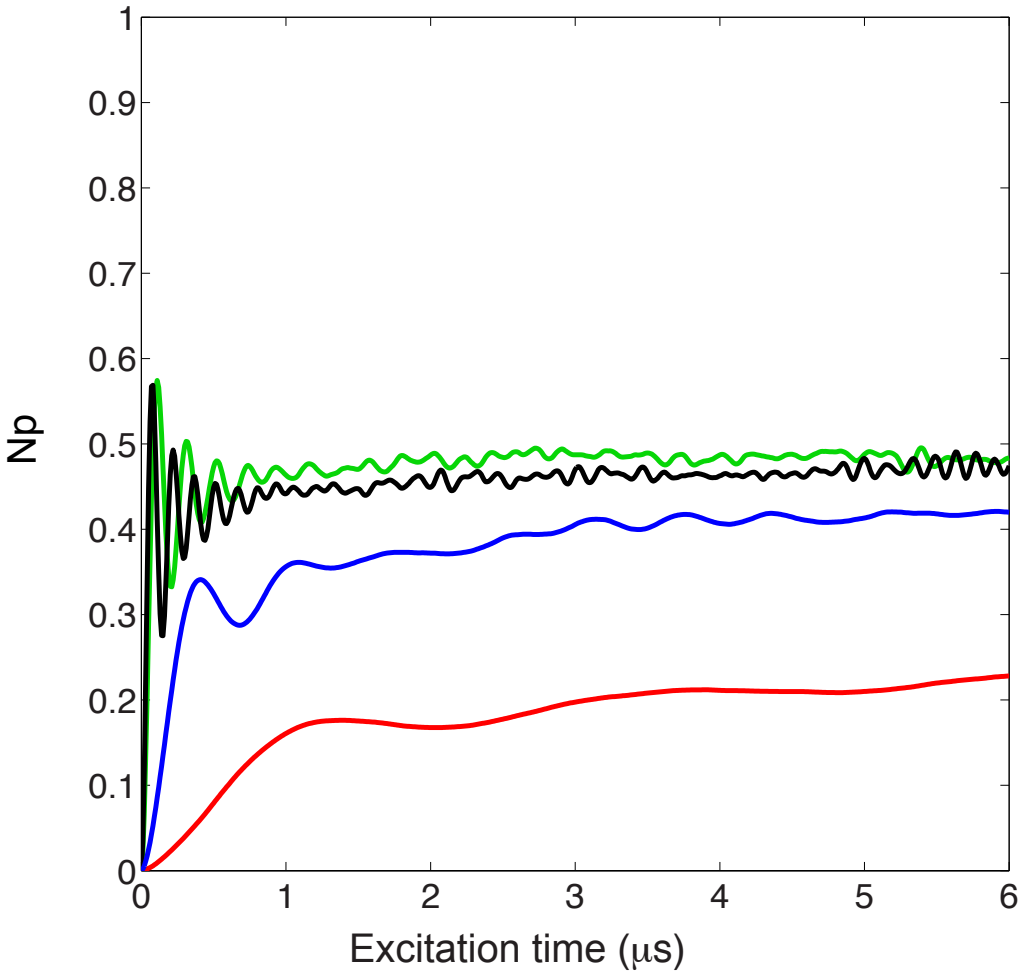

Figure 6.10: Dynamics for different values the Rabi frequency: $\Omega_{MW} = 2\pi \cdot 0.48\,\mathrm{MHz}$(red curve), $\Omega_{MW} = 2\pi \cdot 1.48\,\mathrm{MHz}$ (blue curve), $\Omega_{MW} = 2\pi \cdot 5.0\,\mathrm{MHz}$(black curve) and $\Omega_{MW} = 2\pi \cdot 7.0\,\mathrm{MHz}$ (green curve). In all cases: $N = 7$ atoms and $n_S = 5 \cdot 10^7\,\mathrm{cm}^{-3}$.

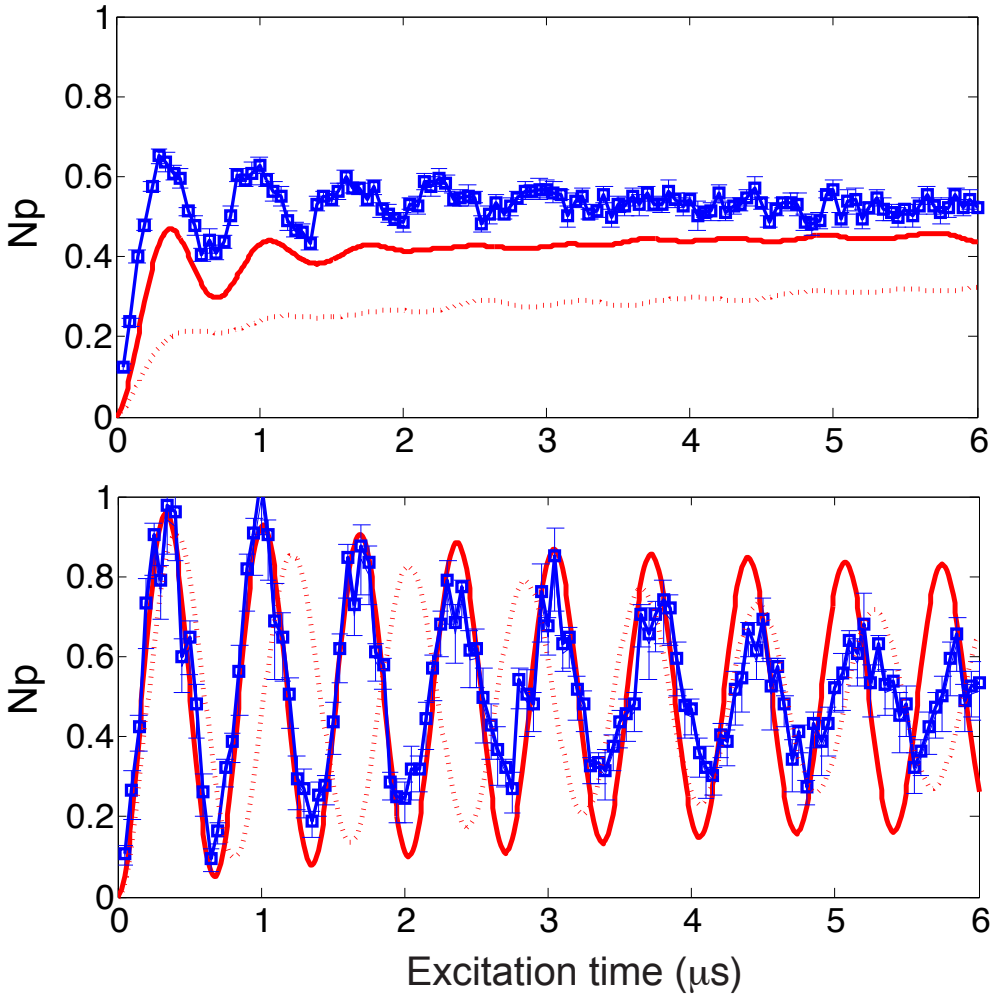

Figure 6.11: Dynamics of the population exchange between S and P states for different densities of the sample: (a) $n_S = 1.3 \cdot 10^8\,\mathrm{cm}^{-3}$ and (b) $n_S = 6.7 \cdot 10^5\,\mathrm{cm}^{-3}$. The experimental data (continuous blue line) is compared to the results of the simulations (dashed red lines). For the continuous line calculations we use an interaction coefficient value of $C_3 = 2\pi \cdot 5.2\,\mathrm{GHz}$; whereas for the continuous red lines, we set an effective value of the interaction coefficient: $C_{3_{eff}} = 2\pi \cdot (1 \pm 0.1)\,\mathrm{GHz}$.

value of the interaction strength ($\tilde{U} \sim 1$, blue curve) Rabi oscillations start to be visible at the beginning of the excitation but also a moderate damping is observed for longer times due to the interaction exchange. When Rabi frequencies are much higher than the dipole-dipole interaction (black and green curves), we get the opposite situation, the stationary state is reached very fast and Rabi oscillations are clearly visible during the whole time scale.

Finally, in Fig. 6.11 we compare the experimental results (blue curves) to the simulations (dashed red curves) for high and low densities: (a)$n_S = 1.3 \cdot 10^8\,\mathrm{cm}^{-3}$, $N_{P_{max}} \approx 270$ excitations in the P-state and (b) $n_S = 6.7 \cdot 10^5\,\mathrm{cm}^{-3}$, $N_{P_{max}} \approx 43$ excitations in the P-state (see [150] for details). In all cases, the Rabi frequency is $\Omega_{MW} = 2\pi \cdot 1.48\,\mathrm{MHz}$, and, the simulations are done with $N = 7$ atoms. For the high density case the agreement of the simulation with the experimental data is not very good, evidencing certain limitations of our model in the strongly interacting regime. This result could be improved by performing the simulations for a higher number of atoms, as shown in [150]. For the low density case, however, the agreement is much better. In order to account for the experimental details we introduce in the model an effective interaction strength that accounts for the angular dependence: $C_{3_{eff}} = 2\pi \cdot (1 \pm 0.1)\,\mathrm{GHz}$, estimated from the experimental measurements in [150]. The results of these simulations are plotted as continuous red lines. It is evident that this modification improves the results, indicating that for the exchange processes between P and S states, the orientation of the dipoles in the space must be taken into account in order to get better fits to the data and a better calibration of the setup.

6.4 Summary and perspectives

In this chapter we have investigated the dipolar exchange process between S and P Rydberg excitations. To do so, we numerically solve the evolution of a Heisenberg-XX Hamiltonian for cases in which the geometry of the sample, the density or the Rabi frequency of the coupling process are varied. We identifiy three interaction regimes dependent on which force (dipolar or coupling) dominates the dynamics. The comparison with the experimental results described in [150] exhibit a good qualitative agreement, specially when the angular dependences of the dipoles are taken into account. This is done by replacing the interaction coefficient by an effective value of the $C_{3_{eff}}$, estimated from experimental measurements, [150]. In view of these results, a way to gain more insight into the Rydberg-Rydberg interactions mechanisms would be to compare the results obtained in the present chapter to a numerical investigation of the dynamics of an Ising-type hamiltonian. In the experiments presented in this chapter we observed that increasing the

number of atoms, i.e. enhancing the exchange process, influences the dynamics of the total process. In order to link the investigations performed in the experimental setups present in Pisa and Heidelberg; an Ising-type Hamiltonian, which describes the experiment in Pisa, could be modeled in analogy to the Heisenberg XX-type Hamiltonian. By comparing the results of these simulations one could see, for instance, whether kinetic constraints appear as well in the coherent dynamics (as they do in the incoherent regime, see Ch. 3) of the Ising-like system; or if they become manifest in a system governed by a Heisenberg-XX type Hamiltonian.

Chapter 7

Conclusions and Outlook

The study of correlations emerging as a consequence of the strong interactions between Rydberg atoms in a cold gas has been the unifying subject of this thesis. To do so, two different approaches were employed, depending on which, different types and degrees of correlation (or anti-correlation) become manifest in such a system: resonant and off-resonant excitation. Both excitation regimes were reached using the same experimental setup, allowing us to study correlations or anti-correlations in a controlled many-body system depending on the selected parameters. Thus, I have studied the dynamics of an atomic system in which atoms are resonantly driven to Rydberg states under non-dissipative conditions. Here, the most striking phenomenon arising from these interactions is the dipole blockade. In this Thesis I present a method that spatially visualizes this effect. By realizing a tomography of the cold cloud, we obtain the excitation profile for Rydberg excitations and also for the ions generated from direct two-photon ionization. The comparison of these profiles evidences a modification of the shape of the Rydberg profile, which is a consequence of the suppression (blockade) of the excitation. An analysis of the counting distribution shows negative values of the Mandel-Q parameter in the high density regions as expected for a sub-Poissonian excitation process due to the Rydberg blockade. Apart from the blockade effect, by studying the incoherent dynamics of a resonantly excited Rydberg gas, we found evidences of the kinetic constraints, which lead to the exhibition of glassy features, as predicted theoretically in [30]. Experimentally, we observed that the dynamics of the system experienced a more or less pronounced slowing down depending on the interaction between the atoms of the sample.

The second approach described in this Thesis consists in Rydberg excitations off resonance, where the behavior of the system depends strongly on the detuning and the character (attractive or repulsive) of the interaction. By inserting an initial excitation acting as a seed in the sample, we managed

to start the chain reaction excitation process, that allowed us to control the dynamics of the system. Furthermore, under highly dissipative conditions novel phases and exotic phenomena have been predicted [54, 56, 57, 131]. By characterizing our system through the analysis of the full counting statistics of the excitation events, we found evidences of this phenomena as, for example, the bimodal counting distributions compatible with inermittency and/or coexistence of dynamical phases [54, 56]. All the results above mentioned were obtained studying systems that can be described by Ising-like Hamiltonians. In the last part of this Thesis I also deal with a different system, present in the Physikalisches Institut in the University of Heidelberg, described by a Heisenberg-XX type Hamiltonian which also exhibits dipole dipole interactions ($\sim 1/r^3$). I performed a theoretical investigation on the dipolar exchange process between S and P Rydberg excitations. To do so, I numerically solved the evolution according to this Hamiltonian for cases in which the geometry of the sample, the density or the Rabi frequency of the coupling process are varied. By comparing the simulations with the experimental results described in [150] we found a good qualitative agreement. Moreover, this work allowed us to do a better characterization of the experimental setup.

The experiments presented here constitute the first step in further investigations of the incoherent dynamics of Rydberg systems. In fact, some questions have been left open throughout these pages. For instance, when studying the incoherent dynamics of a resonantly excited Rydberg sample, we found evidences that neither the superatom model [90, 94, 95] nor the universal scaling laws [80] with the Rabi frequency and the number of atoms match the experimental observations. Recent studies of the superatom model in the incoherent regime [106] predict that the steady-state probability of resonantly driven Rydberg excitations, which saturates to the value 1/2 in the coherent regime, exhibits a higher saturation value in the presence of strong dephasing [152] and, in analogy to the coherent case, that the collective Rydberg excitation of superatoms increases with the atomic density. These predictions do not explain completely our observations suggesting that, away from the fully-blockaded regime, the role of the kinetic constraints is not negligible and, in fact, they dominate the dynamics. Moreover, the inhomogeneous distributions of the Rabi frequency and of the atomic density in our particular case explain why the universal scalings predicted by [80] do not agree with our observations. Hence, there is a need for further theoretical investigations of the incoherent Rydberg dynamics in which the kinetic constraints and the inhomogeneous distributions of the density and Rabi frequency are taken into account in order to get a better approximation to real systems.

Regarding the experiments performed off-resonance and under highly dis-

sipative conditions, recent publications in which our results are analyzed [131], suggest a different interpretation of our observations, explaining them as signs of a first-order phase transition. Although our work agrees well with the predictions of [54], different theoretical approaches to dissipative open quantum systems must be considered in order to analyze the discrepancies between them. Thus, while in [54] the authors employ the mean field approximation to simulate the behavior of an Ising-like system, in [131] a variational principle (described in [130]) and which includes the system correlations, was used.

On the experimental side there are additional limitations due to the inhomogeneous distribution of the density of the sample and of the Rabi frequency, which make it difficult to model the real conditions of the system. This could be improved, for instance, by employing a laser beam with a flat intensity distribution [153]. On the theoretical side, the inclusion of our experimental limitations on the models would allow a clearer interpretation of our observations.

Under non-disspative conditions, the techniques introduced in this Thesis could be used in future experiments to measure, for instance, the interaction forces between atoms generated. This could be done through time-of-flight experiments after the excitation, which should be able to detect the velocity imparted on the Rydberg atoms by the strong van-der-Waals forces.

Finally, a way to link the investigations performed in both setups, Heidelberg and Pisa could be the modeling of an Ising-type Hamiltonian which could be used to study phenomena like the manifestation of kinetic constraints both in the coherent regime of the Ising-type system or their emergence in a system governed by a Heisenberg-XX type Hamiltonian.

Bibliography

[1] R. Löw, H. Weimer, J. Nipper, J. B. Balewski, B. Butscher, H. P. Büchler, and T. Pfau, "An experimental and theoretical guide to strongly interacting Rydberg gases," *Journal of Physics B: Atomic, Molecular and Optical Physics*, vol. 45, no. 11, p. 113001, 2012.

[2] Y. Tokura and N. Nagaosa, "Orbital physics in transition-metal oxides," *Science*, vol. 288, no. 5465, p. 462, 2000.

[3] A. Garg, M. Randeria, and N. Trivedi, "Strong correlations make high-temperature superconductors robust against disorder," *Nat Phys*, vol. 4, no. 10, p. 762, 2008.

[4] G. M. Bruun, O. F. Syljuåsen, K. G. L. Pedersen, B. M. Andersen, E. Demler, and A. S. Sørensen, "Antiferromagnetic noise correlations in optical lattices," *Phys. Rev. A*, vol. 80, p. 033622, 2009.

[5] R. W. Cherng and E. Demler, "Quantum noise analysis of spin systems realized with cold atoms," *New Journal of Physics*, vol. 9, no. 1, p. 7, 2007.

[6] G. Adesso, D. Girolami, and A. Serafini, "Measuring gaussian quantum information and correlations using the rényi entropy of order 2," *Phys. Rev. Lett.*, vol. 109, p. 190502, 2012.

[7] A. Streltsov, *Quantum Correlations Beyond Entanglement and Their Role in Quantum Information Theory*. SpringerBriefs in Physics, 2015.

[8] S. Sachdev, "Quantum criticality: Competing ground states in low dimensions," *Science*, vol. 288, no. 5465, p. 475, 2000.

[9] T. F. Gallagher, *Rydberg Atoms*. Cambridge University Press, Cambridge, 1994.

[10] T. F. Gallagher and P. Pillet, "Dipole-dipole interactions of Rydberg atoms," in *Advances in Atomic, Molecular, and Optical Physics*, vol. 56

of *Advances In Atomic, Molecular, and Optical Physics*, p. 161, Academic Press, 2008.

[11] D. Jaksch, J. I. Cirac, P. Zoller, S. L. Rolston, R. Côté, and M. D. Lukin, "Fast quantum gates for neutral atoms," *Phys. Rev. Lett.*, vol. 85, p. 2208, 2000.

[12] M. D. Lukin, M. Fleischhauer, R. Cote, L. M. Duan, D. Jaksch, J. I. Cirac, and P. Zoller, "Dipole blockade and quantum information processing in mesoscopic atomic ensembles," *Phys. Rev. Lett.*, vol. 87, p. 037901, 2001.

[13] E. Urban, T. A. Johnson, T. Henage, L. Isenhower, D. D. Yavuz, T. G. Walker, , and M. Saffman, "Observation of Rydberg blockade between two atoms," *Nature Physics*, vol. 5, p. 110, 2009.

[14] A. Gaëtan, Y. Miroshnychenk, T. Wilk, A. Chotia, M. Viteau, D. Comparat, P. Pillet, A. Browaeys, and P. Grangier, "Observation of collective excitation of two individual atoms in the Rydberg blockade regime," *Nature Physics*, vol. 5, p. 115, 2009.

[15] R. Löw, H. Weimer, U. Krohn, R. Heidemann, V. Bendkowsky, B. Butscher, H. P. Büchler, and T. Pfau, "Universal scaling in a strongly interacting Rydberg gas," *Phys. Rev. A*, vol. 80, p. 033422, 2009.

[16] H. Weimer, R. Löw, T. Pfau, and H. P. Büchler, "Quantum critical behavior in strongly interacting Rydberg gases," *Phys. Rev. Lett.*, vol. 101, p. 250601, 2008.

[17] E. Pohl, T. Demler and M. D. Lukin, "Dynamical crystallization in the dipole blockade of ultracold atoms," *Phys. Rev. Lett.*, vol. 104, p. 043002, 2010.

[18] J. Schachenmayer, I. Lesanovsky, A. Micheli, and A. Daley, "Dynamical crystal creation with polar molecules or Rydberg atoms in optical lattices," *New J. Phys.*, vol. 12, p. 1030442, 2010.

[19] I. Lesanovsky, "Many-body spin interactions and the ground state of a dense Rydberg lattice gas," *Phys. Rev. Lett.*, vol. 106, p. 025301, 2011.

[20] M. Viteau, M. G. Bason, J. Radogostowicz, N. Malossi, D. Ciampini, O. Morsch, and E. Arimondo, "Rydberg excitations in Bose-Einstein Condensates in quasi-one-dimensional potentials and optical lattices," *Phys. Rev. Lett.*, vol. 107, p. 060402, 2011.

[21] P. Schauß, M. Cheneau, M. Endres, T. Fukuhara, S. Hild, A. Omran, T. Pohl, C. Gross, S. Kuhr, and I. Bloch, "Observation of spatially ordered structures in a two-dimensional Rydberg gas," *Nature*, vol. 491, p. 87, 2012.

[22] A. Schwarzkopf, R. E. Sapiro, and G. Raithel, "Imaging spatial correlations of Rydberg excitations in cold atom clouds," *Phys. Rev. Lett.*, vol. 107, p. 103001, 2011.

[23] M. Saffman, T. G. Walker, and K. Mølmer, "Quantum information with Rydberg atoms," *Rev. Mod. Phys.*, vol. 82, p. 2313, 2010.

[24] D. Comparat and P. Pillet, "Dipole blockade in a cold Rydberg atomic sample," *J. Opt. Soc. Am. B*, vol. 27, p. A208, 2010.

[25] D. Tong, S. M. Farooqi, J. Stanojevic, S. Krishnan, Y. P. Zhang, R. Côté, E. E. Eyler, and P. L. Gould, "Local blockade of Rydberg excitation in an ultracold gas," *Phys. Rev. Lett.*, vol. 93, p. 063001, 2004.

[26] K. Singer, M. Reetz-Lamour, T. Amthor, L. G. Marcassa, and M. Weidemüller, "Suppression of excitation and spectral broadening induced by interactions in a cold gas of Rydberg atoms," *Phys. Rev. Lett.*, vol. 93, p. 163001, 2004.

[27] E. Brion, K. Mølmer, and M. Saffman, "Quantum computing with collective ensembles of multilevel systems," *Phys. Rev. Lett.*, vol. 99, p. 260501, 2007.

[28] M. Müller, I. Lesanovsky, H. Weimer, H. P. Büchler, and P. Zoller, "Mesoscopic Rydberg gate based on electromagnetically induced transparency," *Phys. Rev. Lett.*, vol. 102, p. 170502, 2009.

[29] M. Viteau, P. Huillery, M. G. Bason, N. Malossi, D. Ciampini, O. Morsch, E. Arimondo, D. Comparat, and P. Pillet, "Cooperative excitation and many-body interactions in a cold Rydberg gas," *Phys. Rev. Lett.*, vol. 109, p. 053002, 2012.

[30] I. Lesanovsky and J. P. Garrahan, "Kinetic constraints, hierarchical relaxation, and onset of glassiness in strongly interacting and dissipative Rydberg gases," *Phys. Rev. Lett.*, vol. 111, p. 215305, 2013.

[31] A. Braggio, J. König, and R. Fazio, "Full Counting Statistics in strongly interacting systems: Non-markovian effects," *Phys. Rev. Lett.*, vol. 96, p. 026805, 2006.

[32] A. O. Gogolin and A. Komnik, "Full Counting Statistics for the kondo dot in the unitary limit," *Phys. Rev. Lett.*, vol. 97, p. 016602, 2006.

[33] V. M. M., H. M. D., S. C., A. E., C. D., and M. O., "Preparing cold atomic samples in different density regimes for Rydberg studies," *Journal of Physics: Conference Series*, 2015.

[34] M. M. Valado, N. Malossi, S. Scotto, D. Ciampini, E. Arimondo, and O. Morsch, "Rydberg tomography of an ultracold atomic cloud," *Phys. Rev. A*, vol. 88, p. 045401, 2013.

[35] N. Malossi, M. M. Valado, S. Scotto, P. Huillery, P. Pillet, D. Ciampini, E. Arimondo, and O. Morsch, "Full Counting Statistics and phase diagram of a dissipative Rydberg gas," *Phys. Rev. Lett.*, vol. 113, p. 023006, 2014.

[36] H. E. White, *Introduction to Atomic Spectra*. McGraw-Hill, New York, 1934.

[37] A. Dalgarno, *Rydberg states in atoms and molecules*. Cambridge University Press, Cambridge, 1983.

[38] D. G. Hummer and D. Mihalis, "The equation of state for stellar envelopes. i - an occupation probability formalism for the truncation of internal partition functions," *Astrophys. J.*, vol. 331, p. 794, 1988.

[39] V. L. Jacobs, J. Davis, and P. C. Kepple, "Enhancement of dielectronic recombination by plasma electric microfields," *Phys. Rev. Lett.*, vol. 37, p. 1390, 1976.

[40] P. P. Sorokin and J. R.Lankard, "Stimulated emission observed from an organic dye, chloro-aluminum phthalocyanine.," *IBM J. Res. Develop.*, vol. 10, p. 162, 1966.

[41] T. W. Hänsch, "Repetitively pulsed tunable dye laser for high resolution spectroscopy," *Appl. Opt.*, vol. 11, no. 4, p. 895, 1972.

[42] M. H. Anderson, J. R. Ensher, M. R. Matthews, C. E. Wieman, and E. A. Cornell, "Observation of Bose-Einstein Condensate in a dilute atomic vapor," *Science*, vol. 269, no. 5221, p. 198, 1995.

[43] K. B. Davis, M. O. Mewes, M. R. Andrews, N. J. van Druten, D. S. Durfee, D. M. Kurn, and W. Ketterle, "Bose-Einstein Condensate in a gas of sodium atoms," *Phys. Rev. Lett.*, vol. 75, p. 3969, 1995.

[44] E. A. Burt, R. W. Ghrist, C. J. Myatt, M. J. Holland, E. A. Cornell, and C. E. Wieman, "Coherence, correlations, and collisions: What one learns about Bose-Einstein Condensates from their decay," *Phys. Rev. Lett.*, vol. 79, pp. 337–340, 1997.

[45] F. Verstraete, M. M. Wolf, and J. Ignacio Cirac, "Quantum computation and quantum-state engineering driven by dissipation," *Nat Phys*, vol. 5, p. 633, 09 2009.

[46] H. Weimer, M. M. ller, I. Lesanovsky, P. Zoller, and H. Büchler, "A Rydberg quantum simulator," *Nat. Phys.*, vol. 6, p. 382, 2010.

[47] T. Keating, K. Goyal, Y.-Y. Jau, G. W. Biedermann, A. J. Landahl, and I. H. Deutsch, "Adiabatic quantum computation with Rydberg-dressed atoms," *Phys. Rev. A*, vol. 87, p. 052314, 2013.

[48] T. Wilk, A. Gaëtan, C. Evellin, J. Wolters, Y. Miroshnychenko, P. Grangier, and A. Browaeys, "Entanglement of two individual neutral atoms using Rydberg blockade," *Phys. Rev. Lett.*, vol. 104, p. 010502, 2010.

[49] L. Isenhower, E. Urban, X. L. Zhang, A. T. Gill, T. Henage, T. A. Johnson, T. G. Walker, and M. Saffman, "Demonstration of a neutral atom controlled-not quantum gate," *Phys. Rev. Lett.*, vol. 104, p. 010503, 2010.

[50] T. Peyronel, O. Firstenberg, Q.-Y. Liang, S. Hofferberth, A. V. Gorshkov, T. Pohl, M. D. Lukin, and V. Vuletic, "Quantum nonlinear optics with single photons enabled by strongly interacting atoms," *Nature*, vol. 488, p. 57, 08 2012.

[51] J. D. Pritchard, C. S. Adams, and K. Mølmer, "Correlated photon emission from multiatom Rydberg dark states," *Phys. Rev. Lett.*, vol. 108, p. 043601, 2012.

[52] O. Mülken, A. Blumen, T. Amthor, C. Giese, M. Reetz-Lamour, and M. Weidemüller, "Survival probabilities in coherent exciton transfer with trapping," *Phys. Rev. Lett.*, vol. 99, p. 090601, 2007.

[53] V. Bendkowsky, B. Butscher, J. Nipper, J. P. Shaffer, R. Low, and T. Pfau, "Observation of ultralong-range Rydberg molecules," *Nature*, vol. 458, no. 7241, p. 1005, 2009.

[54] C. Ates, B. Olmos, J. P. Garrahan, and I. Lesanovsky, "Dynamical phases and intermittency of the dissipative quantum Ising model," *Phys. Rev. A.*, vol. 85, p. 043620, 2012.

[55] T. E. Lee, H. Häffner, and C. M. C., "Antiferromagnetic phase transition in a nonequilibrium lattice of Rydberg atoms," *Phys. Rev. A*, vol. 84, p. 031402(R), 2011.

[56] T. E. Lee, H. Häffner, and C. M. C., "Collective quantum jumps of Rydberg atoms," *Phys. Rev. Lett.*, vol. 108, p. 023602, 2012.

[57] A. Hu, T. E. Lee, and C. W. Clark, "Spatial correlations of one dimensional driven-dissipative systems of Rydberg atoms," *ArXiv e-prints*, 2013.

[58] G. Pupillo, A. Micheli, M. Boninsegni, I. Lesanovsky, and P. Zoller, "Strongly correlated gases of Rydberg-dressed atoms: Quantum and classical dynamics," *Phys. Rev. Lett.*, vol. 104, p. 223002, 2010.

[59] N. Henkel, R. Nath, and T. Pohl, "Three-dimensional roton excitations and supersolid formation in Rydberg-excited Bose-Einstein Condensates," *Phys. Rev. Lett.*, vol. 104, p. 195302, 2010.

[60] N. Bohr, "On the constitution of atoms and molecules," *Philosophical Magazine Series 6*, vol. 26, pp. 153,476, 1913.

[61] J. Han, Y. Jamil, D. V. L. Norum, P. J. Tanner, and T. F. Gallagher, "Rb nf quantum defects from millimeter-wave spectroscopy of cold ^{85}Rb Rydberg atoms," *Phys. Rev. A*, vol. 74, p. 054502, Nov 2006.

[62] I. I. Beterov, I. I. Ryabtsev, D. B. Tretyakov, and V. M. Entin, "Quasiclassical calculations of blackbody-radiation-induced depopulation rates and effective lifetimes of Rydberg ns, np, and nd alkali-metal atoms with $n \leq 80$," *Phys. Rev. A*, vol. 79, p. 052504, 2009.

[63] D. B. Branden, T. Juhasz, T. Mahlokozera, C. Vesa, R. O. Wilson, M. Zheng, A. Kortyna, and D. A. Tate, "Radiative lifetime measurements of rubidium Rydberg states," *Journal of Physics B: Atomic, Molecular and Optical Physics*, vol. 43, no. 1, p. 015002, 2010.

[64] B. Butscher, J. Nipper, J. B. Balewski, L. Kukota, V. Bendkowsky, R. Low, and T. Pfau, "Atom-molecule coherence for ultralong-range Rydberg dimers," *Nat Phys*, vol. 6, no. 12, p. 970, 2010.

[65] D. R. Lide, *CRC Handbook of Chemistry and Physics*. CRC Press, Boca Raton, 2005.

[66] V. Vuletić, "When superatoms talk photons," *Nature Physics News & Views*, vol. 2, p. 801, 2006.

[67] R. H. Dicke, "Coherence in Spontaneous Radiation Processes," *Phys. Rev.*, vol. 93, p. 99, 1954.

[68] M. Gross and S. Haroche, "Superradiance: An essay on the theory of collective spontaneous emission," *Physics Reports*, vol. 93, no. 5, p. 301, 1982.

[69] G.-D. Lin and S. F. Yelin, "Chapter 6 - superradiance: An integrated approach to cooperative effects in various systems," in *Advances in Atomic, Molecular, and Optical Physics*, vol. 61 of *Advances In Atomic, Molecular, and Optical Physics*, p. 295, Academic Press, 2012.

[70] P. Huillery, *Few and Many-body physics in a cold Rydberg gas*. PhD thesis, Ph. D. Thesis, University Paris Sud XI, 2013.

[71] J. Radogostowicz, *Investigation of dipole blockade in ultracold atomic ensembles*. PhD thesis, University of Pisa, 2010.

[72] Y. O. Dudin, L. Li, F. Bariani, and A. Kuzmich, "Observation of coherent many-body rabi oscillations," *Nat. Phys.*, vol. 8, no. 11, p. 790, 2012.

[73] M. Gärttner, K. P. Heeg, T. Gasenzer, and J. Evers, "Optimal self-assembly of Rydberg excitations for quantum gate operations," *ArXiv e-prints*, 2013.

[74] D. A. Steck, "Rubidium 87 line d data."

[75] M. Viteau, J. Radogostowicz, A. Chotia, M. G. Bason, N. Malossi, F. Fuso, D. Ciampini, O. Morsch, I. Ryabtsev, and E. Arimondo, "Ion detection in the photoionization of a rb bose–einstein condensate," *J. Phys. B: At. Mol. Opt. Phys.*, vol. 43, p. 155301, 2010.

[76] S.-H. Tsai and S. R. Salinas, "Fourth-order cumulants to characterize the phase transitions of a spin-1 Ising model," *Brazilian Journal of Physics*, vol. 28, p. 58, 1998.

[77] L. Mandel, "Sub-Poissonian photon statistics in resonance fluorescence," *Optics Letters*, vol. 4, 1979.

[78] J. A. Abate, H. J. Kimble, and L. Mandel, "Photon statistics of a dye laser," *Phys. Rev. A*, vol. 14, p. 788, 1976.

[79] N., N. L. J. Johnson, and K. Samuel, "A note on relationships between moments, central moments and cumulants from multivariate distributions," *Statistics and Probability Letters*, vol. 39, p. 49, 1998.

[80] R. Heidemann, U. Raitzsch, V. Bendkowsky, B. Butscher, R. Löw, L. Santos, and T. Pfau, "Evidence for coherent collective Rydberg excitation in the strong blockade regime," *Phys. Rev. Lett.*, vol. 99, p. 163601, 2007.

[81] Y. O. Dudin, L. Li, F. Bariani, and A. Kuzmich, "Observation of spatially ordered structures in a two-dimensional Rydberg gas," *Nature Physics*, vol. 8, p. 790, 2012.

[82] T. C. Liebisch, A. Reinhard, P. R. Berman, and G. Raithel, "Atom counting statistics in ensembles of interacting Rydberg atoms," *Phys. Rev. Lett.*, vol. 95, p. 253002, 2005.

[83] T. A. Johnson, E. Urban, T. Henage, L. Isenhower, D. D. Yavuz, T. G. Walker, and M. Saffman, "Rabi oscillations between ground and Rydberg states with dipole-dipole atomic interactions," *Phys. Rev. Lett.*, vol. 100, p. 113003, 2008.

[84] T. Vogt, M. Viteau, A. Chotia, J. Zhao, D. Comparat, and P. Pillet, "Electric-field induced dipole blockade with Rydberg atoms," *Phys. Rev. Lett.*, vol. 99, p. 073002, 2007.

[85] D. W. Schönleber, M. Gärttner, and J. Evers, "Coherent versus incoherent excitation dynamics in dissipative many-body Rydberg systems," *Phys. Rev. A*, vol. 89, p. 033421, 2014.

[86] R. Dum, P. Zoller, and H. Ritsch, "Monte carlo simulation of the atomic master equation for spontaneous emission," *Phys. Rev. A*, vol. 45, p. 4879, 1992.

[87] K. Mølmer, Y. Castin, and J. Dalibard, "Monte carlo wave-function method in quantum optics," *J. Opt. Soc. Am. B*, vol. 10, no. 3, p. 524, 1993.

[88] H. Metcalf and P. van der Straten, *Laser Cooling and Trapping*. New York: Springer, 1999.

[89] M. Gärttner, K. P. Heeg, T. Gasenzer, and J. Evers, "Finite-size effects in strongly interacting Rydberg gases," *Phys. Rev. A*, vol. 86, p. 033422, 2012.

[90] F. Robicheaux and J. V. Hernández, "Many-body wave function in a dipole blockade configuration," *Phys. Rev. A*, vol. 72, p. 063403, 2005.

[91] K. C. Younge, A. Reinhard, T. Pohl, P. R. Berman, and G. Raithel, "Mesoscopic Rydberg ensembles: Beyond the pairwise-interaction approximation," *Phys. Rev. A*, vol. 79, p. 043420, 2009.

[92] C. Ates, T. Pohl, T. Pattard, and J. M. Rost, "Many-body theory of excitation dynamics in an ultracold Rydberg gas," *Physical Review A (Atomic, Molecular, and Optical Physics)*, vol. 76, no. 1, p. 013413, 2007.

[93] K. P. Heeg, M. Gärttner, and J. Evers, "Hybrid model for Rydberg gases including exact two-body correlations," *Phys. Rev. A*, vol. 86, p. 063421, 2012.

[94] B. Sun and F. Robicheaux, "Spectral linewidth broadening from pair fluctuations in a frozen Rydberg gas," *Phys. Rev. A*, vol. 78, p. 040701(R), 2008.

[95] J. Stanojevic, V. Parigi, E. Bimbard, A. Ourjoumtsev, P. Pillet, and G. P., "Generating non-gaussian states using collisions between Rydberg polaritons," *Phys. Rev. A*, vol. 86, p. 021403, 2012.

[96] R. Egger, H. Grabert, and U. Weiss, "Crossover from coherent to incoherent dynamics in damped quantum systems," *Phys. Rev. E*, vol. 55, p. R3809, 1997.

[97] J. V. Hernández and F. Robicheaux, "Coherence conditions for groups of Rydberg atoms," *Journal of Physics B: Atomic, Molecular and Optical Physics*, vol. 39, no. 23, p. 4883, 2006.

[98] W. Ketterle and M. W. Zwierlein, "Making, probing and understanding ultracold fermi gases," in *Ultracold Fermi Gases* (S. S. M. Inguscio and C. Wieman, eds.), Proceedings of the International School of Physics "Enrico Fermi", Course CLXIV, p. 95, IOS Press, Amsterdam, 2008.

[99] K. Afrousheh, P. Bohlouli-Zanjani, D. Vagale, A. Mugford, M. Fedorov, and J. D. D. Martin, "Spectroscopic observation of resonant electric dipole-dipole interactions between cold Rydberg atoms," *Phys. Rev. Lett.*, vol. 93, p. 233001, 2004.

[100] C. S. E. van Ditzhuijzen, A. F. Koenderink, J. V. Hernández, F. Robicheaux, L. D. Noordam, and H. B. v. L. van den Heuvell, "Spatially resolved observation of dipole-dipole interaction between Rydberg atoms," *Phys. Rev. Lett.*, vol. 100, p. 243201, 2008.

[101] A. Reinhard, K. C. Younge, and G. Raithel, "Effect of förster resonances on the excitation statistics of many-body Rydberg systems," *Phys. Rev. A*, vol. 78, p. 060702, 2008.

[102] M. Viteau, M. Bason, J. Radogostowicz, N. Malossi, O. Morsch, D. Ciampini, and E. Arimondo, "Rydberg excitation of a Bose-Einstein Condensate," *Laser Phys.*, vol. 23, p. 015502, 2013.

[103] G. Lochead, D. Boddy, D. P. Sadler, C. S. Adams, and M. P. A. Jones, "Number-resolved imaging of excited-state atoms using a scanning autoionization microscope," *Phys. Rev. A*, vol. 87, p. 053409, 2013.

[104] M. Ebert, A. Gill, M. Gibbons, X. Zhang, M. Saffman, and T. G. Walker, "Atomic fock state preparation using Rydberg blockade," *Phys. Rev. Lett.*, vol. 112, p. 043602, 2014.

[105] M. Ebert, M. Kwon, T. Walker, and M. Saffman, "Coherence and Rydberg blockade of atomic ensemble qubits," *ArXiv e-prints*, 2015.

[106] D. Petrosyan, M. Höning, and M. Fleischhauer, "Spatial correlations of Rydberg excitations in optically driven atomic ensembles," *Phys. Rev. A*, vol. 87, p. 053414, 2013.

[107] D. Petrosyan, "Dynamics and equilibration of Rydberg excitations in dissipative atomic ensembles," *Journal of Physics B: Atomic, Molecular and Optical Physics*, vol. 46, no. 14, p. 141001, 2013.

[108] T. Amthor, C. Giese, C. S. Hofmann, and M. Weidemüller, "Evidence of antiblockade in an ultracold Rydberg gas," *Phys. Rev. Lett.*, vol. 104, p. 013001, 2010.

[109] C. Ates, T. Pohl, T. Pattard, and J. M. Rost, "Antiblockade in Rydberg excitation of an ultracold lattice gas," *Phys. Rev. Lett.*, vol. 98, no. 2, p. 023002, 2007.

[110] H. Schempp, G. Günter, M. Robert-de Saint-Vincent, C. S. Hofmann, D. Breyel, A. Komnik, D. W. Schönleber, M. Gärttner, J. Evers, S. Whitlock, and M. Weidemüller, "Full Counting Statistics of laser excited Rydberg aggregates in a one-dimensional geometry," *Phys. Rev. Lett.*, vol. 112, p. 013002, 2014.

[111] I. Lesanovsky and J. P. Garrahan, "Out-of-equilibrium structures in strongly interacting Rydberg gases with dissipation," *Phys. Rev. A*, vol. 90, p. 011603, 2014.

[112] G. H. Fredrickson and H. C. Andersen, "Kinetic Ising model of the glass transition," *Phys. Rev. Lett.*, vol. 53, pp. 1244–1247, Sep 1984.

[113] J. P. Garrahan and D. Chandler, "Geometrical explanation and scaling of dynamical heterogeneities in glass forming systems," *Phys. Rev. Lett.*, vol. 89, p. 035704, Jul 2002.

[114] F. Ritort and P. Sollich, "Glassy dynamics of kinetically constrained models," *Advances in Physics*, vol. 52, no. 4, p. 219, 2003.

[115] C. Carr, R. R., K. J. Weatherill, , and C. S. Adams, "Non-equilibrium phase transition in a dilute Rydberg ensemble," *ArXiv e-prints*, 2013.

[116] S. Sachdev, *Quantum Phase Transitions*. Cambridge University Press, 20011.

[117] T. D. Schultz, D. C. Mattis, and E. H. Lieb, "Two-dimensional Ising model as a soluble problem of many fermions," *Rev. Mod. Phys.*, vol. 36, p. 856, 1964.

[118] J. B. Kogut, "An introduction to lattice gauge theory and spin systems," *Rev. Mod. Phys.*, vol. 51, p. 659, 1979.

[119] C. Svoboda, D. Nozadze, F. Hrahsheh, and T. Vojta, "Disorder correlations at smeared phase transitions," *EPL (Europhysics Letters)*, vol. 97, no. 2, p. 20007, 2012.

[120] L. Demkó, S. Bordács, T. Vojta, D. Nozadze, F. Hrahsheh, C. Svoboda, B. Dóra, H. Yamada, M. Kawasaki, Y. Tokura, and I. Kézsmárki, "Disorder promotes ferromagnetism: Rounding of the quantum phase transition in $\mathrm{sr}_{1-x}\mathrm{ca}_x\mathrm{ruo}_3$," *Phys. Rev. Lett.*, vol. 108, p. 185701, May 2012.

[121] A. J. Leggett, "Testing the limits of quantum mechanics: motivation, state of play, prospects," *Journal of Physics: Condensed Matter*, vol. 14, no. 15, p. R415, 2002.

[122] T. E. Lee and C.-K. Chan, "Dissipative transverse-field Ising model: Steady-state correlations and spin squeezing," *Phys. Rev. A*, vol. 88, p. 063811, Dec 2013.

[123] H.-P. Breuer and F. Petruccione, *Theory of open quantum systems*. Oxford University Press, 2002.

[124] J. P. Garrahan and I. Lesanovsky, "Thermodynamics of quantum jump trajectories," *Phys. Rev. Lett.*, vol. 104, p. 160601, 2010.

[125] J. P. Garrahan, R. L. Jack, V. Lecomte, E. Pitard, K. van Duijvendijk, and F. van Wijland, "Dynamical first-order phase transition in kinetically constrained models of glasses," *Phys. Rev. Lett.*, vol. 98, p. 195702, 2007.

[126] V. Lecomte, C. Appert-Rolland, and F. van Wijland, "Thermodynamic formalism for systems with markov dynamics," *Journal of Statistical Physics*, vol. 127, no. 1, p. 51, 2007.

[127] C. Maes and K. Netockny, "Canonical structure of dynamical fluctuations in mesoscopic nonequilibrium steady states," *EPL (Europhysics Letters)*, vol. 82, no. 3, p. 30003, 2008.

[128] M. Marcuzzi, E. Levi, S. Diehl, J. P. Garrahan, and I. Lesanovsky, "Universal nonequilibrium properties of dissipative Rydberg gases," *Phys. Rev. Lett.*, vol. 113, p. 210401, 2014.

[129] M. Gärttner, S. Whitlock, D. Schönleber, and J. Evers, "Collective excitation of Rydberg-atom ensembles beyond the $\sqrt{N}$ enhancement," *eprint arXiv:1408.2453*, 2014.

[130] H. Weimer, "Variational principle for steady states of dissipative quantum many-body systems," *Phys. Rev. Lett.*, vol. 114, p. 040402, Jan 2015.

[131] H. Weimer, "Variational analysis of driven-dissipative Rydberg gases," *ArXiv e-prints*, Jan. 2015.

[132] R. M. W. van Bijnen, S. Smit, K. A. H. van Leeuwen, and E. J. D. K. S. J. J. M. F. Vredenbregt, "Adiabatic formation of Rydberg crystals with chirped laser pulses," *J. Phys. B: At. Mol. Opt. Phys.*, vol. 12, p. 1030442, 2011.

[133] A. Auerbach, *Interacting electrons and quantum magnetism*. Springer-Verlag, New York, 1994.

[134] E. Collini, "Spectroscopic signatures of quantum-coherent energy transfer," *Chem. Soc. Rev.*, vol. 42, p. 4932, 2013.

[135] H. Lee, Y.-C. Cheng, and G. R. Fleming, "Coherence dynamics in photosynthesis: Protein protection of excitonic coherence," *Science*, vol. 316, no. 5830, pp. 1462–1465, 2007.

[136] I. Bloch, J. Dalibard, and W. Zwerger, "Many-body physics with ultracold gases," *Rev. Mod. Phys.*, vol. 80, p. 885, 2008.

[137] I. Bloch, J. Dalibard, and S. Nascimbene, "Quantum simulations with ultracold quantum gases," *Nat Phys*, vol. 8, p. 267, Apr. 2012.

[138] S. Diehl, A. Tomadin, A. Micheli, R. Fazio, and Z. P., "Dynamical phase transitions and instabilities in open atomic many-body systems," *Phys. Rev. Lett.*, vol. 105, p. 015702, 2010.

[139] D. Barredo, S. Ravets, H. Labuhn, L. Béguin, A. Vernier, F. Nogrette, T. Lahaye, and A. Browaeys, "Demonstration of a strong Rydberg blockade in three-atom systems with anisotropic interactions," *Phys. Rev. Lett.*, vol. 112, p. 183002, 2014.

[140] P. Schauß, J. Zeiher, T. Fukuhara, S. Hild, M. Cheneau, T. Macrì, T. Pohl, I. Bloch, and C. Gross, "Dynamical crystallization in a low-dimensional Rydberg gas," *ArXiv e-prints*, Apr. 2014.

[141] G. Günter, H. Schempp, M. Robert-de Saint-Vincent, V. Gavryusev, S. Helmrich, C. S. Hofmann, S. Whitlock, and M. Weidemüller, "Observing the dynamics of dipole-mediated energy transport by interaction-enhanced imaging," *Science*, vol. 342, no. 6161, p. 954, 2013.

[142] B. Olmos, W. Li, S. Hofferberth, and I. Lesanovsky, "Amplifying single impurities immersed in a gas of ultracold atoms," *Phys. Rev. A*, vol. 84, p. 041607, 2011.

[143] M. Fleischhauer, A. Imamoglu, and J. P. Marangos, "Electromagnetically induced transparency: Optics in coherent media," *Reviews of Modern Physics*, vol. 77, no. 2, p. 633, 2005.

[144] I. Mourachko, D. Comparat, F. de Tomasi, A. Fioretti, P. Nosbaum, V. M. Akulin, and P. Pillet, "Many-body effects in a frozen Rydberg gas," *Phys. Rev. Lett.*, vol. 80, p. 253, 1998.

[145] W. R. Anderson, J. R. Veale, and T. F. Gallagher, "Resonant dipole-dipole energy transfer in a nearly frozen Rydberg gas," *Phys. Rev. Lett.*, vol. 80, p. 249, 1998.

[146] G. S. Engel, T. R. Calhoun, E. L. Read, T.-K. Ahn, T. Mancal, Y.-C. Cheng, R. E. Blankenship, and G. R. Fleming, "Evidence for wavelike energy transfer through quantum coherence in photosynthetic systems," *Nature*, vol. 446, p. 782, 04 2007.

[147] M. Sarovar, A. Ishizaki, G. R. Fleming, and K. B. Whaley, "Quantum entanglement in photosynthetic light-harvesting complexes," *Nat Phys*, vol. 6, p. 462, 06 2010.

[148] M. B. Plenio and S. F. Huelga, "Dephasing-assisted transport: quantum networks and biomolecules," *New Journal of Physics*, vol. 10, no. 11, p. 113019, 2008.

[149] P. Rebentrost, M. Mohseni, I. Kassal, S. Lloyd, and A. Aspuru-Guzik, "Environment-assisted quantum transport," *New Journal of Physics*, vol. 11, no. 3, p. 033003, 2009.

[150] H. Schempp, *Formation of Aggregates and Energy Transport in Ultracold Rydberg Interacting Gases*. PhD thesis, Heidelberg University, 2014.

[151] D. Maxwell, D. J. Szwer, D. Paredes-Barato, H. Busche, J. D. Pritchard, A. Gauguet, K. J. Weatherill, M. P. A. Jones, and C. S. Adams, "Storage and control of optical photons using Rydberg polaritons," *Phys. Rev. Lett.*, vol. 110, p. 103001, Mar 2013.

[152] J. Honer, R. Löw, H. Weimer, T. Pfau, and H. P. Büchler, "Artificial atoms can do more than atoms: Deterministic single photon subtraction from arbitrary light fields," *Phys. Rev. Lett.*, vol. 107, p. 093601, 2011.

[153] M. Reetz-Lamour, J. Deiglmayr, T. Amthor, and M. Weidemüller, "Rabi oscillations between ground and Rydberg states and van der waals blockade in a mesoscopic frozen Rydberg gas," *New Journal of Physics*, vol. 10, no. 4, p. 045026, 2008.

Acknowledgements

Saving the best for the last, I would like now to thank all those people who have contribute to the development and success of this work. When I arrived to Pisa three years ago, I could not even imagine all the nice things that would happen to me and how the PhD would change not only my career, but also my life.

In primo luogo, vorrei ringraziare la mia supervisor **Dr. Donatella Ciampini** per avermi incoraggiato sempre a lavorare su questo sperimento, per tutte le cose che da lei ho imparato, per le discussioni e il suo aiuto tutte le volte che gliel'ho chiesto.

Grazie al **Dr. Oliver Morsch** per aver messo tanto impegno per insegnarmi, per la sua pazienza e per incoraggiarmi sempre a dare il meglio di me stessa. Per tutta la libertà che mi ha dato per lavorare sullo sperimento, le lunghe discussioni, i suoi saggi consigli e per la disponibilità che ha sempre dimostrato. Grazie per aver creduto in me e darmi la posibilità di venire a lavorare a Pisa.

Grazie al **Prof. Ennio Arimondo** per avermi dato l'opportunità di venire a Pisa a far parte del suo gruppo e di aver potuto lavorare su un tema che mi appassiona a fianco a ricercatori di primo livello da cui ho imparato tanto.

Grazie al **Prof. Francesco Fuso** per le sue parole sempre sagge e la sua forma di fare per cui ci riesce sempre a risolvere anche le situazioni più difficili.

Vorrei anche ringraziare a tutti quanti con cui ho lavorato direttamente sullo sperimento durante questi tre anni: il **Dr. Nicola Malossi** che ha avuto la pazienza d'insegnami tutto da capo; **Stefano Scotto** e **Luigi Gianelli**, insieme a chi ho dato i miei primi passi in questo laboratorio; ai dottorandi **Cristiano Simonelli** e **Riccardo Faoro**, con chi ho avuto il piacere di lavorare durante quest'ultimo anno; e ai laureandi **Matteo Archimi**, **Guido Masella**, **Francesco Fogliano**,

Luca Asteria, con chi ho colaborato in questo ultimo periodo. Grazie a tutti per i momenti che abbiamo visuto insieme, per aver reso il lavoro un divertimento e non un obbligo, per le lunghe discussioni che abbiamo fatto e per tutto quanto ho imparato di ciascuno di loro. In bocca al lupo con le tesi, sono convinta gli porterete in fine con successo.

Se c'è una persona in Italia per chi non mi basterebbero tutte queste pagine per ringraziarla, quella è **Francesca Usala** perché, senza di lei io non sarei sopravvissuta nemmeno un giorno. Grazie per l'aiuto in tutti sensi, per ascoltarmi e per farmi ridere (anche se penso che quello l'ho fatto io di piú con te). Desidero soltanto si rimetta al piú presto e ritorna ad essere come sempre.

Grazie anche a **Nicola Puccini** ed **Enrico Andreoni** perché indipendentemente di cosa non andase bene o si fosse rotta, loro sono stati sempre disponibili ad aiutare e subito mi hanno aiutato a sistemare tutto in forma che potesse continuare col mio lavoro.

I would like to thank to **Prof. Matthias Weidemüller** who made a big effort to make possible the coutelle agreement between Universities of Pisa and Heidelberg, and gave me the great opportunity to join his group and who encouraged me in working on very interesting topics.

Vorrei specialmente ringraziare al **Prof. Francesco Pegoraro** per l'impegno che ha messo per fare possibile l'accordo di cotutela fra le Università di Pisa e Heidelberg, che mi ha dato la possibiltà, non solo di avere questo doppio titolo, se no anche di completare la mia formazione come scienziata ed spero mi aprirà tante porte in un futuro.

I would like also to thank to the other members of the committee, **Prof. Giovanni Modugno** and **Prof. Thomas Gasenzer**, for commenting and proofreading this work.

Thanks to **Prof. Maarten Hoogerland** and **Prof. Mikkel Andersen** for joining us and contributing to the experiment.

Many thanks to **Vladislav Gavryusev**, **Miguel Ferreira Cao** and **Giulia Faraoni**. We made a good team in Heidelberg and working with you was a very good experience. Thanks for the nice time together in the lab as well as for the fruitful discussions. I am convince you will manage to show everybody the great scientists you are, I wish you the best with your PhD's and I'm sure in a few years we will laugh remembering all the conversations we had during the past months. Last thing to Miguel and Vlad: I still believe the other "Rydberg project" will be a bestseller one day.

I would like also to thank to the other present and past members of the Heidelberg team: **Shannon Whitlock, Georg Gunter, Hanna Schempp, Valentin Ivannikov, Luc Coutourier** and **Yu Lu**, for the fruitful discussions, great cooperation and pleasant atmosphere during the time I spent in Heidelberg.

Entrando en un terreno puramente personal, quiero dar las gracias a mi amiga **Isabel Martínez-Espejo Zaragoza**, a quien conocí por casualidad el primer día que llegué a Pisa y, desde entonces, ha sido un gran apoyo en todos los pasos que he dado en esta aventura.

Gracias **a mi familia:** mis padres, **María Teresa** y **Juan Antonio** y mi hermano **Álvaro**. Gracias por haberme apoyado siempre, no sólo en mi decisión de venir a Pisa y en todo lo que he hecho durante estos tres años, sino también a lo largo de toda mi vida. Porque soy consciente del gran esfuerzo que han hecho durante todos estos años para ayudarme a conseguir mi sueño y también por entenderme. Sin su compresión su cariño esta tesis no habría sido posible y, por este motivo, està dedicada a ellos.

Finalmente, voglio ringraziare **Giovanni Nizzola**, *mi sol*, per appoggiarmi in tutto ció che faccio, per le sue opinioni critiche, per il suo sostegno e, sopratutto, per credere in me quando nemmeno io stessa lo facevo. Se ho finito questa tesi con successo è in grande parte grazie a lui e a che è stato sempre a fianco a me. Sono sicura che, così come abbiamo vinto questa volta, vinceremo anche il resto.